University of Alberta

Design of an Annular Mixing Jet Pump

by

David Lennard deJong

A thesis submitted to the Faculty of Graduate Studies and Research in partial fulfillment of the requirements for the degree of Master of Science.

Department of Mechanical Engineering

Edmonton, Alberta
Spring 2002

National Library of Canada
Acquisitions and Bibliographic Services
395 Wellington Street
Ottawa ON K1A 0N4
Canada

Bibliothèque nationale du Canada
Acquisitions et services bibliographiques
395, rue Wellington
Ottawa ON K1A 0N4
Canada

Your file Votre référence

Our file Notre référence

The author has granted a non-exclusive licence allowing the National Library of Canada to reproduce, loan, distribute or sell copies of this thesis in microform, paper or electronic formats.

The author retains ownership of the copyright in this thesis. Neither the thesis nor substantial extracts from it may be printed or otherwise reproduced without the author's permission.

L'auteur a accordé une licence non exclusive permettant à la Bibliothèque nationale du Canada de reproduire, prêter, distribuer ou vendre des copies de cette thèse sous la forme de microfiche/film, de reproduction sur papier ou sur format électronique.

L'auteur conserve la propriété du droit d'auteur qui protège cette thèse. Ni la thèse ni des extraits substantiels de celle-ci ne doivent être imprimés ou autrement reproduits sans son autorisation.

0-612-69797-5

Canada

University of Alberta

Library Release Form

Name of Author: David Lennard deJong

Title of Thesis: Design of an Annular Mixing Jet Pump

Degree: Master of Science

Year this Degree Granted: 2002

Permission is hereby granted to the University of Alberta to reproduce single copies of this thesis and to lend or sell such copies for private, scholarly, or scientific research purposes only.

The author reserves all other publication and other rights in association with the copyright in the thesis, and except as hereinbefore provided, neither the thesis nor any substantial portion thereof may be printed or otherwise reproduced in any material form whatever without the author's prior written permission.

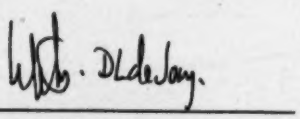

David Lennard deJong
8308 152A avenue NW
Edmonton, Alberta,
Canada T5E 3B2

31 January 2002

University of Alberta

Faculty of Graduate Studies and Research

The undersigned certify that they have read, and recommend to the Faculty of Graduate Studies and Research for acceptance, a thesis entitled *Design of an Annular Mixing Jet Pump* submitted by David Lennard deJong in partial fulfillment of the requirements for the degree of Master of Science.

Dr. L. W. Sigurdson (Advisor)

Dr. J. Szymanski

Dr. R. W. Toogood

28 January 2002

The Country of the Young

A.Y. Jackson for instance
83 years old
halfway up a mountain
standing in a patch of snow
to paint a picture that says
"Look here
You've never seen this country
it's not the way you thought it was
Look again"
And boozy traders
lost in a dream of money
crews of homesick seamen
moored to a China-vision
hunting the North West Passage
they didn't see it either
The colours I mean
for they're not bright Gauguin
or blazing Vincent
not even Breughel's "Hunters in the Snow"
where you can get lost
and found in five minutes
–but the original colour-matrix
that after a giant's heartbeat
lighted the maple forests
in the country south
You have to stoop a little
bend over and then look up
–dull orange on a cliff face
that says iron deposits
olive leaves of the ground willow
with grey silver catkins
minute wild flower beacons
sea blue as the world's eye-
And you can't be looking for something else
money or a night's lodging on earth
a stepping stone to death maybe
or you'll never find the place
hear an old man's voice
in the country of the young
that says
"Look here—"

–Al Purdy

for Marcella, who may never understand why I did this,
and for Victoria, who some day just might

Abstract

A type of jet pump called the annular mixing jet pump was investigated. It uses multiple jets flowing into an annulus formed between two concentric pipes, with the jets parallel to the pipes. The secondary flow travels radially inward toward the pipes, then turns through 90° to align with the annulus and mix with the jets. Experiments were conducted in water with a model sectioned longitudinally in half. The effects of four parameters were studied: the nozzle to throat separation, the jet inlet pressure, the nozzle to throat area ratio, and the number of jets. The annular mixing jet pump exhibits performance similar to a centre jet pump, except that it is strongly affected by the number of jets. The model had a very low area ratio, making it very resistant to cavitation. The use of a one-dimensional computer simulation to design this type of jet pump is discussed along with favourable comparisons with the experiments.

ACKNOWLEDGEMENTS

It takes a village to raise a child, and this progeny was no different.

I must first thank Ray Field, for his vision of where he wants to take his company, and his firm belief in the value of research to enable that future.

Next, I thank Dr. Lorenz Sigurdson who, as my advisor, provided considerable insight into the nature of research. Without his help, this exercise would have taken even longer than it did.

There were many others who helped in ways large and small. I wish to thank all the faculty and staff of the Mechanical Engineering Department, notably Ian Buttar, Don Fuhr, Dave Pape, Albert Yuen, Bernie Faulkner, Terry Nord, and Mark Ackerman for their help making things, and more importantly, making things work; Mssrs. Brian Smeenk, Eric Peace, and Luigi Esposito of Big Iron Drilling Ltd. for their help fabricating the equipment and conducting experiments; Mr. Russ Baldwin of Baldwin Machining and Installation Ltd., who made all those little jets; and the Vortex Fluid Dynamics Group: Chris Apps, Andrew Coward, and John Diep, for their help with equipment, instrumentation, imagery, and LaTeX.

This work was funded by Big Iron Drilling Ltd. of Edmonton, with support from the National Research Council of Canada Industrial Research Assistance Program, Project Number 344353.

CONTENTS

1 Introduction to the Jet Pump 1
- 1.1 Introduction . . . 1
- 1.2 History and Terminology of Jet Pump Design . . . 2
  - 1.2.1 Conventional Jet Pump Designs . . . 2
  - 1.2.2 Operation of Jet Pumps . . . 5
  - 1.2.3 Alternative Jet Pump Designs . . . 10
  - 1.2.4 Applications of Jet Pumps . . . 12
- 1.3 Methodology and Objectives . . . 18
- 1.4 Thesis Outline . . . 21

2 Experimental Setup and Apparatus 23
- 2.1 Introduction . . . 23
- 2.2 Apparatus . . . 23
  - 2.2.1 Test Tank . . . 23
  - 2.2.2 Plumbing . . . 25
- 2.3 Jet Pump Model . . . 27
- 2.4 Performance Measurements . . . 32
  - 2.4.1 Flow Instrumentation . . . 32
  - 2.4.2 Pressure Instrumentation . . . 33
  - 2.4.3 Miscellaneous Instrumentation . . . 34
  - 2.4.4 Instrument Calibration . . . 35
- 2.5 Flow Visualization . . . 35
  - 2.5.1 Dye Injection System . . . 36
  - 2.5.2 Image Capture System . . . 37
- 2.6 Experimental Procedures . . . 38
  - 2.6.1 Performance Measurements . . . 38
  - 2.6.2 Flow Visualization . . . 39

3 Simulation of the Experiments 41
3.1 Introduction 41
3.2 Approach 41
3.3 Schematic Diagram 42
3.4 Flow Diagram 42
3.5 One-Dimensional Energy Equation 45
3.6 Continuity Equation 46
3.7 Energy Loss Terms 47
3.7.1 Pipe Wall Friction 48
3.7.2 Flow Direction Changes (Elbows) 50
3.7.3 Gradual Area Changes 52
3.7.4 Sudden Area Changes 53
3.7.5 Jet Mixing Losses 55
3.7.6 Non-Circular Shapes and Effective Diameter 57
3.7.7 Combined Effects 60
3.8 Construction and Solution of the Model 60
3.9 Validation of the Model 62
3.9.1 Unit Testing 62
3.9.2 Integration Testing 63
3.9.3 Final Validation Comments 64

4 Measurement and Simulation Accuracy 66
4.1 Introduction 66
4.2 Combination and Propagation of Errors 66
4.3 Accuracy of the Experimental Measurements 69
4.3.1 Uncertainty of the Measured Flow Rates 70
4.3.2 Uncertainty of the Measured Jet Inlet Pressure 75
4.3.3 Uncertainty of the Measured Mixing Region Pressures . 76
4.3.4 Uncertainty of Other Measurements 79
4.3.5 Uncertainty of the Reduced Data 79
4.4 Accuracy of the Simulation 81
4.4.1 Uncertainty of the Simulated Flow Rates 82
4.4.2 Uncertainty of the Simulated Static Pressures 86
4.4.3 Uncertainty of the Simulated Efficiency 87
4.5 Comments on the Simulation Uncertainty 89

5 Results and Discussion **91**
5.1 Introduction 91
5.2 Effect of Nozzle to Throat Separation 93
5.2.1 Effect on Flow Rates 94
5.2.2 Effect on Mixing 94
5.2.3 Effect on Efficiency 97
5.3 Effect of Jet Inlet Pressure 99
5.3.1 Effect on Flow Rates 99
5.3.2 Effect on Mixing 103
5.3.3 Effect on Efficiency 105
5.4 Effect of Area Ratio 107
5.4.1 Effect on Flow Rates 108
5.4.2 Effect on Mixing 109
5.4.3 Effect on Efficiency 110
5.5 Effect of Number of Jets 112
5.5.1 Effect on Flow Rates 113
5.5.2 Effect on Mixing 115
5.5.3 Effect on Efficiency 123
5.6 Cavitation 125
5.7 Simulation Error 131
5.8 Considerations for Design 131
5.8.1 General Discussion 133
5.8.2 Use of the Simulation 136

6 Summary and Conclusions **138**
6.1 Introduction 138
6.2 Conclusions from the Experiments 140
6.3 Conclusions from the Simulation 143
6.4 Recommendations for Future Work 144

Bibliography **146**

A Simulation Uncertainty Parameters **151**

B Experiment and Simulation Data **155**

List of Tables

3.1 Loss Coefficients for 90° Elbows 51
3.2 Loss Coefficients for Sudden Area Changes 55
3.3 Rounded Inlet Correction Factors to K_{sc} 56

4.1 Relative Uncertainty of Flows Measurable by Calibration . . . 73
4.2 Flow Rate Measurement Uncertainty Summary 75
4.3 Relative Uncertainties of Static Pressure Instruments 77
4.4 Uncertainty of Simulated Flow Rates 83
4.5 Uncertainty of Simulation Results for P_4 86
4.6 Uncertainty of Simulation Results for η 88

5.1 General Design Recommendations 136

6.1 General Design Recommendations 143

A.1 Parameters Contributing to Simulation Uncertainty 151

B.1 Experimental Test Schedule 156
B.2 Nozzle to Throat Distances 156

List of Figures

1.1 Centre Jet Pump 4
1.2 Annular Jet Pump 5
1.3 Bidimensional Jet Pump 11
1.4 Annular Mixing Jet Pump 12
1.5 Discrete Peripheral Jet Pump 13
1.6 Jet Pump in a Water Conditioner 17
1.7 Johnson Backwash Device 19
1.8 Field Backwash Device 20

2.1 Experimental Apparatus 24
2.2 Experimental Apparatus Plumbing 26
2.3 Experimental Model Mounted on Window 28
2.4 Detailed View of Inlet and Mixing Regions 30

3.1 Schematic Diagram of Apparatus 43
3.2 Flow Diagram for the Simulation 44

5.1 Effect of Nozzle to Throat Separation on Flow Rates 95
5.2 Effect of Nozzle to Throat Separation on Mixing 96
5.3 Effect of Nozzle to Throat Separation on Efficiency 98
5.4 Effect of Jet Inlet Pressure on Flow Rates 100
5.5 Effect of Jet Inlet Pressure on Mixing 104
5.6 Effect of Jet Inlet Pressure on Efficiency 106
5.7 Effect of Area Ratio on Flow Rates 109
5.8 Effect of Area Ratio on Mixing 110
5.9 Effect of Area Ratio on Efficiency 111
5.10 Effect of Number of Jets on Flow Rates 114
5.11 Effect of Number of Jets on Mixing Pressures 117
5.12 Recirculation in Jet Pumps 119
5.13 Mixing Region Recirculation Image 121

5.14 Effect of Number of Jets on Efficiency 124
5.15 Incipient Cavitation Image 127
5.16 Simulation Error 132

B.1 Flow Rate Q_1 Results 157
B.2 Flow Rate Q_2 Results 158
B.3 Flow Rate Q_3 Results 159
B.4 Static Pressure P_4 Results 160
B.5 Flow Ratio M Results 161
B.6 Jet Pump Efficiency η Results 162
B.7 Mixing Pressure Results - Tests 1 to 5 163
B.8 Mixing Pressure Results - Tests 6 to 10 164
B.9 Mixing Pressure Results - Tests 11 to 15 165
B.10 Mixing Pressure Results - Tests 16 to 20 166
B.11 Mixing Pressure Results - Tests 21 to 25 167
B.12 Mixing Pressure Results - Tests 26 to 30 168
B.13 Mixing Pressure Results - Tests 31 to 35 169
B.14 Mixing Pressure Results - Tests 36 to 40 170
B.15 Mixing Pressure Results - Tests 41 to 45 171

NOMENCLATURE

α ..... kinetic energy correction factor

ϵ ..... surface roughness height, cm

ϕ^* ..... shape factor for non-circular ducts

μ ..... dynamic viscosity, g/(cm · s)

ν ..... kinematic viscosity, cm^2/s

ρ ..... mass density, g/cm^3

η ..... jet pump efficiency MN

σ ..... cavitation number

A ..... area, cm^2

d ..... distance (linear), cm or m

D ..... diameter, mm or cm

f ..... friction factor

g ..... gravity, 980.9 cm/s^2

H ..... head $(\frac{P}{\rho g} + \frac{U^2}{2g} + z)$, cm

k ..... laminar friction coefficient $f_l Re$

K ..... loss coefficient

L ..... length, cm

M ..... flow ratio $\frac{Q_2}{Q_1}$

N ..... head ratio $\frac{(H_3-H_7)}{(H_0-H_3)}$

P ..... static pressure, kPa

$\mathcal{P}$ ..... wetted perimeter, cm

Q ..... volumetric flow rate, cm^3/s

r ..... radius, cm

R ..... nozzle to throat area ratio $\frac{A_n}{A_t}$

Re ..... Reynolds number $\frac{UD}{\nu}$

s ..... nozzle to throat distance, cm

U ..... velocity, cm/s

V ..... volume, cm^3

z ..... elevation, cm

subscripts:

eff ..... effective

el ..... elbow

f ..... friction

gc ..... gradual contraction

ge ..... gradual expansion

hyd ..... hydraulic

i, in ..... inlet

j ..... jet

l ..... laminar

mix ..... mixing

n ..... nozzle

o, out ..... outlet

p ..... primary

s ..... secondary

sc ..... sudden contraction

se ..... sudden expansion

t ..... tertiary, turbulent, throat

T ..... pressure tap

v ..... vapour

Chapter 1

Introduction to the Jet Pump

1.1 Introduction

The jet pump, also known as the eductor, is commonly used throughout the world. These devices have very simple construction, contain no moving parts, and can be manufactured from a wide variety of materials. Their applications are numerous, ranging from simple domestic water pumping to use in advanced aerospace vehicles and nuclear reactors.

This thesis describes research performed with a type of jet pump called the annular mixing jet pump. The work included experiments with a model of the annular mixing jet pump, and the development of a one-dimensional computer simulation which could be used to design this type of jet pump.

In this chapter, the jet pump is introduced. A brief discussion of its history and theory of operation is given, followed by an overview of several different jet pump designs and applications.

1.2 History and Terminology of Jet Pump Design

The history of jet pumps has been developing for over 150 years, when the earliest known work describing the jet pump was published (Thomson, 1852). The theoretical foundation for jet pump analysis followed later (Rankine, 1870), with primarily experimental work by numerous researchers in the late 19th and early 20th centuries. In the 1930s, a landmark report was published by Gosline and O'Brein (1934), which was the first paper to combine experimental results with a theoretical analysis of jet pumps. Since then, there has been much activity in furthering the understanding of jet pump capabilities and limitations. Reviews of jet pump literature by Bonnington and Hemmings (1976) and Blevins (1992) cite over four hundred papers, and at the end of 2001, the Ei Compendex engineering literature database, published by Elsevier Engineering Information Inc., listed over two hundred papers published since 1984. Despite the jet pump's apparent simplicity and long history, many researchers continue to investigate this versatile device.

1.2.1 Conventional Jet Pump Designs

A jet pump operates through momentum transfer from jet with low volumetric flow rate and high flow velocity to another fluid. These flows combine into a total flow with a volumetric flow rate greater than the jet alone, but with a velocity which is much lower than the jet. Because of the losses associated with mixing, jet pumps have a low energy efficiency compared with other

pumping methods. However, where efficiency is not a primary concern, the simplicity and reliability of the jet pump may make it the best method of pumping.

There are two common types of jet pumps; these are generally known as centre jet pumps and annular jet pumps. These two types have very similar principles of operation, and differ mainly in the configuration of the jet.

A centre jet pump is shown in Figure 1.1. The device has generally axisymmetrical construction of circular cross-section, with a single jet located on the axis in the inlet region of the pump. The inlet region is typically convergent until the throat is reached, defined as the point where the cross-sectional area first reaches a minimum. This is followed by the mixing region, which has a constant cross-sectional area. Depending on the application, this may be followed by a divergent diffuser region. The diffuser may serve two useful purposes: firstly, to raise the static pressure of the mixed fluids, and secondly, to reduce the flow velocity and associated pipe wall friction losses. However, with increased pipe size comes increased material, handling, and installation costs, and the pump system designer must balance the merits and drawbacks of reducing the flow velocity.

An annular jet pump is shown in Figure 1.2. Its features are similar to the centre jet pump, except for the jet, which flows from an annulus located on the periphery of the inlet region. The driving fluid is pumped through this annulus, and creates an annular jet along the wall of the mixing region. Because of the geometry of the annular jet, this type of jet pump

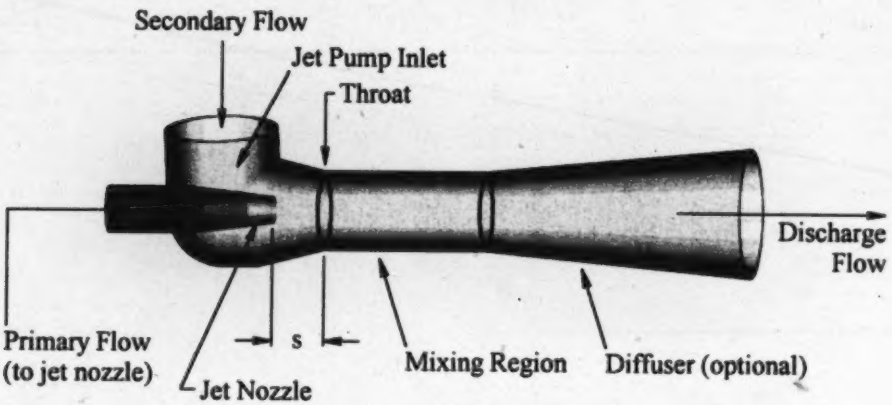

Figure 1.1: Phantom view of a centre jet pump, showing the main components and flows. The distance s is the nozzle to throat separation.

may not have a convergent inlet, in which case the throat would be located at the exit plane of the annular jet. Since this style of jet pump has more of a straight-through flow than the centre jet pump, it is commonly used in solids transport and conveying applications, where a central jet would be a significant obstacle to solids flow. Since a solids transporter would not require a high discharge pressure, and would likely require higher flow velocities to keep the solids in suspension with the fluid, the annular jet pump is often found without a diffuser.

Many other varieties of jet pump designs have been developed for specific applications, and some of these are discussed further in Section 1.2.3.

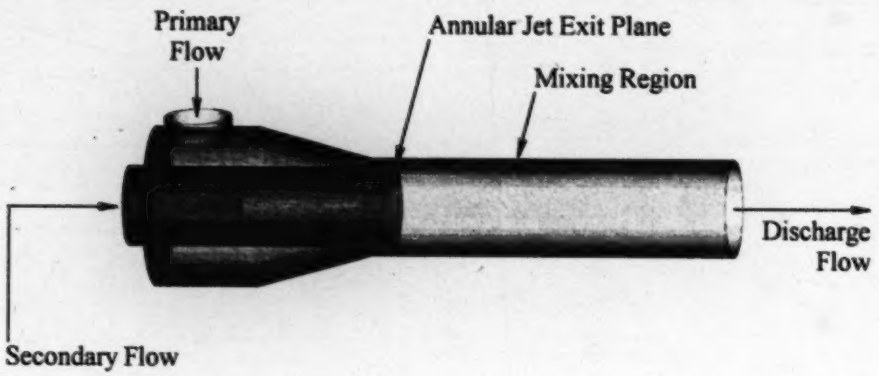

Figure 1.2: Phantom view of an annular jet pump, showing the main components and flows.

1.2.2 Operation of Jet Pumps

1.2.2.1 General Principles

There are three main flows in the pump. The primary flow, or jet flow, Q_p, is the volumetric flow rate which passes through the jet and which supplies the power for the pump. The secondary flow, or suction flow, Q_s, is the ambient fluid surrounding the inlet of the pump which is entrained by the primary flow. These two flows combine in the mixing region of the pump. The combined flow is called the the tertiary flow, or mixed flow, Q_t, and exits the pump through the discharge opening. The ratio of secondary to primary flow rates is called the flow ratio, with the symbol M. The ratio of nozzle exit area to throat area is called the area ratio, with the symbol R.

The secondary flow may enter the inlet region from the side of the pump, as shown in Figure 1.1, or along the main axis of the pump. The selection of

inlet geometry is determined primarily by the application of the pump and on other constraints placed on the design. Other considerations and constraints may give rise to alternative designs, such as those discussed in Section 1.2.3.

The basic principle of operation involves momentum transfer from the primary flow of the jet to the secondary flow of the inducted fluid. For incompressible fluids, this transfer may be modeled with the one-dimensional energy equation:

$$Q_p(P_p + \frac{\alpha\rho}{2}U_p{}^2 + \rho g z_p) + Q_s(P_s + \frac{\alpha\rho}{2}U_s{}^2 + \rho g z_s) = Q_t(P_t + \frac{\alpha\rho}{2}U_t{}^2 + \rho g z_t) + losses \quad (1.1)$$

where Q is the volumetric flow rate, P is the static pressure of the fluid, ρ is the density, U is the mean velocity, g is gravity, α is a kinetic energy correction factor, and z is the elevation. The subscripts p, s, and t refer to the primary, secondary, and tertiary flows respectively.

The terms of the energy equation represent the three main components of the fluid energy flux, and have dimensions of work per unit time. QP is the pressure energy of the flow, $Q\frac{\alpha\rho}{2}U^2$ is the kinetic energy of the fluid, and $Q\rho gz$ is the gravitational potential energy. The development and application of the energy equation is covered in detail in many introductory fluid mechanics text books, such as White (1986).

The loss terms refer to energy losses in the system. For a jet pump, these losses come from three main sources: expansion of the jet flow into the mixing

region, mixing losses, and viscous friction on the pipe walls. The physical nature of these losses are the viscous dissipation of kinetic energy, such as the dissipation of vortex structures formed when the jet flow mixes with the secondary flow, the subsequent expansion of the jet, or from dissipation of shear stresses in the boundary layers near the jet pump walls. The losses are modeled with terms of the form $Q_2^{\varrho}U^2K_{loss}$. As with the energy equation, $Q_2^{\varrho}U^2$ represents the kinetic energy of the fluid, and K_{loss} is a coefficient representing the fraction of the kinetic energy lost to viscous dissipation.

The loss factors account for physical phenomena which cannot be adequately modeled with a simple one-dimensional equation, and are determined experimentally for specific flow patterns. Factors have been determined for many common engineering applications, such as friction losses in pipes, losses from sudden and gradual flow expansions and contractions, losses from pipe fittings, and losses through valves. White (1986) includes tables and plots of many of these loss coefficients. These factors will be further discussed in Section 3.7.

1.2.2.2 Other Factors Affecting Performance

Two other factors which influence the performance of a jet pump are the area ratio R, and the nozzle to throat separation distance s.

The area ratio directly affects the flow ratio of the pump, which in turn affects mixing and friction energy losses. As outlined by Cunningham (1975), the mixing losses are maximum at low flow ratios, when the relative velocity

between the primary and secondary flows is a maximum, and decrease as the flow ratio increases. The friction losses, however, are minimum at low flow ratios, when the total flow velocities are minimized, and increase with the flow ratio. For a centre jet pump, the minimum total energy losses and maximum efficiency occur at an area ratio $R \approx 0.3$.

Years of experience and research with jet pumps has shown that the nozzle to throat distance has a significant effect on the performance of the pump. For best performance, it has been found that the jet nozzle exit should be positioned some distance s upstream of the throat. Most researchers agree that a value of $1.0D_t \leqslant s \leqslant 2.0D_t$ results in the highest efficiency (Cairns and Na, 1969), and improves the jet pump resistance to cavitation (Cunningham et al., 1970).

1.2.2.3 Cavitation

As with most other pumping methods, cavitation can occur in jet pumps when liquids are handled, and has the effect of limiting the maximum flow ratio of the pump. This phenomenon has been extensively studied, and a review of several cavitation parameters and configuration effects are found in a paper by Cunningham et al. (1970).

Cavitation occurs when the local pressure of a liquid is depressed below the local vapour pressure of the liquid. In a jet pump, this can occur between the nozzle exit plane and into the mixing chamber, and generally has two stages: incipient cavitation and full cavitation.

Incipient cavitation is the first phenomenon to develop. This is a result of low local pressures in the vortex structures which form in the shear layer between the primary and secondary flows. The high angular velocities in the vortex create a low pressure region near the centre of the vortex. If the vortex is sufficiently intense, this can depress the local pressure in the vortex and cause cavitation bubbles to appear. Since the vortex strength is dependent on the relative velocity between the jet and secondary flow, an increase in jet flow will increase the amount of bubbles formed by this mechanism.

A variation of incipient cavitation occurs with liquids with very low vapour pressures which contain high amounts of dissolved gases, such as lubricating oils. Instead of bubbles forming because the local static pressure drops below the vapour pressure, a low static pressure may cause dissolved gases to leave solution. As the primary and secondary flows mix, the pressure rises and the bubbles will re-enter solution with the liquid.

As the mixing progresses, the coherency of the shear layer vortices reduces, and the local static pressures begin to rise. With the pressure rise, the cavitation mechanism dissipates, and the vapour bubbles collapse. Therefore, incipient cavitation has little effect on the performance of a jet pump.

Further increases in the secondary flow rates can cause flow-limiting cavitation, which has a significant effect on the performance of the jet pump. As the jet velocity increases, so too does the secondary flow rate. In the mixing region, momentum transfer from the jet to the secondary flow causes local longitudinal acceleration of the secondary flow. As predicted by the

one-dimensional energy equation, the increased kinetic energy is balanced by a reduced static pressure. A sufficiently high velocity causes the pressure to drop to the point that the cavitation bubbles formed in the mixing shear layer will not dissipate before reaching the mixing chamber wall. At this point, the tertiary flow becomes choked with bubbles, and the flow ratio reaches a maximum. This condition is called flow-limiting cavitation.

1.2.3 Alternative Jet Pump Designs

Although the simple centre jet pump shown in Figure 1.1 is very common, specific applications have given rise to many other configurations of jet pump.

A simple variation on the centre jet pump uses multiple parallel nozzles clustered together near the centre of the pump, rather than a single nozzle. Lewis (1965) and Schmitt (1975) report that this nozzle configuration improves the efficiency of the pump, particularly with higher flow ratios, and also gives improved resistance to cavitation.

The multiple nozzle system can be configured into what is called a bidimensional pump (Schmitt, 1975), shown in Figure 1.3. In this configuration, the multiple nozzles are arranged in a row and inject fluid into a rectangular inlet. This results in a high-capacity pump which is very compact in one dimension.

The bidimensional pump concept can also be converted back to an axisymmetrical pump by revolving the nozzle line and pump walls about an axis, as shown in Figure 1.4. This layout offers similar performance to the

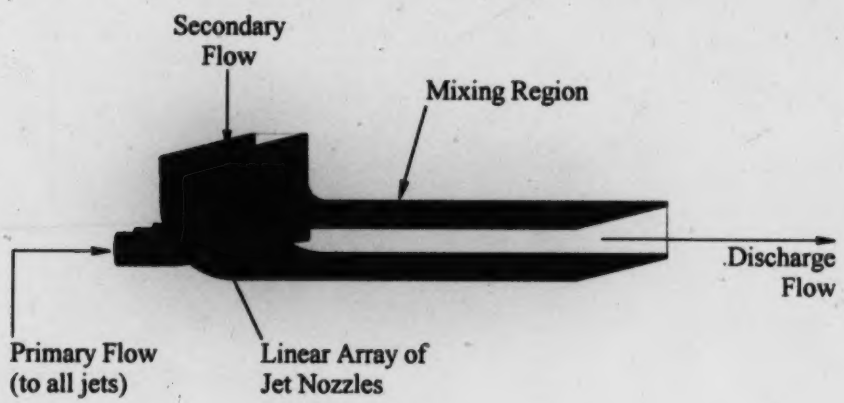

Figure 1.3: Sectioned phantom view of a bidimensional jet pump, showing the linear geometry, main components, and flows.

bidimensional pump, with the added benefits of an overall compact size and elimination of friction losses from the end walls of the pump. Furthermore, the central pipe, which forms the inner wall of the annulus, can be used to supply the primary flow to the jets. This configuration, called the annular mixing jet pump, was employed in a device invented by Field (1995), and is the subject of this thesis.

One design which combines features of both the centre and annular jet pumps uses several discrete jets located around the periphery of the inlet, and is illustrated in Figure 1.5. These jets enter the mixing region at some angle to the secondary flow, and if the jets are positioned opposite each other, the interaction of the jets results in a larger central jet flowing along the centre line of the mixing region. This style of jet pump can be installed into a

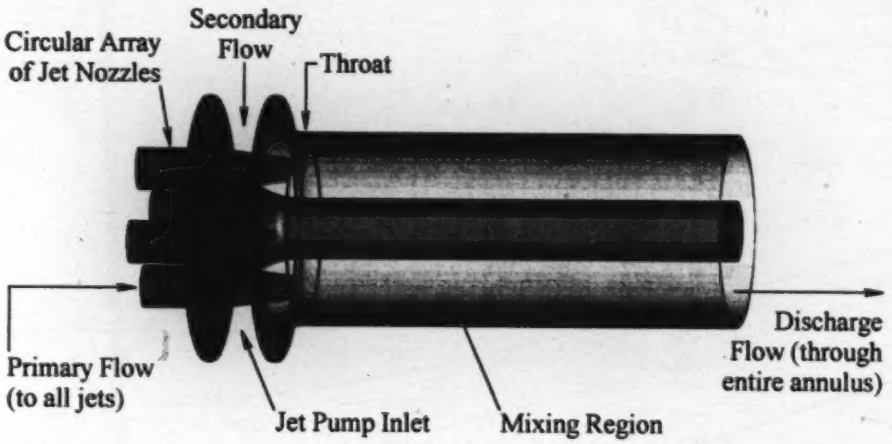

Figure 1.4: Phantom view of an annular mixing jet pump, showing the main components and flows.

pipeline without introducing any flow obstructions or area changes, making it well suited to pipelines which transport solids or capsules. However, the deflection of the jets introduces large mixing losses, and therefore a large performance penalty.

1.2.4 Applications of Jet Pumps

There are many applications where jet pumps can be successfully employed, including fluid pumping, mixing, and multiphase transport.

1.2.4.1 Fluid Pumping

Probably the most common application is simple fluid pumping. Some applications include pumping of shallow water wells, the pump in a conventional

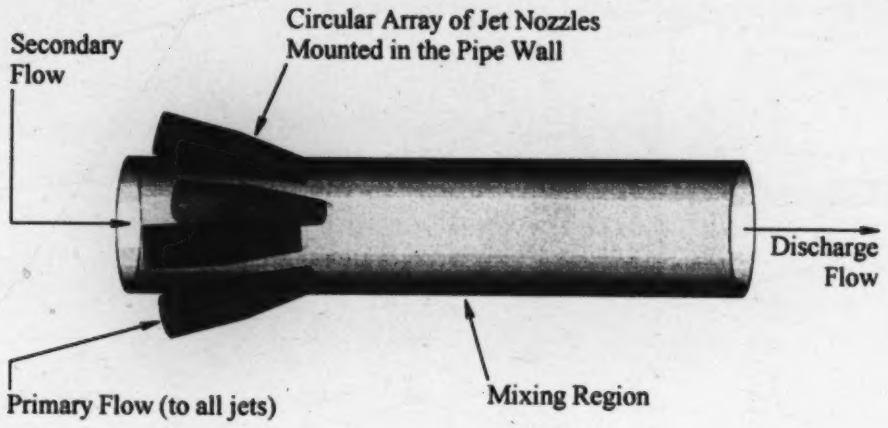

Figure 1.5: Phantom view of a discrete peripheral jet pump, showing the main components and flows.

flush toilet, and fuel transfer pumps in aircraft. The simplicity of jet pumps gives them a high inherent reliability, and for this reason jet pumps are widely used to circulate cooling water in nuclear reactors.

1.2.4.2 Mixing

Except when handling fluids of very high viscosity, the jets in a jet pump often operate at high Reynolds numbers, and the jet flows are usually turbulent. This turbulence, combined with the high shear rates present throughout the mixing region, make jet pumps very effective mixing devices. Jet pumps, when used in a pipe, can be used to combine mixing and pumping functions in a single, simple device.

1.2.4.3 Multiphase Transport

In some jet pump applications, the primary and secondary flows are of different phases, resulting in a multiphase tertiary flow, or the secondary flow may be multi-phase. One example of this is the use of jet pumps for dredging. In this application, water is injected into the jets, and a two-phase mixture of ambient water and solids is drawn into the pump. This application does not generally involve a significant head rise above the water surface, and thus the weak lifting capacity of the jet pump is not a constraint.

For materials handling, solid particles can be transported in pipelines using air or water jet pumps. Examples are the transport of powdered desiccants, food ingredients, or polymer pellets using air jets, or the transport of coal or oil sand slurries with water jets.

An application similar to jet pumps is the gas lift pump. In this application, a gas is injected into a pipe suspended vertically in a liquid. The buoyant gas bubbles travel upward in the pipe and transfer momentum to the liquid in the pipe, generating a vertical pumping action. These pumps may also be used to lift small amounts of solids suspended in the liquid phase. Gas lift pumps are commonly found in aquarium water filters, where the pump is used to draw water through a filter before it is aerated and returned to the tank. Gas lift pumps are also used for pumping oil from offshore reservoirs to the ocean surface.

1.2.4.4 Water Filters

The application of jet pumps to water conditioning devices, in particular the use of jet pumps for cleaning and regenerating the conditioner medium, is the chief motivation for this thesis.

One type of water conditioner is an iron filter, a system which removes dissolved iron compounds from water. This system uses an oxidizer to oxidize the iron ions from the ferrous (Fe^{2+}) to the ferric (Fe^{3+}) state. Once oxidized, the ferric ions form only non-soluble compounds which precipitate from the water. The precipitate is then removed with a particulate filter. The particulate filter in residential iron filters is a packed bed of granular material with particles the shape and size of sand.

The deposition of iron onto the filter medium eventually contaminates the filter, and the precipitate must be periodically removed. The simplest approach is to backwash the medium with a high volumetric flow rate of water. This fluidizes the filter bed, and the resulting collisions between medium particles breaks the precipitate off the particles. The iron flakes are then carried to a waste drain by the backwash water flow.

However, there are many installations where the available water flow is insufficient to adequately backwash an iron filter. This leads to incomplete cleaning of the filter medium, and eventual complete fouling and failure of the filter.

Many devices have been developed which employ jet pumps to overcome the problem of insufficient backwash flow, including those developed

by Robinson (1944); Matthews (1959); Johnson (1968); and Field (1995). In these devices, rather than providing the high volumetric flow rate needed to fluidize the entire filter bed, a jet pump with a lower flow rate is used. The jet pump is designed to draw a two-phase mixture of water and filter medium particles from the bottom of the medium bed into the jet pump inlet. The local shear rates and turbulence levels in the jet pump mixing region cause many collisions between medium particles, which effectively removes the iron from the particles. The cleaned particles are deposited on top of the medium bed. As the particles are drawn into the jet pump at the bottom of the bed and re-deposited at the top, the entire bed will move slowly downward. The jet pump is operated until the entire bed has been processed through the jet pump.

The Matthews device (Matthews, 1959) is an early design in which a jet pump is used specifically to reduce the quantity of water required to backwash a water filter. This device uses a single centre jet pump located on the central axis of the pressure tank. When the filter medium required regeneration, a valve would be set to admit water into the jet pump nozzle. The jet pump would then draw water and the filter medium from the tank into the pump, where it would be cleaned. An illustration of the Matthews device is shown in Figure 1.6.

The development of automatic control valves which mount on the top of the pressure tank resulted in new designs for water conditioner backwash devices. The Johnson device (Johnson, 1968), shown in Figure 1.7, uses a

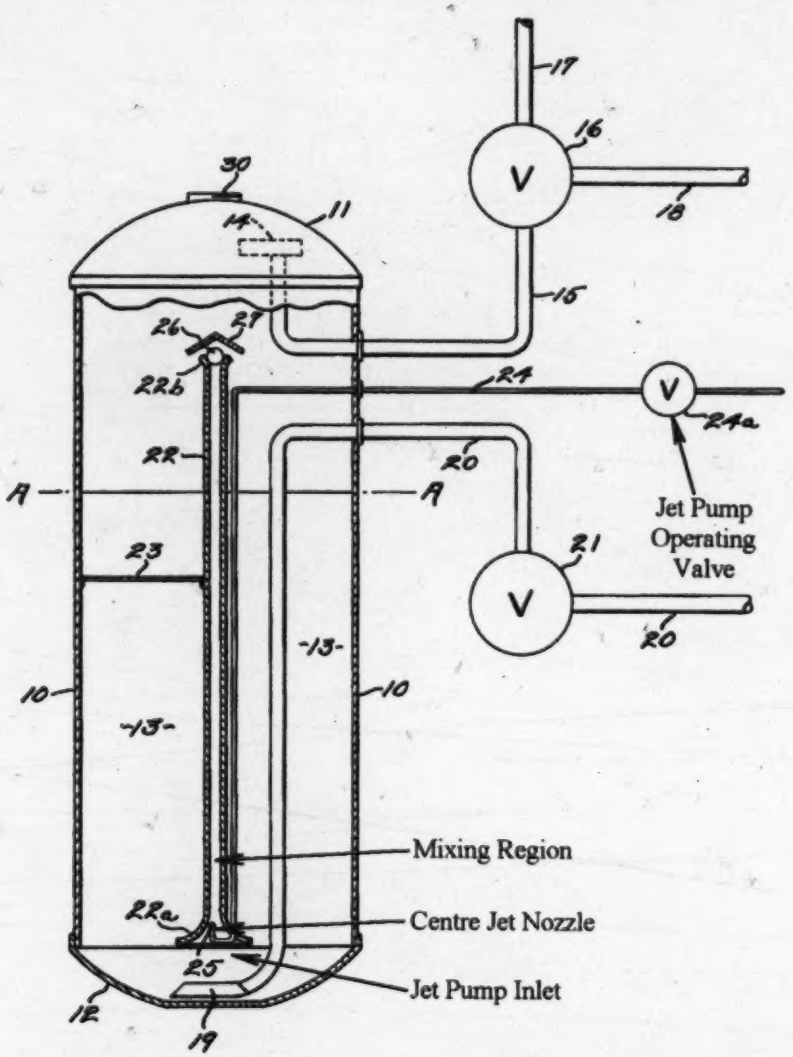

Figure 1.6: Jet Pump in a Water Conditioner (Matthews, 1959), shown in section view. This design uses a centre jet pump installed in the centre of the pressure tank, with manual external valves to control operation of the jet pump. Labels for the jet pump inlet, nozzle, mixing region, and operating valve have been added to the original patent drawing.

single centre jet pump mounted vertically and eccentrically inside the water conditioner pressure tank.

The asymmetric nature of the Johnson device prevents uniform flow of water and filter medium into the jet pump inlet, which can lead to incomplete cleaning of the medium. To provide a symmetrical inlet geometry, the Field device was developed (Field, 1990, 1995). This device uses an annular mixing jet pump to provide an axisymmetrical jet pump inlet, and is shown in Figure 1.8. The design of an annular mixing jet pump for use in a water filter is explored in detail in this thesis.

1.3 Methodology and Objectives

The objectives of this research were three-fold:

1. develop a general understanding of the operation and characteristics of the annular mixing jet pump,

2. investigate the application of conventional design methods to an annular mixing jet pump in the Field backwash device, and

3. develop a method of designing a full line of products similar to the Field backwash device, but with different capacities

In pursuit of these objectives, the research program was approached from two directions: numerical simulation and experimental validation. A valid computer simulation was viewed as a very effective design tool, since it would

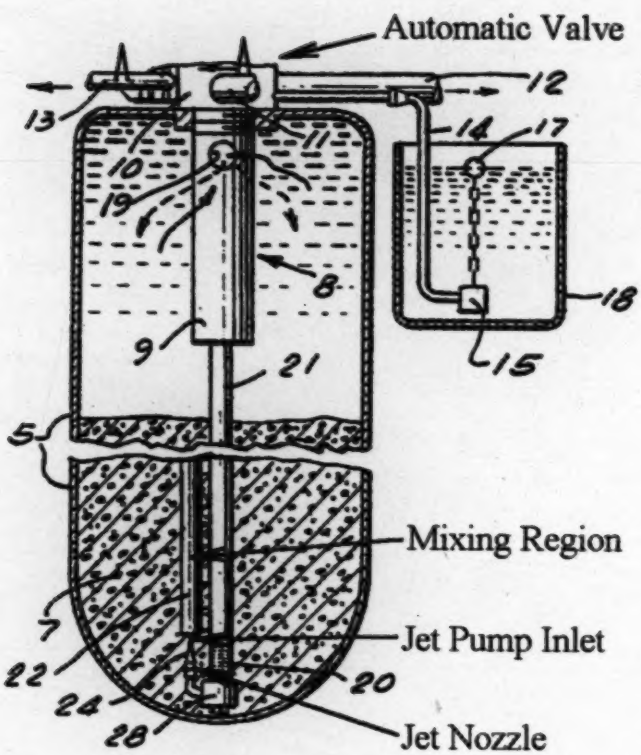

Figure 1.7: Johnson Backwash Device (Johnson, 1968), shown in sectioned pressure tank. This design uses a centre jet pump installed adjacent to the central water pipe, with a top mounted automatic control valve. Labels for the jet pump inlet, nozzle, mixing region, and operating valve have been added to the original patent drawing.

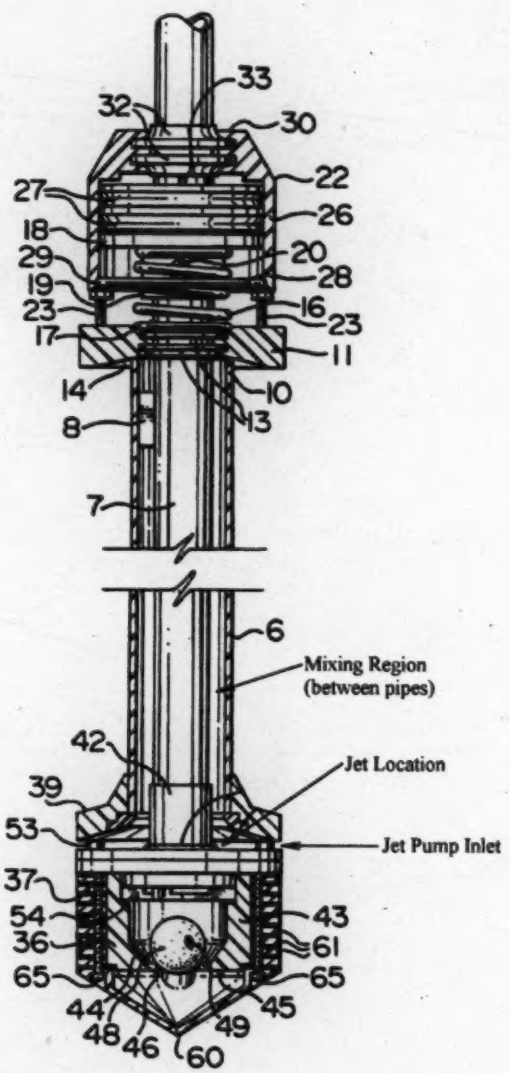

Figure 1.8: Field Backwash Device (Field, 1995), shown in section view. This design uses an annular mixing jet pump with a top mount automatic control valve. Labels for the jet pump inlet, jet location, and mixing region have been added to the original patent drawing.

allow the evaluation of many alternative designs, and also allow a semi-automated search for optimal design parameters. Since the validity of the simulation would be crucial to this approach, experiments were conducted with a physical model of the jet pump which could provide direct correlation with the simulation.

Finally, it was recognized that since this type of jet pump had not previously been studied, the flow patterns within the jet pump were unknown. It was decided to construct the experimental model to allow flow visualization within the jet pump. The types of phenomena of interest were the flow patterns in the jet pump inlet and mixing regions, and cavitation.

1.4 Thesis Outline

This thesis is written in the traditional format with six chapters. Chapter One presented introductory and background material on the general subject of jet pumps and their numerous applications. Chapter Two outlines the experimental portion of the research, describing a model of an annular mixing jet pump and the associated apparatus and procedures used to evaluate its performance.

Chapter Three describes the development of a numerical simulation of the annular mixing jet pump, providing details on the construction and solution of the equations which model the device. An uncertainty analysis of the experimental and simulation results is presented in Chapter Four.

In Chapter Five, the results of the experiments and simulations are com-

pared and discussed, as are the steps and factors to be considered when designing an annular mixing jet pump. The conclusions and recommendations for further research are summarized in Chapter Six.

There are also two appendices to this work which contain additional information about the experiments and simulations. Appendix A lists the parameters used to estimate the overall uncertainty of the simulation. Appendix B contains information about the experiment configurations, and plots of the experiment and simulation results.

CHAPTER 2

EXPERIMENTAL SETUP AND APPARATUS

2.1 Introduction

This chapter describes the experimental model of the annular-mixing jet pump, and the associated equipment used to operate the model and collect data from the experiments.

2.2 Apparatus

The experimental apparatus consisted of a large water tank into which the experimental model was installed. Installed into and onto the tank were the pumps, pipes, valves, and instrumentation needed to control and monitor the experiments.

2.2.1 Test Tank

The main element was a steel water tank, shown in Figure 2.1. The tank was approximately 1.2 m (48") wide, 1.2 m (48") long, and 1.8 m (72") tall. It

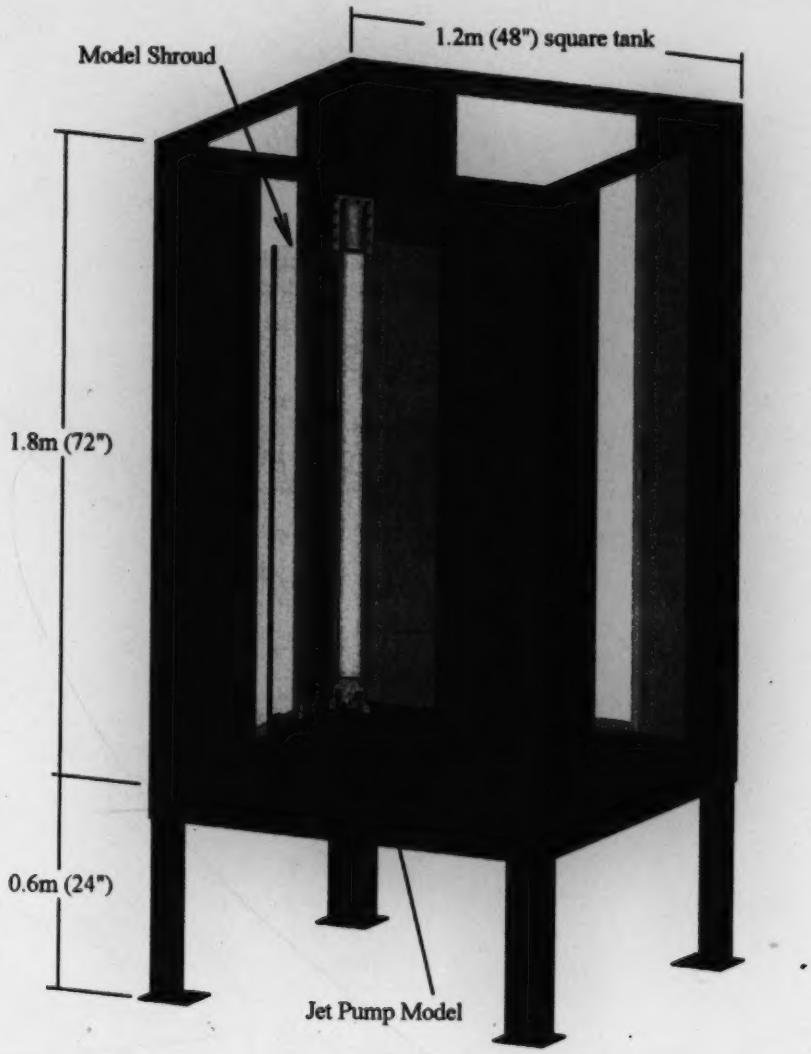

Figure 2.1: Experimental apparatus, showing the general configuration and size of the test tank, and the position of the jet pump model on the tank window. See Figures 2.3 and 2.4 for additional details of the jet pump model.

was fabricated from 3.2 mm (1/8") galvanized steel sheet with welded joints, and reinforced with steel angles and tubing. Each wall of the tank was fitted with a large window, approximately 0.6 m (24") wide and 1.7 m (68") high, made of 18 mm (3/4") acrylic sheet. The tank was also equipped with two bottom drains, each with a shut-off valve, and a single overflow drain which allowed a maximum water depth of about 1.7 m (68"). To provide space for piping underneath, the tank was mounted on a steel stand approximately 0.6 m (24") tall.

The model was mounted on one of the tank windows, giving a clear view into the model during experiments. To help simulate the presence of a pressure tank, an acrylic shroud was built around the model. This shroud was shaped like half of a 610 mm (24") diameter pressure tank, and to simplify construction, was built in a semi-octagon shape.

2.2.2 Plumbing

The plumbing for the apparatus is shown schematically in Figure 2.2. Water flow and pressure was provided by three submersible pumps installed at the bottom of the tank outside of the shroud. The main pump was a Goulds Pumps model 7G10 submersible water well pump, which was supplemented with two Goulds Pumps model 7GS07 submersible pumps. Each pump had its own controller, allowing independent operation. To prevent back flow through an unused pump, the two supplemental pumps were fitted with outlet check valves.

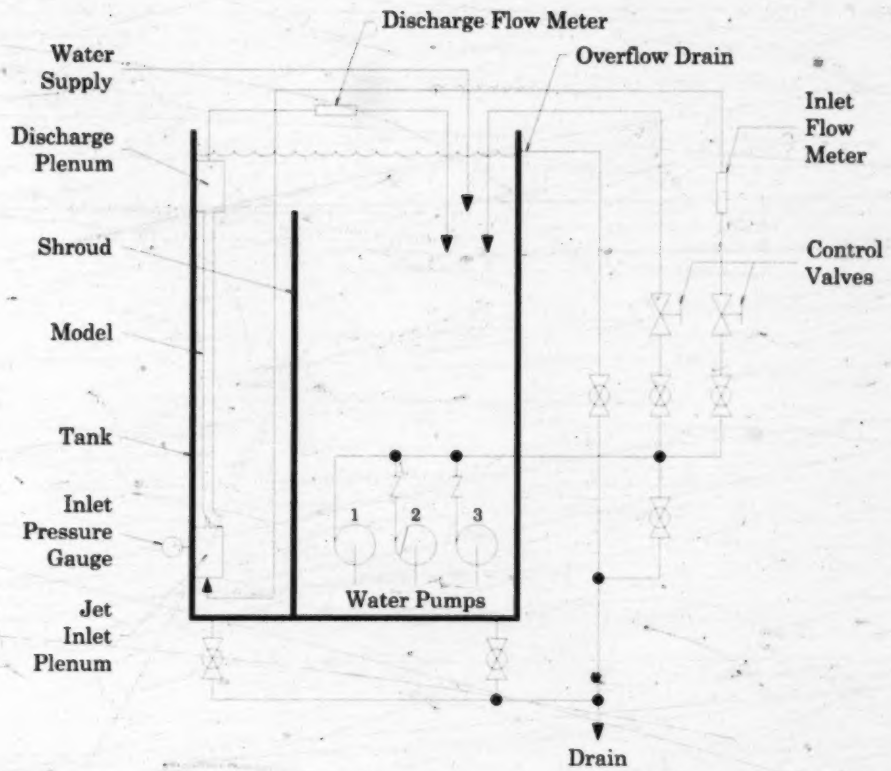

Figure 2.2: Schematic diagram of the experimental apparatus plumbing, showing the general arrangement of the model, pumps, valves, and instrumentation. The jet pump model and shroud are shown on the left side of the tank in the illustration.

After the pumps, the water was piped out of the tank to a main manifold. From there, manual ball valves directed the flow to three locations: back into the tank, to a floor drain located near the apparatus, or to the inlet plenum of the model.

Two control valves were installed in the piping. One valve was installed between the manifold and the model to provide pressure regulation at the model inlet plenum. A second valve was installed between the manifold and the tank return to regulate the return flow back to the tank. The use of these valves allowed easy and repeatable control of the model inlet plenum pressure.

The plumbing, valves, and pump motor controls were mounted on a control panel attached to the left side of the tank. A staircase was mounted to the right side of the tank to allow access to pipes and instruments at the top of the tank, and a ladder was mounted in the tank to access the pumps, model, and other equipment inside the tank.

2.3 Jet Pump Model

The jet pump model was constructed as shown in Figure 2.3, with an enlarged view of the inlet and mixing region shown in Figure 2.4. The model was built to represent a water filter backwash device similar to that described by Field (1995) and shown in Figures 1.4 and 1.8, with a central pipe of 51 mm (2") nominal size. The 51 mm size was chosen for two reasons: firstly, because the model represented a commercial device, which would use 51 mm supply

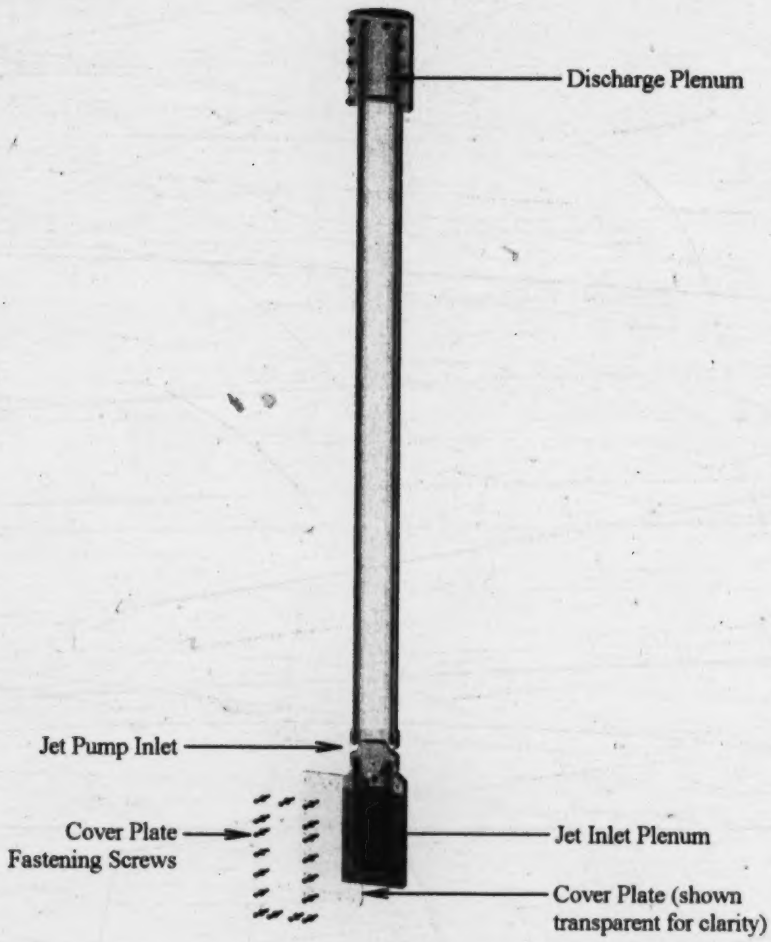

Figure 2.3: Experimental model of the annular-mixing jet pump, shown mounted on one window of the test tank. A more detailed view of the jet pump inlet area is shown in Figure 2.4.

piping, and secondly, because a model of this size would be easier to construct than a smaller one.

In a water conditioning application, the device would be installed vertically inside a pressure tank, and to best replicate this, the model was also constructed and installed vertically.

In addition to the central pipe size, the model had to meet several other design constraints. The model was built to represent a device which could fit into a commercially-available pressure tank with a 4"-8UN thread for its top opening; this dictated a maximum model diameter of 96.5 mm (3.80"). To allow access to the model, it was installed into an open-top tank, rather than a sealed pressure tank. To permit visualization of flows within the jet pump, the model was sectioned in half along its longitudinal axis, and the sectioned surface mounted onto a transparent acrylic window.

The radius of the jet pump secondary flow inlet was expected to have some impact on flow losses in the inlet, and therefore the overall performance of the device. However, the 96.5 mm maximum model diameter allowed for maximum inlet radius of only 3.6 mm (0.140"), and the model was fitted with a fixed geometry inlet with this radius.

The model used two concentric pipes to form the jet pump mixing region. The inner pipe was a 51 mm (2") schedule 40 pipe made of transparent polyvinyl chloride (PVC). A transparent material was selected to give a view into the inlet and mixing regions of the jet pump. The outer pipe was a 76 mm (3") series 160 pipe made of white PVC. This type of thin-walled

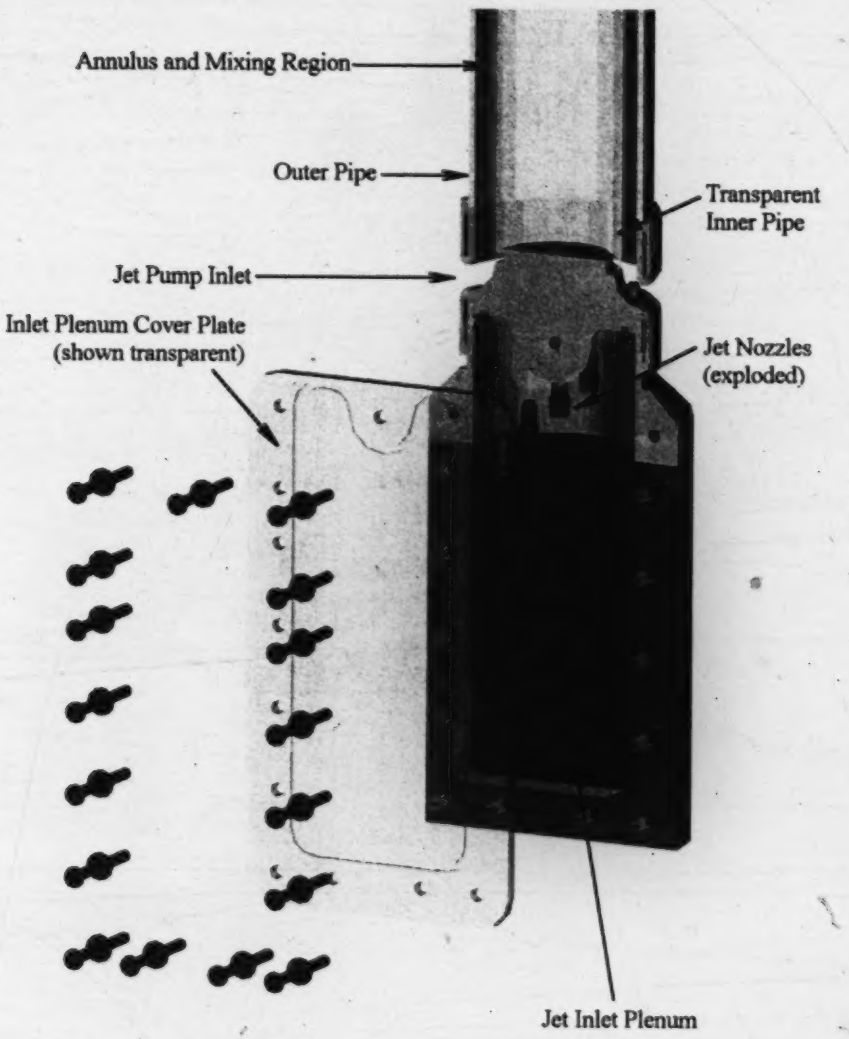

Figure 2.4: Detailed view of the jet pump inlet and mixing regions, showing major components of the model.

pipe was used to maximize the distance between the inner and outer pipes, and therefore minimize the flow friction losses. The white colour gave good contrast between the inside pipe wall and a dark flow visualization dye.

Three nozzle parameters were expected to affect the performance of the jet pump: the nozzle diameter, which affects the area ratio, the number of jets, and the nozzle to throat separation distance. To evaluate the effects of these parameters, the model was built with replaceable nozzles. The lower surface of the jet pump inlet was made with seven holes into which combinations of nozzles and plugs could be installed. The nozzles were made of type 304 stainless steel for corrosion resistance and durability, and an o-ring was used to provide a seal between the nozzles and the jet pump inlet. Installation of the nozzles was through a hole in the window into the inlet plenum. A steel hatch secured with screws covered the access hole.

The primary flow entered the bottom of the model through an inlet plenum. The plenum admitted water from a circular pipe, and directed the flow upward to the jet nozzles. The plenum was built large enough to provide access for changing the nozzles and plugs.

The secondary flow entered the jet pump from the tank, horizontally and radially inward toward the jet pump inlet. The water then flowed through a 90° bend to align with the vertical mixing region. The parts forming the upper and lower surfaces of the inlet were made of type 6061 aluminum to offer corrosion resistance and ease of fabrication.

During and after mixing, the tertiary flow travelled through the annulus until it reached an adaptor. The adaptor effected a transition from the

annular flow passage to a circular pipe. The flow then continued through a pipe and flow meter before discharging into the tank which housed the entire model.

2.4 Performance Measurements

Six key parameters were recorded during the experiments. These were the primary and tertiary water flow rates Q_1 and Q_3, the primary flow pressure at the jet inlet plenum P_0, the tertiary flow static pressure at sixteen points within the jet pump mixing region $P_{T,1}$ to $P_{T,16}$, the tertiary flow static pressure at the top of the annulus P_4, the height of the free water surface H_w, and the temperature of the water T_w. Each of these measurements is described in greater detail below.

2.4.1 Flow Instrumentation

Two of the water flow rates were directly measured: the primary and tertiary flows. The secondary flow rate was determined by the difference between the primary and tertiary flows.

The primary and tertiary flow rates were measured using Annubar® in-line flow meters. The primary flow was measured with a 25 mm (1") Annubar® flow meter, and the tertiary flow was measured with a 51 mm (2") Annubar® flow meter. The Annubar® flow meter, manufactured by the Ellison Instrument Division of Dieterich Standard Corp., is a variation of a conventional pitot-static velocimeter, and provides average flow velocity and

flow rate information from the difference between two pressure ports. The size of the Annubar® flow meter indicates the inside diameter of the meter, which is built to match the inside diameter of schedule 40 pipe of the same nominal size.

The differential pressures were sensed with Validyne pressure transducers, which consisted of model DP15 sensors with appropriate diaphragms and CD15 carrier demodulators. The water flows through the Annubar® flow meters were turbulent, and the indicated pressures fluctuated greatly. However, only mean flow rates were of interest, so the Validyne voltage outputs were measured with an averaging volt meter (AVM). The AVM was developed and built by the University of Alberta Department of Mechanical Engineering. It is an analogue instrument which converts the input voltage to a frequency, then counts the number of cycles for a user-selected interval of 1, 10, 100, or 1000 seconds.

2.4.2 Pressure Instrumentation

The primary flow pressure at the jet inlet plenum was measured with a Bourdon tube type pressure gauge manufactured by Ashcroft. The gauge had a 4 inch (100 mm) face diameter, a range from zero to 160 psi (0-1100 kPa), and a resolution of 1 psi (6.9 kPa). The gauge was installed into a hole in the steel access hatch covering the inlet plenum.

The tertiary flow pressure in the jet pump mixing region was measured with a Validyne pressure transducer. Along the mixing region, the outer

pipe was fitted with sixteen pressure taps at spacings equal to one equivalent hydraulic diameter of the mixing region annulus (see Section 3.7.6 for more details of the concept of hydraulic diameter). An additional pressure tap was installed at the end of the annulus, just prior to the point where the tertiary flow entered the discharge plenum. The pressure taps were located at the midpoint of the half-pipe.

Each pressure tap was connected with a transparent plastic tube to a manual valve, and each valve was connected through a common manifold to the Validyne transducer. This arrangement allowed a single transducer to measure all the pressures, eliminating errors which may have been introduced by variations between individual pressure transducers. The transparent material allowed verification that the tubes contained no air bubbles which could affect the accuracy of the measurements.

2.4.3 Miscellaneous Instrumentation

The water temperature was measured with a Fluke model 2175A digital thermometer. This thermometer used a type T (copper/constantan) thermocouple probe which was immersed into the water near the surface.

The water level was measured with a steel ruler marked in millimetres. The elevations of the various locations within the model and apparatus were measured with a builder's level, consisting of a small telescope mounted on a vertical scale.

2.4.4 Instrument Calibration

To calibrate the Validyne pressure transducers, an Omega model PCL-601 digital pressure indicator was used to provide a calibrated source pressure. A Fluke model 8050A bench top digital multimeter was used to measure the output voltage from the Validyne carrier demodulator unit.

Each Annubar® flow metering system was calibrated by pumping water through the meter and adjoining experiment piping. The water flow rate was determined by timing the transfer of a known mass of water at a known temperature, and measuring the voltage output of the Validyne on the AVM. The mass flow rate was converted to a volumetric rate using data from Weast (1982), and the Validyne voltage output was converted to pressure using data from the Validyne calibration. These data were then used to develop functions for the flow rate versus the Validyne output voltage.

The jet inlet pressure gauge was calibrated with a Budenberg model 280L deadweight pressure calibrator. The gauge was calibrated in the range from zero to 100 psi (0-689 kPa). The error analysis found that small errors in the water temperature and level measurements have a very small effect on the data analysis. Therefore, the thermometer and ruler were not calibrated.

2.5 Flow Visualization

The model was built as a half-section to allow for visualization of the internal flows. Cavitation was visible to the naked eye during the experiments, and a

dye was injected into the model to allow visualization of the inlet and mixing flow patterns. In this section, the dye injection and imaging systems are described.

2.5.1 Dye Injection System

The visualization dye used for these experiments was a saturated solution of potassium permanganate. The dye was stored in a chemical-resistant vessel adjacent to the experimental apparatus. Potassium permanganate is a strong oxidizer, so it was reduced with sodium hydrosulfite before disposal.

Three dye injection points were built into the apparatus. The first point was the inlet to water pump #1, which allowed dye to flow through the jets of the model. The other two points were slits near the jet pump inlet, located approximately five millimetres above and below the inlet. From these slits, dye would be entrained by the secondary flow, and would be carried with the flow into the jet pump inlet and mixing region.

A small 24 volt DC gear pump, model UGP-2015P manufactured by B&D Pumps, was used to pump the dye to the injection points. Power for the pump was provided by a manually adjustable 24 volt DC power supply. Varying the input voltage to the pump allowed precise control of the pump speed, and hence the dye delivery rate. The pump input voltage was monitored with a Fluke model 8080A digital multimeter.

From the pump, a tube carried the dye to a manifold, and then through valves to the dye injection points. After tests were conducted, the tubing, pump, and valves were purged of dye with clean water.

2.5.2 Image Capture System

The image capture system comprised three main items: the camera, the photographic film, and the light source.

The camera used for all imagery was a Nikon F3 body with power winder. The body was fitted with a Nikon AF Micro Nikkor 60mm lens with a 1:2.8 focal length, which allows focus distances as close as 200mm. The film used for all imagery was Agfa Agfacolor HDCplus 400 colour print film, and the light source was a Strobotac® 1531-AB strobe, manufactured by the General Radio Company.

The strobe was used at its high intensity setting in external trigger mode. A trigger signal was provided by the camera through an interface unit which converted the camera flash trigger contact closure to a voltage pulse. The interface unit was built by the University of Alberta Department of Mechanical Engineering.

In its high intensity setting, the strobe has a flash duration of approximately three microseconds, which is sufficiently fast to stop the motion of the high-speed flow from the jet. The highest jet velocities were approximately 30 m/s, so a 3 μs flash would show only about 0.1 mm of travel for a particle in the jet. Considering the focus distance, depth of field, and film used for the imagery, this amount of travel approached the resolution of the film, and was considered adequate.

2.6 Experimental Procedures

The procedures to set up and conduct the performance and visualization experiments are outlined below.

2.6.1 Performance Measurements

For the performance measurements, the following items were performed to prepare the model and equipment for measurements:

1. turn on all electronic equipment and allow it to warm up
2. install nozzles into the model as required
3. install and secure the access hatch
4. fill the tank with water
5. purge air from the water supply piping, model, instrument lines, and the water in the tank

Once the model was configured and the above steps complete, the performance data could be recorded. The general procedure was as follows:

1. record the general test data on the data recording form
2. set the desired pressure at the inlet plenum
3. allow 5-10s for the system to stabilize before starting measurements
4. make the necessary Validyne voltage measurements with the AVM

5. record the average voltages on the data recording form

6. repeat the above steps for each additional model inlet pressure

2.6.2 Flow Visualization

The setup of the model and image capture equipment depended on the phenomena being observed, but for all visualization attempts, the model and apparatus were set up and operated in a manner similar to that described above for the performance measurements.

To observe the inlet and mixing flow patterns, the model was configured with two nozzles, which were inserted into the holes in the second position away from the window. In this location, the jets were visible through the window and the transparent inner pipe. The camera was positioned an appropriate distance from the model and aimed perpendicular to the window to view the mixing region. Dye was injected into the water pump, and hence into the jets, using the maximum dye flow rate to minimize dilution.

To observe cavitation, two nozzles were used inserted into the holes adjacent to the window, to give the best view of the jets and bubbles. The camera was positioned very close to the model, and two views were used. To observe vortex shedding from the nozzle, the camera was aimed level, and to observe the shape of the ring vortices, the camera was aimed downward at a 45° angle. In both cases, the camera was positioned slightly left of normal, to improve the view around the inner pipe. Since the cavitation phenomena is visible under normal conditions, no dye injection was required.

For all photography, the flash was positioned to provide maximum illumination of the area of interest, but also to avoid any reflections of the flash off the window and into the camera lens.

CHAPTER 3

SIMULATION OF THE EXPERIMENTS

3.1 Introduction

This chapter discusses the development of a mathematical model for the experimental apparatus, starting with a schematic diagram of the apparatus and its partition into modules which can be separately modelled. Next, the development of the energy equation and loss terms is discussed. Finally, the methods of solving and validating the simulation are presented.

3.2 Approach

To simulate the experimental model, it was sectioned into several discrete and connected computational modules. Each module was modelled with the one-dimensional energy equation, and one node was modeled with the continuity equation for mass flow. Applying boundary conditions gives a system of nine independent simultaneous equations which were solved to determine the pressures at each node and the flow rates in each branch.

3.3 Schematic Diagram

A schematic diagram of the experimental model is shown in Figure 3.1. The figure shows the general configuration of the experimental model, and shows the locations of the nodes at which the pressures and flow rates were calculated. The node numbering shown in Figure 3.1 is used throughout this thesis for the presentation of the simulation and experiment results.

3.4 Flow Diagram

From the schematic, a flow diagram was developed. This diagram, shown in Figure 3.2, shows each module and node of the simulation.

Figure 3.2 lists the eight modules of the simulation. Each module is modelled with the one-dimensional energy equation, described in greater detail in Section 3.5. A node exists at the inlets and outlets of each branch, as well as between each module. The static water pressure is calculated at each node, as are the flow rates in each of the three branches.

Three of the nodes have known values. Pressure P_0 is the pressure in the inlet plenum, which was set by the equipment operator at the start of each test. Pressure P_6 is the discharge pressure of the tertiary flow into the tank at a known hydrostatic pressure. Pressure P_7 is the hydrostatic pressure in the tank at the elevation of the jet pump inlet.

There are six unknown pressures at nodes one to five and node eight, and three flow rates Q_1, Q_2, and Q_3, for a total of nine unknown variables. Each

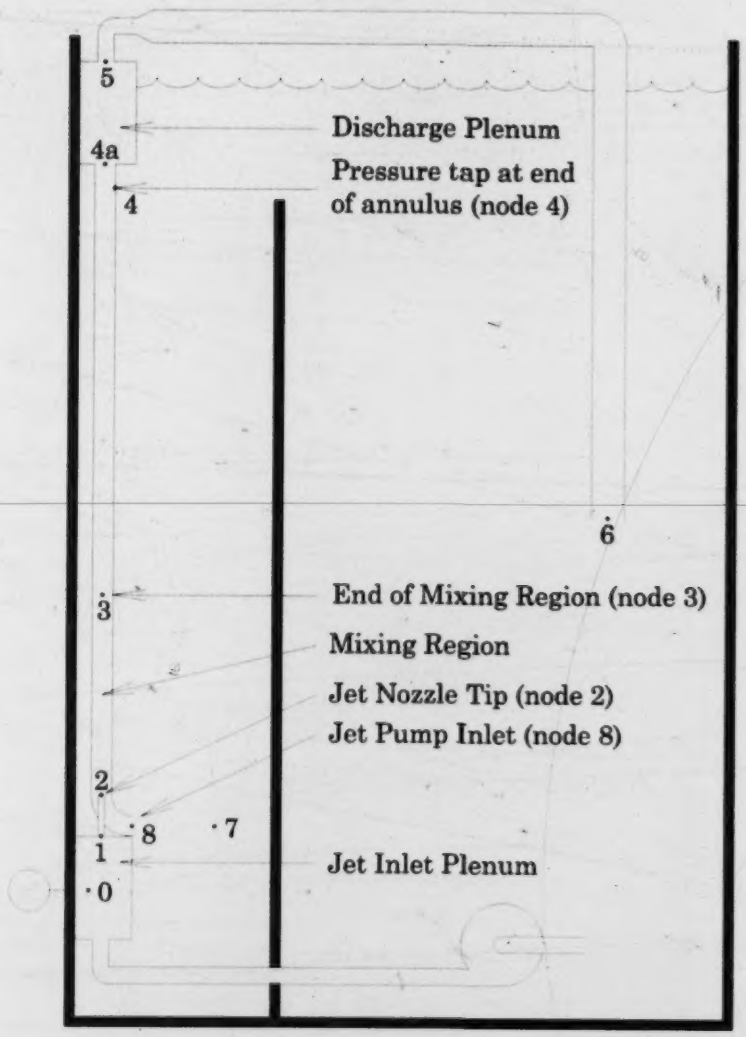

Figure 3.1: Schematic diagram of the apparatus, showing the locations of the simulation and experiment nodes

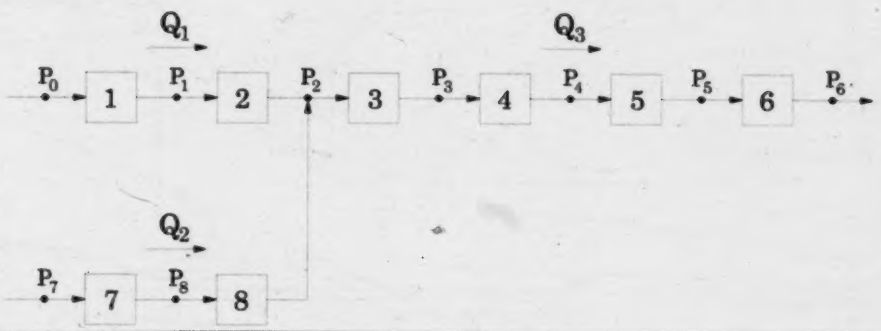

Module 1: Model Inlet Plenum
Module 2: Jet Nozzles
Module 3: Mixing Chamber
Module 4: Teritary Flow Through Annulus
Module 5: Discharge Plenum
Module 6: Discharge Piping to Tank
Module 7: Flow from Tank to Jet Pump Inlet
Module 8: Jet Pump Inlet

Figure 3.2: Flow Diagram for the Simulation

module provides one energy equation, and node two provides one continuity equation, for a total of nine independent equations. With nine independent equations and nine unknowns, this system of equations is solvable.

3.5 One-Dimensional Energy Equation

Each module of the simulation is modelled mathematically with the one-dimensional energy equation. For one-dimensional incompressible adiabatic flow in a control volume, the energy equation takes the following form:

$$\Sigma\left[Q_{in}(P_{in}+\frac{\alpha\rho}{2}{U_{in}}^2+\rho g z_{in})\right] = \Sigma\left[Q_{out}(P_{out}+\frac{\alpha\rho}{2}{U_{out}}^2+\rho g z_{out})\right]+losses \quad (3.1)$$

where Q is the volumetric flow rate, P is the static pressure of the fluid, α is a kinetic energy correction factor, ρ is the density, U is the mean velocity, g is gravity, and z is elevation.

The terms of the energy equation represent the three main components of the fluid energy flux, and have dimensions of work per unit time. QP is the pressure energy of the flow, $Q\frac{\alpha\rho}{2}U^2$ is the kinetic energy of the fluid, and $Q\rho gz$ is the gravitational potential energy. The development and application of the energy equation is covered in detail in many introductory fluid mechanics text books, such as White (1986).

Most modules have only one inlet and one outlet flow, so the flow rates can be eliminated and Equation 3.1 simplifies to the following form:

$$P_{in} + \frac{\alpha\rho}{2}{U_{in}}^2 + \rho g z_{in} = P_{out} + \frac{\alpha\rho}{2}{U_{out}}^2 + \rho g z_{out} + losses \qquad (3.2)$$

Module three, the mixing region, has two inlet flows, the primary and secondary, and one outlet flow, the tertiary. This module uses the following equation:

$$Q_1(P_2 + \frac{\alpha\rho}{2}{U_2}^2 + \rho g z_2) + Q_2(P_2 + \frac{\alpha\rho}{2}{U_2}^2 + \rho g z_2) = Q_3(P_3 + \frac{\alpha\rho}{2}{U_3}^2 + \rho g z_3) + losses \qquad (3.3)$$

All the energy equations use elevation data for the experimental apparatus, obtained as described in Section 2.4.3. Development of the loss terms is described in Section 3.7.

3.6 Continuity Equation

In addition to conservation of energy, node two requires the use of the continuity equation for mass flow. Assuming the water density to be constant throughout the model, this equation is as follows:

$$Q_3 = Q_1 + Q_2 \qquad (3.4)$$

3.7 Energy Loss Terms

To accurately predict pressures and flow rates using conservation of energy, all energy flows into and out of the control volume must be accounted for. The one-dimensional energy equation contains terms for the pressure, kinetic, and gravitational potential energy of the flow, but energy losses arising from the three-dimensional nature of real pipe flows cannot be directly calculated. To allow the use of simple one-dimensional models, loss terms are used to account for these energy losses. Loss terms have been developed for many conditions encountered in pipe flow, and the use of these terms is expanded to allow their use in the more complex configuration of an annular mixing jet pump.

In the mixing region of a jet pump, energy losses come from three main sources: expansion of the jet flow into the mixing region, mixing losses, and viscous friction on the pipe walls. In the flows leading to and from the mixing region, losses arise from pipe wall friction and from flow area and direction changes.

For the general one-dimensional energy equation (Equation 3.1), the losses are modeled as follows:

$$loss\ term = Q\frac{\rho}{2}U^2K_{loss} \tag{3.5}$$

As with the energy equation, $Q\frac{\rho}{2}U^2$ represents the kinetic energy of the fluid, and K_{loss} is a coefficient representing the fraction of the kinetic energy lost to viscous dissipation.

For the case of a flow with only one inlet and outlet (Equation 3.2), the flow rate factor is removed, and the loss term takes the following form:

$$loss\ term = \frac{\rho}{2} U^2 K_{loss} \tag{3.6}$$

The loss terms are determined experimentally for specific flow patterns. Factors have been determined for losses occurring in many common engineering applications, such as pipe wall friction, sudden and gradual flow expansions and contractions, pipe fittings, and valves. These factors and their implementation in the simulation are further discussed below.

3.7.1 Pipe Wall Friction

Pipe wall friction is the result of two flow conditions: the viscosity of the fluid, and the non-slip condition at the fluid-wall interface. These combine to produce a shear layer in the fluid as the pipe wall is approached, and the retarding shear stress acting over the pipe surface results in an energy loss from the fluid.

Pipe wall friction losses are modelled with the following loss term:

$$K_f = f \frac{L}{D} \tag{3.7}$$

where f is the friction factor for the pipe, and L and D are the length and diameter of the pipe.

For laminar flows, the friction factor is is a function solely of the Reynolds number based on pipe diameter, and is given by the following equation (White, 1986):

$$f_l = \frac{64}{Re_D} \tag{3.8}$$

For transition and turbulent flows, the value of f is obtained from the Colebrook equation (Colebrook, 1939), or its graphical version, the Moody chart (Moody, 1944).

Although the Colebrook equation is commonly used and reasonably accurate, it is a nonlinear, implicit equation which requires an iterative numerical solver. Such a solver adds programming complexity and additional processing time, so an explicit function developed by Haaland (1983) was used to calculate the friction factors for the simulation:

$$\frac{1}{\sqrt{f_t}} = -1.8 \log \left[\frac{6.9}{Re_D} + \left(\frac{\epsilon/D}{3.7} \right)^{1.11} \right] \tag{3.9}$$

With the Haaland function, the friction factor is explicitly calculated using the flow Reynolds number based on pipe diameter Re_D, the surface roughness ϵ, and the pipe diameter D. The Haaland function deviates less than $\pm 1.5\%$ from the Colebrook equation, and since the Colebrook equation itself is only accurate to within about $\pm 5\%$ for smooth pipes and $\pm 10\%$ for rough pipes (Moody, 1944), the Haaland function is considered sufficiently accurate for the simulation.

With two exceptions, wall friction losses were calculated for all simulation modules where wall friction applied. The flow from nodes 7 to 8 in Figure 3.1 was the only part of the simulation not constrained by walls, so no friction losses were applied there. Friction losses were not considered for the inlet and discharge plena, since the plena were very short, the flows would be undeveloped, and wall friction losses would be very small compared with the large flow inlet and outlet losses.

3.7.2 Flow Direction Changes (Elbows)

In pipe flows, changes in flow direction may be made with curved pipes or elbow fittings. A flow direction change introduces secondary flows which effectively increase the distance the fluid must flow, and the dissipation of which result in energy losses. Elbow losses are denoted with the symbol K_{el}.

The simulation contains three elbows. Two of these are the 32 mm and 51 mm 90° elbows installed in the discharge piping between nodes 5 and 6 in Figure 3.1. The third "elbow" is the 90° flow bend in the jet pump inlet. This bend was modeled as a pipe elbow with a diameter equal to the mean of the effective hydraulic diameters at the jet pump inlet (nodes eight) and the throat (node two).

Since most engineering applications involve turbulent flow, data for turbulent loss coefficients are readily available. However, despite decades of research, the literature remains inconsistent. For example, The Crane Company (1976) and The Hydraulic Institute (1954) present loss coefficients

which vary with the nominal size of the fitting, although these sources differ widely on the magnitude of the coefficient. Blevins (1992) summarizes data suggesting that, provided the Reynolds number exceeds 2×10^5, the loss coefficient is constant, and that for $Re < 2 \times 10^5$, K_{el} varies with $Re^{-0.2}$. Table 3.1 summarizes the loss coefficients for three sizes of 90° elbows in fully turbulent flow; it is clear by inspection that there is wide disagreement regarding the correct value of the loss coefficient.

Table 3.1: Loss coefficients for 90° elbows in turbulent flow ($Re \geqslant 2 \times 10^5$).

Data Source	Nominal Elbow Size		
	13 mm	25 mm	51 mm
The Crane Company (1976)	0.81	0.69	0.57
The Hydraulic Institute (1954)	2.1	1.5	0.98
Blevins (1992)	1.1	1.1	1.1

The apparent disagreement of these sources would be of great concern if the elbow losses were significant. Fortunately, the elbows represent only a small fraction of the total losses in the jet pump model, and a method is readily available to assess the validity of these different loss models.

The simulation was tested with each of the three elbow loss models, and the calculated results were compared with the experimental data. A MATLAB® program was written to compare the flow rates predicted by the simulation with the experimental data. These values were then used to calculate the simulation error. For each inlet pressure setting, the mean and standard deviation of the simulation error was also calculated.

Although all three models gave very similar results for standard deviation of the mean error values, the Crane model gave the smallest mean error for all three flow rates. It will also be shown in Chapter 4 that even 50% variations in the value of the elbow loss coefficient have negligible effects on the uncertainty of the results. It was however found that the simulation converged to a solution much faster with the Crane model than with the other two models. For the reasons of small error and quicker calculation time, the Crane model was used for all elbow loss calculations.

3.7.3 Gradual Area Changes

Gradual area changes occur when the cross-sectional area of the flow changes slowly enough that large recirculation vortices, and the corresponding large losses, do not develop at the area transitions. Loss coefficients for gradual area changes are denoted K_{gc} for gradual contractions and K_{ge} for gradual expansions. Functions for these coefficients are commonly found in textbooks on fluid mechanics.

The only gradual contraction occurs in the inlet to the jet pump. To allow calculation of K_{gc} for different jet pump designs, the following function was fit to data given by White (1986) using a least-squares method:

$$K_{gc} = 1.23 \times 10^{-7}(2\theta)^3 + 5.56 \times 10^{-6}(2\theta)^2 + 3.89 \times 10^{-4}(2\theta) \qquad (3.10)$$

where 2θ is the included angle of the gradual contraction in degrees. This function is valid in the range $0° \leqslant 2\theta \leqslant 60°$.

The calculation of 2θ for the jet pump inlet was done by geometric construction of a frustum which represented the inlet duct. The base of the frustum had a diameter equal to the effective hydraulic diameter of the jet pump inlet (node 8 in Figure 3.1), while the top of the frustum used the effective diameter of the throat (node 2). The height of the frustum was the arc length of the inlet flow path between nodes 8 and 2. The included angle of the frustum was calculated and used for 2θ in Equation 3.10.

There are no gradual expansions in the jet pump model. However, one gradual expansion exists in the piping between nodes 5 and 6 where the discharge pipe diameter increases from 32 mm to 51 mm. This expansion was made with a pipe fitting with an included angle $2\theta = 90°$. To simplify the program code, a single number $K_{ge} = 0.9$ was used, based on data given by White (1986).

3.7.4 Sudden Area Changes

Sudden area changes occur when the cross-sectional area of the flow makes an abrupt change. At the corner of the transition point, a recirculation bubble forms, and this bubble generates the losses at the transition. A sudden contraction has a second recirculation region just downstream of the inlet to the smaller pipe, resulting in additional losses. Loss coefficients are denoted K_{se} for sudden expansions and K_{sc} for sudden contractions. Functions for these coefficients, based on the relative diameters of the pipes flowing into and out of the sudden expansion or contraction, are commonly found in fluid mechanics textbooks.

Two special cases of sudden area changes are the transition from an infinite tank to a pipe, or vice versa. In these cases, one of the "pipes" has an infinite diameter, and the function defining the loss coefficient collapses to a constant.

The losses at a sudden contraction can be reduced by rounding the inlet edge of the smaller pipe. This reduces or eliminates the recirculation region at the inlet of the smaller pipe, reducing the total loss at the transition. The amount of reduction depends on the ratio of the inlet edge radius r_i to the diameter of the smaller pipe D_{out}. The loss decreases as the ratio r_i/D_{out} increases, until a limit is reached, after which any further increase in the ratio has no effect on the loss coefficient.

To calculate a sudden expansion or contraction loss coefficient, the nominal coefficient is first calculated using the appropriate function shown in Table 3.2. If the area change is a sudden contraction with a rounded inlet edge, the nominal coefficient is then multiplied by the appropriate rounded inlet correction factor, given in Table 3.3.

The simulation contained one sudden expansion, located at point 4a in Figure 3.1. This was modeled as the expansion from the effective diameter of the annulus to the effective diameter of the discharge plenum.

There were two sudden contractions in the simulation. The first occurred at node 1, where the flow area made a sudden transition from the jet inlet plenum to the much smaller jet nozzles. The jet nozzles had slightly rounded inlet edges, so the rounded inlet correction factor for pipe flow was applied.

Table 3.2: Loss coefficients for sudden expansions and contractions (Blevins, 1992).

Flow Condition	Sharp-Inlet Loss Coefficient
Inlet from Infinite Tank	$K_{sc} = 0.50$
Sudden Contraction	$K_{sc} = \frac{1}{2}\left[1 - \left(\frac{D_{out}}{D_{in}}\right)^2\right]$
Sudden Expansion	$K_{se} = \left[1 - \left(\frac{D_{in}}{D_{out}}\right)^2\right]^2$
Discharge to Infinite Tank	$K_{se} = 1.0$

The second sudden contraction occurs at the jet pump inlet between nodes 7 and 8. This was considered an inlet from an infinite tank, and used the appropriate rounded inlet correction factor.

3.7.5 Jet Mixing Losses

The mixing region of the jet pump is somewhat analogous to a sudden enlargement, where the jet expands to the larger throat diameter. Compared with a sudden expansion, the co-flowing secondary flow reduces the recirculation at the jet exit, but allows the formation of a shear layer between the jet and secondary flow. This shear layer allows momentum transfer from the jet to the secondary flow and drives the entire operation of the jet pump, but this layer does not transfer momentum very efficiently and introduces significant losses to the overall system.

Table 3.3: Rounded inlet correction factors to K_{sc}.

Inlet from an infinite tank: (White, 1986)	
$k_{edge} = -160(\frac{r}{D})^3 + 80.9(\frac{r}{D})^2 + 14.3(\frac{r}{D}) + 1.00$	if $\frac{r}{D} < 0.2$
$k_{edge} = 0.1$	if $\frac{r}{D} \geqslant 0.2$
Sudden contraction in pipe flow: (Bullen et al., 1988)	
$k_{edge} = -187(\frac{r}{D})^3 + 82.0(\frac{r}{D})^2 + 14.9(\frac{r}{D}) + 1.00$	if $\frac{r}{D} < 0.15$
$k_{edge} = 0.2$	if $\frac{r}{D} \geqslant 0.15$

Cunningham (1957) presented a function for the energy losses caused by the mixing in a jet pump, which can be rewritten in the following form for use as a loss coefficient:

$$K_{mix} = \left[1 - 2R(1+M) + R^2(1+M)^3 + \frac{M^3R^2}{(1-R)^2} - 2M^2R^2\frac{1+M}{1-R}\right] \tag{3.11}$$

Equation 3.11 was used in the simulation to estimate the mixing losses. It may be noted that for the case where there is no secondary flow, the flow ratio M equals zero, and the equation reduces to the expression shown in Table 3.2 for a sudden expansion from the jet diameter to the throat diameter.

3.7.6 Non-Circular Shapes and Effective Diameter

All of the previous discussion on loss factors has been for flows in pipes or ducts of circular cross-section. To allow the use of the loss factor models in ducts of non-circular cross-section, the concepts of hydraulic diameter and effective diameter are used.

The hydraulic diameter of a pipe of arbitrary cross-sectional shape is calculated with the following equation:

$$D_{hyd} = \frac{4A_{pipe}}{\mathcal{P}_{pipe}} \tag{3.12}$$

where A_{pipe} is the cross-sectional area of the flow in the pipe, and $\mathcal{P}_{pipe}$ is the wetted perimeter of the pipe wall over which the wall shear stress acts. For a circular pipe, the hydraulic diameter equals the pipe diameter.

The hydraulic diameter alone tends to under-estimate the friction of a pipe flow, particularly for the case of laminar flow, where the error can easily approach forty percent. For laminar flows, most duct shapes can be solved exactly, and a method based on the laminar analysis has been developed which significantly improves the accuracy of friction factor calculations for turbulent flows (Jones, Jr., 1976).

The Jones method compares the laminar flow friction factor for a non-

circular pipe to the friction factor for a circular pipe:

$$\text{for a circular pipe, } f_l = \frac{64}{Re}$$
$$\text{for a non-circular pipe, } f_l = \frac{k}{Re}$$

where k is the dimensionless friction coefficient determined from the exact solution of the laminar flow problem for a specific duct profile. For a duct with an arbitrary cross section, this coefficient generally falls within the range $48 \leqslant k \leqslant 96$ (Blevins, 1992).

For turbulent flows, a shape factor ϕ^* may be calculated:

$$\phi^* = \frac{64}{k} \tag{3.13}$$

This shape factor applies to geometrically similar pipes, and is used to calculate an effective diameter for the pipe:

$$D_{eff} = \phi^* D_{hyd} \tag{3.14}$$

The effective diameter is used as the characteristic diameter for all loss coefficient calculations. Flow velocities are calculated with the actual cross-sectional area of the duct. For example, to determine a pipe wall friction factor, the Reynolds number, relative roughness, and friction factor would

be calculated using D_{eff} as follows:

$$Re_{D_{eff}} = \frac{UD_{eff}}{\nu}$$

$$\text{relative roughness} = \frac{\epsilon}{D_{eff}}$$

$$k_f = \frac{fL}{D_{eff}}$$

It was reported by Jones, Jr. (1976) that this method gives turbulent smooth-pipe friction factors which are accurate to within ±5% of experiment.

Functions for ϕ^* for rectangular ducts are presented by Jones, Jr. (1976), and for concentric annuli by Jones, Jr. and Leung (1981). For a sector of an annulus, such as the half-annulus used for the experimental model, functions published by Sparrow et al. (1964) allow calculation of ϕ^*.

For the simulation, non-circular ducts are found in the mixing chamber and annulus, the jet pump inlet, and the inlet and discharge plena.

The half-annulus of the jet pump was modelled with the shape factor for a sector of an annulus, which for the model geometry and dimensions gave $\phi^* = 0.753$. It should be noted that this was very close to the value of $\phi^* = 0.752$ obtained for a rectangular duct with a width equal to the arc length of the midpoint of the annulus radii, and with a height equal to the gap between the radii.

Since it was found that the values of ϕ^* for the annulus calculated with the annular sector and rectangular models were very close, the jet pump inlet was treated as a rectangular duct. Using a width equal to the arc length of

the inlet surface and a height equal to the inlet gap, a shape factor $\phi^* = 0.735$ was calculated.

A semi-circular duct, found in the inlet and discharge plena, has a shape factor $\phi^* = 1.01$ (Blevins, 1992). Since this is very close to unity, the shape factor was not applied, and the hydraulic diameter alone was used for the inlet and discharge plena.

3.7.7 Combined Effects

The simultaneous combined effects of several types of losses were accounted for by linear superposition. The multiple loss terms were individually calculated, then added together to give the overall combined energy loss for the module.

3.8 Construction and Solution of the Model

As shown in Section 3.4, the flow diagram yields a system of nine simultaneous nonlinear equations. These equations were solved using the Newton-Raphson method, described in Jaluria (1988).

A group of programs was written with the MATLAB® programming language to construct and solve the system of equations. The main program is a function which receives parameters from a calling program, builds the solution matrices, and performs the necessary iterations until a solution converges. The function then returns the results to the calling program.

The CGS system of consistent units was used for all programs. Early work on the simulation programs showed that use of the MKS system of units resulted in matrices with unacceptably high condition numbers, which caused some problems with solution stability and convergence. Adopting the CGS system reduced the condition number from the order of 10^{15} to 10^{7}. The use of CGS units did not affect the numerical results compared with MKS units. However, the lower condition number resulting from the use of CGS units allowed rapid, reliable convergence for all simulation runs.

The program inputs included the known inlet plenum pressure P_0, the water level and temperature, the measured flow rates Q_1 and Q_3, the number of jets, and the jet diameters. The water level was used to calculate the hydrostatic pressures P_6 and P_7. The water temperature was used to calculate the water density and viscosity. The secondary flow Q_2 was calculated as the difference between Q_1 and Q_3. All model dimensions were coded into the program.

The actual flow rates measured during the experiments were used as initial guess values for the flow rates. The calculated hydrostatic pressure P_7 was used as the initial guess value for pressures P_1 to P_5.

The Newton-Raphson method uses an iterative method to solve the system of equations. The solution progresses until some convergence criterion is met, such as a maximum residual or maximum percent change in the calculated solution. For this simulation, convergence was considered to occur if a calculated solution differed from the solution of the previous iteration by less

than 10^{-10} percent. This criterion gave convergence in about fifteen iterations and gave function residuals of the range of 10^{-6} to 10^{-13}, corresponding to a maximum numerical error of the order of 10^{-4} percent.

3.9 Validation of the Model

The simulation was subjected to several types of checks to ensure the validity of its results. The validation process used both unit and integration testing as described by Rakitin (1997).

3.9.1 Unit Testing

Unit testing is the process of locating and correcting faults in the individual functions or modules of a main program. This type of testing was performed on the eight modules of the simulation program, as well as for the functions which were called to evaluate the loss coefficients during the program execution.

Several specific activities were done to ensure the modules functioned properly. First, the code was reviewed to ensure the algorithms were correct, and that the proper coding syntax was used. To aid this process, consistent variable naming was used. Tests were done of all the loss coefficient functions to ensure that they returned correct values. This was done by comparing the function results with published data.

Some global data structures were used to minimize repeated variable initialization; these global data were stored as MATLAB® data files, which

were loaded by subsequent analysis programs. This ensured consistency of the input data for all analyses.

Since the simulation was very application-specific, general purpose error traps were not widely used and run-time error handling was limited. The elbow loss coefficient function was written to accept only specific values of elbow angle, and to issue a warning if the input angle was not acceptable. The main simulation program also included a trap for non-convergence, which terminated the program if convergence did not occur within 2000 iterations.

Tests were done at the boundaries of the experimental envelope, and at all points the program converged onto realistic solutions. Additional simulation runs were done within the experimental envelope to search for numerical singularities, and none were found.

3.9.2 Integration Testing

Integration testing searches for problems with the interfaces or interactions between program modules. This was done in a bottom-up manner, first by testing the simulation modules and functions, then by testing the interfaces between these units.

Apart from the iterative solver used for the Newton-Raphson method, the simulation is a single pass program. This simplified the task of analyzing the potential flow paths. Many of the loss coefficient functions accepted multiple input parameters, and had multiple flow paths before a result is calculated. For these programs, each path was tested to ensure a correct path and result.

Many of the other issues commonly checked during integration testing, such as resource allocation, are handled automatically by MATLAB® , and were not tested.

The final integration test was a check of the energy flows through the simulation. For each module, the total energy flux at the inlet and outlet was calculated using Equation 3.1. The total losses within each module were also calculated, using Equation 3.5. If the simulation works properly, the inlet energy should equal the outlet energy plus the losses. This test uncovered a small problem with one of the modules, and the final simulation program gave good results with this test.

3.9.3 Final Validation Comments

Finally, some other comments should be made regarding the simulation and its validation. First, it should be noted that, like most software, the simulation did not always work well, or even at all, and that some of its features are legacies from early development work. One such feature was the use of CGS units of measure, which was an attempt to reduce the condition number of the solution matrices. Now, after substantial development, the simulation appears stable. For all the conditions tested, it converges, and converges rapidly to a unique, realistic solution. Secondly, and just as importantly, the simulation achieves reasonable results without any adjustment "knobs" or experimentally-derived factors. It is believed that the validation process, the reasonable results, and the absence of adjustment factors all suggest that the simulation program gives valid results.

Despite the apparent validity of the simulation results, the uncertainty of these results is in many cases quite high. This will be discussed in the following chapter. The absolute accuracy of the simulation, as compared with the experiments, will be discussed in Chapter 5.

CHAPTER 4

MEASUREMENT AND SIMULATION ACCURACY

4.1 Introduction

Before a meaningful analysis and discussion of the results may be undertaken, it is first necessary to estimate the uncertainties or potential errors of the results. This chapter describes a method of estimating the uncertainty of measurements presented by Taylor and Kuyatt (1994), then discusses the application of this method to the experimental measurements and the simulation results.

4.2 Combination and Propagation of Errors

A measurand or output quantity Y is often not measured directly; rather, it is determined from other measurements through a functional relationship:

$$Y = f(X_1, X_2, X_3, \ldots, X_N) \tag{4.1}$$

An estimate of the measurand may be obtained using estimates of the input variables as follows:

$$y = f(x_1, x_2, x_3, \ldots, x_N) \tag{4.2}$$

where y is the estimate of Y, and $x_1, x_2, x_3, \ldots, x_N$ are estimates of the input variables $X_1, X_2, X_3, \ldots, X_N$.

The combined standard uncertainty of y is denoted $u_c(y)$. This is the estimated standard deviation of y, and is given by the following equation:

$$u_c{}^2(y) = \sum_{i=1}^{N} \left[\frac{\partial f}{\partial x_i}\right]^2 u^2(x_i) + 2\sum_{i=1}^{N-1}\sum_{j=i+1}^{N} \frac{\partial f}{\partial x_i}\frac{\partial f}{\partial x_j} u(x_i, x_j) \tag{4.3}$$

where $u(x_i)$ is the standard uncertainty of measurement x_i, and $u(x_i, x_j)$ is the covariance associated with x_i and x_j.

For the case where the covariance between measurements is zero, the second term of Equation 4.3 reduces to zero, and the equation for the combined standard uncertainty simplifies as follows:

$$u_c{}^2(y) = \sum_{i=1}^{N} \left[\frac{\partial f}{\partial x_i}\right]^2 u^2(x_i) \tag{4.4}$$

The expanded uncertainty U_p is calculated by applying a coverage factor k_p to the combined uncertainty:

$$U_p = k_p u_c \tag{4.5}$$

The coverage factor provides an estimate of the overall uncertainty, which by NIST and international practice is generally at the 95% confidence level. Using large data samples and assuming a normal distribution, the 95% confidence level is is achieved with a coverage factor $k_p = 2.0$. However, for small sample sizes, the normal distribution is not appropriate, and the Student's t distribution is used instead.

To determine k_p from the t distribution, the number of statistical degrees of freedom for the measurement is required. For a single measurement, this is the number of measurements less the number of reduced data calculated from these measurements. For multiple measurements with zero covariance, the effective number of degrees of freedom for the combination is calculated as follows:

$$\nu_{eff} = \frac{u_c^4(y)}{\sum_{i=1}^{N} \frac{\left(\frac{\partial f}{\partial x_i}\right)^4 u^4(x_i)}{\nu_i}} \tag{4.6}$$

where ν_i is the number of degrees of freedom for measurement i. For the analyses presented here, the t distribution was used whenever $\nu_i \leqslant 27$, since with more degrees of freedom, the t distribution gives $k_p = 2.0$ (Miller and Freund, 1985).

Finally, an estimate of the true process value to the specified confidence

level may be calculated:

$$Y = y \pm U_p \tag{4.7}$$

There are two methods of estimating the standard uncertainty of the measurements. In a Type A analysis, the standard uncertainty is calculated by a statistical analysis of measurement data. In a Type B analysis, non-statistical methods are used and the standard uncertainty is estimated based on the judgement and experience of the analyst.

For this chapter, the experimental measurements were analyzed with both Type A and Type B methods, and a Type B analysis alone was performed on the simulation. It was also assumed that the covariance was zero and that Equation 4.4 applied. The following sections describe each analysis in greater detail.

4.3 Accuracy of the Experimental Measurements

Several types of data were recorded during the experiments, including volumetric flow rates, water pressures, and water temperature and elevation. The following sections describe in greater detail the sources of uncertainty for these measurements, and present estimates of the overall uncertainty of these measurements.

4.3.1 Uncertainty of the Measured Flow Rates

The volumetric flow rates were measured using Annubar flow meters and Validyne pressure transducers, described in Section 2.4.1. The calibration produced expressions for the volumetric flow rate as a function of the differential pressure measured with the flow meter. The general form of these functions is as follows:

$$Q = BP^m \tag{4.8}$$

where the calibration constants B and m are determined from a least-squares curve fit to the linear version of the function:

$$\log Q = m \log P + B \tag{4.9}$$

Applying Equation 4.8 to Equation 4.4 gives the following expression for the relative uncertainty of the flow rates:

$$\left[\frac{u(Q)}{Q}\right]^2 = \left[m\frac{u(P)}{P}\right]^2 \tag{4.10}$$

For the Annubar system, the exponent $m \approx 0.5$, so from Equation 4.10 the relative uncertainty of the flow rate is about half the relative uncertainty of the differential pressure measurement.

The following sections describe the methods used to minimize and estimate the overall uncertainty of the differential pressure, and the estimated values of the uncertainty.

4.3.1.1 Uncertainty Reduction by Apparatus Design

The flow meters were installed to minimize instrument errors caused by the physical positioning and arrangement of the system components.

Firstly, the Annubar flow meters were installed as recommended by the manufacturer, using recommended lengths of straight pipe upstream and downstream of the meters to minimize the effects of elbows and other pipe fittings.

The meter measuring Q_3 was located approximately 30 cm above the tank water surface, and therefore operated at a slight vacuum. This could have allowed air bubbles to enter the pressure taps during test configuration changes, affecting the differential pressure measurements as described in Section 4.3.3.3. To prevent this from occurring, the Validyne sensor for this meter was placed approximately 100 cm below the meter and connected with transparent plastic tubing. Once filled with water, the elevation difference provided enough hydrostatic pressure to bleed all air bubbles from the pressure taps, eliminating a potential source of error.

The Annubar flow meter measuring Q_1 operated at the high pressure of the jet pump inlet, so the pressure tap lines could be easily bled of air. Furthermore, because of the high static pressure, the effects of air bubbles in the pressure tap tubing would be very small.

Finally, calibration of the flow metering systems was performed with the same piping, equipment, and instruments that were used for the experiments. This was done to minimize the introduction of unknown errors with changes

to any of the components, and also to simplify the data analysis, since the overall uncertainties in the system could be easily determined.

Some sources of uncertainty of the differential pressure measurements could not be designed out of the apparatus. Contributions to this uncertainty can be segregated into three groups: items which are detected and calculated from the system calibration data, instrument zero drift, and instrument range or span drift. Each of these three groups is discussed in greater detail in the following paragraphs.

4.3.1.2 Statistical Analysis of Calibration Data

The measured flows Q_1 and Q_3 were turbulent, with Reynolds numbers ranging from about 8 000 to 33 000. Because of the turbulence, large pressure fluctuations were detected at the Annubar pressure taps. The averaging volt meter (AVM) was used to determine a time average of the pressure fluctuations, but variations in the averaged values were still observed. These variations, however, allowed statistical analysis of the data to determine the standard error of the flow measurements.

The calibration data were fit to Equation 4.9 to obtain the calibration function coefficients. The standard error of estimate was calculated for the fitted curve, and was used as the standard error in Equation 4.4; Table 4.1 summarizes the standard error for both of the measured flow rates.

Analysis of the calibration data accounts for uncertainties arising from the pressure fluctuations at the Annubar flow meters, as well as nonlinearities

Table 4.1: The standard error of flow rates Q_1 and Q_3 measurable by metering system calibration at the 95% confidence level.

Flow Rate	Standard Error
Q_1	0.24%
Q_3	0.45%

in the Validyne and AVM instruments. However, calibration drift for these instruments cannot be estimated with this analysis, so the drift must be estimated and added separately.

4.3.1.3 Instrument Scale Drift

The electronic circuits in the Validyne and AVM instruments are subject to a small amount of drift in their calibration over time, which is usually caused by effects of temperature, humidity, and aging of the circuit components. To minimize thermal changes during the experiments, the instruments remained turned on for the duration of the tests, but it is likely that some drift occurred during the course of the experiments.

The maximum relative uncertainty of the Validyne output due to drift is specified by the manufacturer to be ± 0.25% (Validyne Corp., 1971). Data for the AVM were not available, but based on information for the voltage to frequency converter and the power supply, the maximum relative uncertainty of the AVM output due to drift is estimated at ± 0.2%. Assuming the uncertainty to be uniformly distributed across the range, the standard error is estimated by dividing the uncertainty by root three; this type of estimate for standard error is taken to have an infinite number of degrees of freedom.

4.3.1.4 Instrument Zero Drift

Another potential source of error was from zero drift in the Validyne and AVM instruments. This error was minimized by recording the AVM output at zero flow rates, and using this value as a correction term during data analysis. Because of this correction, it was assumed that this source of uncertainty was insignificant compared with the other sources, and was not included in the calculation of the combined uncertainty.

4.3.1.5 Expanded Uncertainty of the Flow Rate Measurements

The combined uncertainty of the volumetric flow rates Q_1 and Q_3 is the root sum square of the calibration and drift uncertainties. Since Q_2 was calculated as the difference between Q_1 and Q_3, the uncertainty of Q_2 is the root sum square of the uncertainties for Q_1 and Q_3. The expanded uncertainty is calculated by applying an appropriate coverage factor.

The calibration for Q_1 was made with 45 data points. Subtraction of the two calculated curve fit parameters leaves 43 degrees of freedom. When this is combined with the Validyne and AVM drift, both of which are assumed to have infinite degrees of freedom, the number of effective degrees of freedom becomes 57. This is enough for the normal distribution to apply, and a value of $k_p = 2.00$ was applied to $u_c(Q_1)$.

The calibration for Q_3 was made with only eight data points, giving six degrees of freedom. When combined with the instrument drift, there are a total of seven effective degrees of freedom. The t statistic corresponding to

the 95% level of confidence at seven degrees of freedom is 2.36, and this was used as the value for k_p applied to $u_c(Q_3)$.

The calculation for Q_2 used both Q_1 and Q_3, making a total of 12 effective degrees of freedom for the combination. The t statistic corresponding to the 95% confidence level at 12 degrees of freedom is 2.18, and this was used as the value for k_p applied to $u_c(Q_2)$.

Table 4.2 summarizes the combined uncertainties, coverage factors, and expanded uncertainties of all three measured flow rates.

Table 4.2: The combined uncertainties, coverage factors, and expanded uncertainties of the measured volumetric flow rates Q_1, Q_2, and Q_3 at the 95% confidence level.

Flow Rate	Combined Uncertainty	Coverage Factor	Expanded Uncertainty
Q_1	0.257%	2.00	0.51%
Q_2	0.531%	2.18	1.2%
Q_3	0.465%	2.36	1.1%

4.3.2 Uncertainty of the Measured Jet Inlet Pressure

The jet inlet plenum pressure was measured with a Bourdon tube pressure gauge. This gauge was calibrated with a Budenberg model 280L deadweight pressure calibrator in the range from zero to 690 kPa (0-100 psi), and was found to indicate within ± 0.3 psi (± 6.9 kPa) of the calibration standard over the entire range. However, the resolution of the gauge is ± 0.5 psi (± 3.5 kPa), which sets the lower limit for the uncertainty of the gauge.

Dividing by root three, the standard error for the instrument is taken as $u(P_0) = \pm$ 2.0 kPa.

4.3.3 Uncertainty of the Measured Mixing Region Pressures

Static pressure measurements were made along the mixing length of the jet pump annulus. The pressures were measured with a Validyne system, and fluctuations in the measured pressure were smoothed with the AVM. Since these system components have linear additive uncertainties, the overall uncertainty of the measurements is the root sum square of the component uncertainties.

4.3.3.1 Uncertainty Reduction by Apparatus Design

As with the flow metering system, achieving accurate pressure measurements starts with good design of the measurement system.

The static pressure measurement system included several design features to minimize the introduction of errors and uncertainties. The pressure tap holes were made small in comparison to the effective diameter of the annulus, were drilled perpendicular to the annulus wall, and were deburred before the experimental model was assembled.

Each of the 17 pressure taps was connected with transparent plastic tubing to a valve, then from the valve through a manifold to a single pressure transducer. The tubing allowed confirmation that large air bubbles were removed from the system, and the use of a single pressure sensor eliminated differences between sensors as an additional uncertainty of the measurements.

Even with good equipment design, error in the static pressure measurements may still have been introduced from three sources: instrument nonlinearity, instrument drift, and air bubbles in the pressure tap tubing. These sources are discussed in the following sections.

4.3.3.2 Instrument Uncertainties

The uncertainties in the Validyne and AVM instruments arise from nonlinearities and drift in the instruments. Data for the Validyne system were obtained from Validyne Corp. (1971), and similar data for the AVM were estimated from data sheets for the AVM voltage to frequency converter and power supply components. Zero drift errors were eliminated by recording the system zeros prior to data collection. Table 4.3 summarizes the uncertainties for both instruments. Assuming the uncertainty to be a uniform distribution across the range, the standard error is estimated by dividing the uncertainty by root three.

Table 4.3: The overall relative uncertainties of the static water pressure instruments.

Instrument	Nonlinearity	Scale Drift
Validyne	0.1%	0.25%
AVM	0.25%	0.2%

4.3.3.3 Air Bubbles in the Pressure Tap Tubing

Great care was taken to ensure that large air bubbles were removed from the pressure tap tubing before measurements were made. This was accomplished by operating the apparatus, opening the Validyne bleed port, then opening each pressure tap selector valve. This allowed water to flow through the pressure tap tubing, flushing out all large air bubbles.

In a vertical tube, the presence of air bubbles which block the entire tube would reduce the sensed pressure, because the low mass density of air compared with water would reduce the hydrostatic pressure at the pressure sensor. For any tube orientation, the presence of large bubbles would also cause surface tension stresses between the water and the tubing, which when combined with the compressibility of the air, could introduce some hysteresis to the pressure measurements. These factors would be more significant when measuring low pressures, such as those found in the mixing region, and would be of little importance if the measured pressures were much higher, such as at the jet nozzle inlet plenum.

Small air bubbles were not considered to be a factor affecting the accuracy of the pressure measurements. Small bubbles commonly formed inside the pressure taps as dissolved air left solution to coalesce on the inner walls of the pressure tap tubing. These bubbles were too small to completely block the tubing, and as a continuous column of water existed inside the tube, and it was assumed that the small bubbles did not affect the pressure measurements.

4.3.3.4 Expanded Uncertainty of the Static Pressure Measurements

The combined uncertainty of the static water pressure measurements is the root sum square of the instrument standard errors, which has the value $u_c(P)/P = 0.24\%$. Since the variance was estimated from a uniform distribution, it was assumed to have infinite degrees of freedom. This gives a coverage factor $k_p = 2.0$, and an expanded uncertainty $U_p(P)/P = 0.48\%$.

4.3.4 Uncertainty of Other Measurements

Two other measurements were made during the experiments: the water temperature and water surface elevation. The water temperature was measured with a Fluke model 2175A digital thermometer with a specified accuracy of $\pm$ 0.9°C (Fluke Mfg. Co., 1977), which corresponds to a standard error of $u(T_w) = \pm 0.5$°C. The water elevation was measured with a steel ruler at an estimated uncertainty of $\pm$ 0.2 cm, giving a standard error $u(H_w) = \pm$ 0.12 cm. These instruments were not calibrated, and the contributions of these two measurements to the overall uncertainty of the experiment and simulation results was found to be negligible.

4.3.5 Uncertainty of the Reduced Data

There are several additional parameters which are calculated from the measured data to indicate the performance of the jet pump. These parameters include the flow ratio and efficiency.

The flow ratio M is the ratio of the secondary to primary flow rates:

$$M = \frac{Q_2}{Q_1} \tag{4.11}$$

Applying Equation 4.4 and the relative uncertainties of Q_1 and Q_2 to Equation 4.11 gives an estimate of $u_c(M)/M = 0.59\%$. The combination of Q_1 and Q_2 has 18 effective degrees of freedom, giving a coverage factor $k_p = 2.10$ and an expanded uncertainty for the flow ratio $U_p(M)/M = 1.2\%$.

The jet pump efficiency η is defined as the quotient of the flow energy leaving the pump to the energy entering the pump. The generally accepted expression for the efficiency, adjusted for the experiments and simulation as shown in Figure 3.1, is given as follows (Gosline and O'Brein, 1934):

$$\eta = \frac{Q_2\,(H_3 - H_7)}{Q_1\,(H_0 - H_3)} = MN \tag{4.12}$$

The combined uncertainty of the flow ratio was given above as 0.59%. A simple expression for the combined uncertainty of the head ratio N cannot be directly written, since it is dependent upon the actual flow rates and pressures. The uncertainty was therefore calculated for each test point and was found to fall in the range $0.62\% \leqslant u_c(N)/N \leqslant 1.2\%$, with a mean value of 0.86%. The uncertainties for M and N give a combined uncertainty range $0.85 \leqslant u_c(\eta)/\eta \leqslant 1.3\%$, with a mean value of 1.05%. Assuming a sufficiently large number of degrees of freedom, a coverage factor $k_p = 2.0$ can be applied to give a mean expanded uncertainty $U_p(\eta)/\eta = 2.1\%$.

4.4 Accuracy of the Simulation

In this section, the factors affecting the general accuracy of the simulation are discussed. There likely exist small dimensional differences between the experimental and computer models, and there are uncertainties associated with the models used to simulate the jet pump, all of which generate the uncertainty that the simulation does not exactly represent the experimental test point. In this section, these uncertainties are discussed and the overall uncertainty of the simulation is estimated.

The uncertainty of the simulation was analyzed in a manner similar to that described in Section 4.1, using Equation 4.4. Forty-four parameters were identified as having a potential effect on the simulation results. These can be broadly classed as variations in model dimensions, elevations, and loss coefficients. A complete list of the parameters and their uncertainty limits is given in Appendix A.

To evaluate the expanded uncertainty of the simulation for a test point, the simulation was run once to obtain a nominal result, then again at plus and minus one percent of the upper and lower uncertainty limits for each parameter. For each parameter, these three solutions were fitted to a least-squares linear curve to obtain the partial derivative of the result with respect to the parameter. The partial derivatives and standard errors for each parameter were combined using Equation 4.4 to obtain the combined uncertainty for the simulation at the test point, then a coverage factor $k_p = 2.0$ was applied

to obtain the expanded uncertainty. This procedure was repeated for each combination of test number and nozzle inlet pressure.

The relative uncertainty for a test point was obtained by dividing the expanded uncertainty by the nominal result. An estimate of the overall relative uncertainty of a simulation output was calculated as the arithmetic mean of the relative uncertainties for all test points and pressures. The maximum and minimum values were also recorded to give an indication of the range.

To obtain an overall estimate the relative contribution of each parameter to the simulation uncertainty, the means of the relative contributions of each parameter were calculated across all test points and pressures. These means did not necessarily sum to unity, so they were normalized by dividing by the sum of the means.

The uncertainty estimates were calculated for each of the three flow rates, the pressure P_4 which corresponds to pressure tap 17 of the experimental model, and the jet pump efficiency. In each of the following sections, the relative uncertainty estimates are discussed, as are the parameters contributing the most to the uncertainty of the results.

4.4.1 Uncertainty of the Simulated Flow Rates

The estimated uncertainty of the simulated flow rates is summarized in Table 4.4. Also listed in the table are the top five contributors to the overall uncertainty of each of the three flow rates.

Table 4.4: The relative expanded uncertainty of the flow rates calculated by the simulation, and the five largest contributors to the uncertainty expressed as a fraction of the total, at the 95% confidence level.

Relative Uncertainty $U_p(Q_1)/Q_1$		
mean: 4.4%	minimum: 3.6%	maximum: 5.3%

Top five contributors to the relative uncertainty of Q_1		
Symbol	Parameter Description	Fraction
r_j	jet nozzle inlet radius	61.2%
f_2	jet nozzle friction factor	16.9%
D_j	jet nozzle diameter	12.1%
$K_{sc,1}$	sudden contraction into the jet nozzles	3.9%
α	kinetic energy correction factor	3.6%
	Total:	97.7%

Relative Uncertainty $U_p(Q_2)/Q_2$		
mean: 35.9%	minimum: 33.2%	maximum: 40.6%

Top five contributors to the relative uncertainty of Q_2		
Symbol	Parameter Description	Fraction
K_{mix}	mixing loss factor	91.5%
f_3	annulus friction factor	2.2%
$K_{el,6a}$	31mm discharge pipe elbow loss factor	1.9%
α	kinetic energy correction factor	1.7%
r_j	jet nozzle inlet radius	1.2%
	Total:	98.5%

Relative Uncertainty $U_p(Q_3)/Q_3$		
mean: 25.3%	minimum: 20.3%	maximum: 31.7%

Top five contributors to the relative uncertainty of Q_3		
Symbol	Parameter Description	Fraction
K_{mix}	mixing loss factor	90.2%
r_j	jet nozzle inlet radius	2.4%
f_3	annulus friction factor	2.2%
$K_{el,6a}$	31mm discharge pipe elbow loss factor	1.8%
α	kinetic energy correction factor	1.4%
	Total:	98.1%

The relative uncertainty of Q_1 has a mean value of 4.4%. This flow has a very simple loss model, with only a sudden contraction and friction in the nozzle. The flow is driven by the difference between the inlet plenum pressure and the pressure at the jet pump throat. The inlet plenum pressure, supplied by the pumps, is very high compared with the throat pressure, which is slightly lower than the hydrostatic pressure at the jet pump inlet. Despite the potential for large uncertainties of the processes within the jet pump, the pressure difference between the inlet plenum and the jet pump throat remains mostly insensitive to these processes, and the relative uncertainty of Q_1 is small.

The largest factor contributing to the uncertainty of Q_1 is the radius at the inlet to the jet nozzles r_j, which contributes about 61% of the total uncertainty. The radius has a nominal value of 0.038 cm (0.015") with an uncertainty range of ± 0.025 cm (0.010"). With the six nozzle diameters, this gives a range of radius to diameter ratios $0.021 \leqslant r_j/D \leqslant 0.19$, which gives a sudden contraction loss coefficient range of $0.052 \leqslant K_{sc} \leqslant 0.36$. This is much more than the ± 15% uncertainty for the loss coefficient function, so it is not unexpected that the inlet radius contributes roughly fifteen times as much to the uncertainty of Q_1 as the loss coefficient itself.

The results for the secondary and tertiary flows are similar to each other. The relative uncertainty of Q_2 has a mean value of 36%, which is an order of magnitude greater than the uncertainty of Q_1. The mean value of the relative uncertainty of Q_3 is 25%, which is approximately six times than the uncertainty of Q_1 and about two-thirds the uncertainty of Q_2.

Compared with the primary flow, the other two flows have much more complicated models, since they are dependent upon nearly all the processes occurring within the jet pump. However, it is clear from Table 4.4 that the uncertainties of both flows are almost completely the result of the uncertainty of the jet pump mixing model.

The only energy source for the jet pump is the primary flow, supplied by external pumps. Some of the flow energy is transferred to the ambient fluid in the mixing chamber, generating the secondary flow. The mixing process is simulated with the model described in Section 3.7.5.

The secondary flow gets all its energy from the momentum transfer from the primary to the secondary flows, and is therefore very sensitive to changes in the mixing model. This flow is also affected to a much smaller degree by the pressure difference between the jet pump inlet and the mixing chamber, which is seen by the effects of the other factors affecting the uncertainty.

The tertiary flow is supplied by both the primary and secondary flows, so the accuracy of the calculation is less dependent on the mixing process. This is seen by the lower mean value of the relative uncertainty of Q_3 compared with Q_2, which is entirely dependent on the mixing process for its flow. Also, the jet inlet radius r_j has a greater effect on Q_3 than Q_2. It was shown earlier that r_j has a very strong effect on Q_1, and this effect is carried into the tertiary flow more strongly than into the secondary flow.

4.4.2 Uncertainty of the Simulated Static Pressures

The uncertainty of the simulated static pressures was estimated by analyzing pressure P_4. This location was selected because it corresponds directly to pressure tap 17 of the experimental model, and therefore the simulated P_4 could be compared directly with experimental measurements. Table 4.5 summarizes the relative uncertainty of this pressure; also listed in the table are the top five contributors to the overall uncertainty of the static pressure.

Table 4.5: The relative expanded uncertainty of the annulus static discharge pressure P_4 as calculated by the simulation, and the five largest contributors to the uncertainty expressed as a fraction of the total, at the 95% confidence level.

Relative Uncertainty $U_p(P_4)/P_4$		
mean: 43.9%	minimum: 36.3%	maximum: 53.3%

Top five contributors to the relative uncertainty		
Symbol	Parameter Description	Fraction
K_{mix}	mixing loss factor	89.1%
$K_{el,6a}$	31mm discharge pipe elbow loss factor	2.9%
r_j	jet nozzle inlet radius	2.4%
f_3	annulus friction factor	1.9%
α	kinetic energy correction factor	1.2%
	Total of the top five contributors:	97.6%

The uncertainty of the static pressure P_4 has a mean value of 44%, which is about twice the uncertainty of the flow rate Q_3 which flows past that point. Review of the numerical results shows that the sensitivity of P_4 to

the dominant parameters is approximately 1.7 times the sensitivity of Q_3 to the same parameters. The simplified energy equation, Equation 3.2, offers some explanation for this. In this equation, the velocity, which is directly proportional to the flow rate, appears with an exponent of two, whereas the pressure has an exponent of unity. Applying a small change to the loss term while fixing the flow rate would cause a proportional change to the pressure. However, the same change in the loss term with the pressure fixed would cause a smaller change in the flow rate because of the exponent. The difference of the changes would be expected to be of the order of root two, but the jet pump model is much more complicated than this simple example, and it does not seem unreasonable that the uncertainty of the annulus pressure is of the order of double the uncertainty of the tertiary flow rate.

The five largest contributors to the uncertainty of P_4 are the same as for the flow Q_3, although there are slight differences in the order and magnitudes of the smaller contributors. As expected, most of the uncertainty arises from the mixing loss coefficient, which has the greatest influence on the momentum transfer in the mixing region, and hence on the overall performance of the jet pump.

4.4.3 Uncertainty of the Simulated Efficiency

Finally, the uncertainty of the simulated efficiency was calculated, and is summarized in Table 4.6. Also shown in the table are the top five contributors to the overall uncertainty of the efficiency.

Table 4.6: The relative expanded uncertainty of the jet pump efficiency η as calculated by the simulation, and the five largest contributors to the uncertainty expressed as a fraction of the total, at the 95% confidence level.

Relative Uncertainty $U_p(\eta)/\eta$		
mean: 84.5%	minimum: 72.3%	maximum: 101%

Top five contributors to the relative uncertainty		
Symbol	Parameter Description	Fraction
K_{mix}	mixing loss factor	96.2%
α	kinetic energy correction factor	1.8%
r_j	jet nozzle inlet radius	0.9%
f_3	annulus friction factor	0.3%
$K_{el,89}$	jet pump inlet elbow loss factor	0.2%
	Total of the top five contributors:	99.6%

The mean uncertainty of the efficiency is 85%, which is much greater than the uncertainties of the flow rates and pressures. This is expected because the efficiency is calculated from the pressures, flow rates, and elevations within the jet pump, and the uncertainties in these calculations are combined and amplified in the efficiency calculation.

The four largest contributors to the uncertainty of the efficiency are also responsible for most of the losses for Q_1 and Q_2, showing the significant effect these two flow rates have on the efficiency. As with the other parameters in the annulus, most of the uncertainty arises from the mixing loss coefficient, which has the greatest influence on the momentum transfer in the mixing region, the energy losses, and therefore the efficiency of the jet pump.

4.5 Comments on the Simulation Uncertainty

The expanded uncertainty of the measured volumetric flow rates and static pressures were of the order of one half to one percent. The efficiency, which is calculated from the flow rates and pressures, had an expanded uncertainty of the order of two percent.

The simulation, on the other hand, had a significantly higher uncertainty. The primary flow rate, despite it's simple model, had an expanded uncertainty of about four percent; this is an order of magnitude greater than than the measurements. The other flow rates had expanded uncertainties of the order of thirty percent. The uncertainty of the simulated efficiency was very high, around 85 %, rendering the efficiency calculation almost meaningless.

It is unlikely that the high condition number of the simulation matrices amplified or otherwise affected the uncertainty estimate. It was stated in Section 3.8 that the condition number of the simulation using CGS units was high, of the order of 10^7. A version of the simulation program written with MKS units had a much higher condition number, of the order of 10^{15}. Although MKS units affected the stability and convergence of the solution, the calculated results remained the same as with CGS units. Also, an iterative solver was used, which by its nature minimizes the numerical error of the result. Therefore it is believed that the uncertainty estimates were not affected by the high condition number of the simulation.

Despite the high uncertainty of the simulation results, it will be shown in

the following chapter that the simulation generally gave correct correlations between the design parameters, and had errors less than predicted by the uncertainty analysis.

CHAPTER 5

RESULTS AND DISCUSSION

5.1 Introduction

In this chapter, results of the experiments and simulations are presented. The first discussion covers the effect of the nozzle to throat separation distance, to establish that its effect is small and to justify the use of mean data for the remainder of the chapter. Next, the effects of the jet inlet pressure are discussed, followed by the effects of the nozzle to throat area ratio and number of jets. This chapter concludes with recommendations for designers of annular mixing jet pumps.

The experiments were performed in nine groups of five tests, for a total of 45 tests. Each of the nine groups had a fixed area ratio and number of jets, and the five tests within each group had a different nozzle to throat separation distance. Each of the 45 test configurations was run with the jet inlet pressure P_0 ranging from 344 kPa (50 psi) to a maximum of 689 kPa (100 psi) in 69 kPa

(10 psi) increments. The test schedule is found in Table B.1 in Appendix B, and the nozzle to throat distances used for the tests are listed in Table B.2.

Appendix B also includes the recorded and reduced data from the experiments. Figures B.1, B.2, and B.3 show the primary, secondary, and tertiary flow rates measured for each test configuration and jet inlet pressure. Figure B.4 shows the static pressures at the end of the annulus. Figure B.5 shows the flow ratio, and Figure B.6 presents the jet pump efficiency. For all plots, the estimated measurement or simulation uncertainty is shown with error bars; the larger error bars are for the simulation results.

The subsequent nine figures of Appendix B, Figures B.7 through B.15, show the static pressures along the mixing region. These plots show the mean pressures recorded for all five tests within the group, because it is shown in Section 5.2 that the nozzle to throat distance has only a very small effect on the pressure.

The reduced data, such as the flow ratio, head ratio, and efficiency, are common non-dimensional parameters used to describe the performance of jet pumps. These parameters are used in the following sections for the discussions of the effects of the four main parameters.

For consistency of the presentation and discussion, the experimental and simulation results are all named and numbered using the notation shown in Figures 3.1 and 3.2.

5.2 Effect of Nozzle to Throat Separation

The experiments were conducted in nine groups of five tests. Within each group, all tests used the same jet diameter and quantity, but each of the five tests used different nozzle lengths, and therefore different nozzle to throat separation distances. The shortest jets had their exit planes flush with the lower surface of the jet pump inlet, while the longest jets had their exit planes at the throat. It was found that the different nozzle lengths had some effect on the jet pump performance, and in this section, these effects are presented and discussed.

The experimental data were analyzed to determine the effect of the nozzle to throat distance on various parameters. For each test group, the mean value of the parameter of interest was calculated, then the deviation from this mean was calculated for each test point within the group.

The results for $P_0 = 483$ kPa (70 psi) are typical, and are shown as figures in the following sections. Figure 5.1 shows the effect of the nozzle to throat separation on the water flow rates in the jet pump. Next, Figure 5.2 shows the effect of the on the peak mixing pressure and mixing length. Finally, Figure 5.3 shows the effect on the flow ratio, the head ratio, and their product, the jet pump efficiency.

The simulation did not contain any models which could compensate for the effects of different nozzle to throat separation distances. Therefore, the simulation results are independent of this distance, and are not discussed.

5.2.1 Effect of Nozzle to Throat Separation on Flow Rates

The measured flow rates were analyzed to determine what effect the nozzle to throat separation distance had on the flow rates. The results for each test within a group were compared with the mean of the five tests within the group, and the percent deviations from these means are shown in Figure 5.1.

The three flow rates show similar results, with somewhat inconsistent curves for the test groups. The overall mean trend lines, however, suggest a slight increase in the flow rates as the nozzle to throat distance increases. Since the primary and secondary flows both show similar increases with the nozzle to throat separation, the flow ratio shows almost no dependence on the separation.

However, it is possible that this effect is the result of the shorter jet length alone, rather than the increased nozzle to throat separation, which is a by-product of the reduced jet length. The shorter nozzles would have slightly lower friction losses, increasing slightly Q_1 and leaving more energy to transfer to the secondary flow. The increased primary flow should have a proportional effect on Q_2 and Q_3. Finally, the slightly greater mean trends of Q_2 and Q_3, when compared to Q_1, could be the result of reduced flow obstruction by the nozzles as they are pulled away from the throat.

5.2.2 Effect of Nozzle to Throat Separation on Mixing

The measured values of the peak static mixing pressure P_3 were analyzed to determine what effect the nozzle to throat separation distance had on this

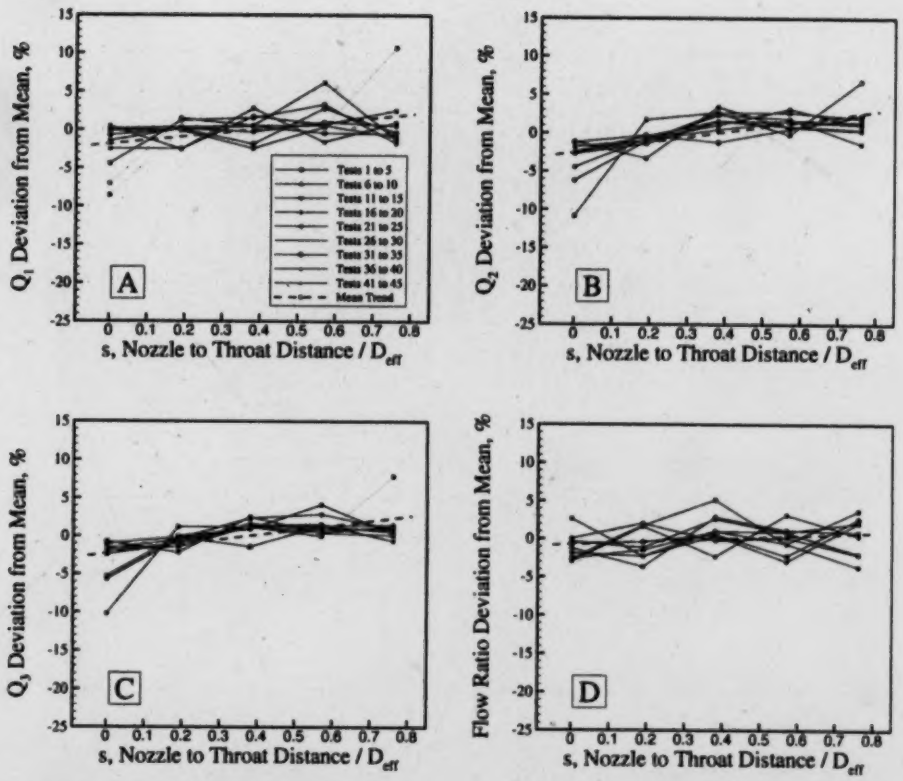

Figure 5.1: The flow rates Q_1, Q_2, and Q_3, and the flow ratio M, versus nozzle to throat separation s for jet inlet pressure $P_0 = 483$ kPa (70 psi). The figures show the percent deviation of the measured parameter from the mean of the five measurements within the group. $D_{eff} = 1.49$ cm.

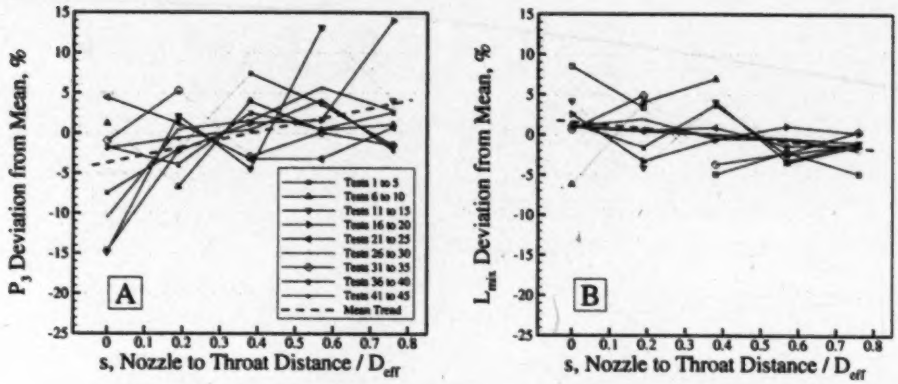
P3 Deviation from Mean, %
s, Nozzle to Throat Distance / Deff
A
Tests 1 to 5
Tests 6 to 10
Tests 11 to 15
Tests 16 to 20
Tests 21 to 25
Tests 26 to 30
Tests 31 to 35
Tests 36 to 40
Tests 41 to 45
Mean Trend
Lmix Deviation from Mean, %
s, Nozzle to Throat Distance / Deff
B

Figure 5.2: The peak mixing pressure P_3 and mixing length L_{mix} versus nozzle to throat separation s, for jet inlet pressure P_0 = 483 kPa (70 psi). The figures show the percent deviation of the measured parameter from the mean of the five measurements within the group. D_{eff} = 1.49 cm.

pressure, and on the length of annulus needed for complete mixing of the flows. As with the previous section, the results of each test were compared with the mean values for the test group, and the deviations are plotted in Figure 5.2.

It is clear from the irregular curve shapes of Figure 5.2 that the effect of s is not consistent. However, there appear to be general trends in the data, with a slight positive trend for peak pressure and a slight negative trend for mixing length as the separation increases. The magnitude of these trends is small, with the P_3 trend within $\pm$ 4 % and the L_{mix} trend within $\pm$ 1.5 % of their respective mean values. Given the inconsistent relationship between the nozzle to throat distance and the mixing phenomena, and the small overall deviation trends, further discussion of the mixing phenomena will use mean data calculated from all five tests within each test group.

5.2.3 Effect of Nozzle to Throat Separation on Efficiency

The experimental data were also analyzed to determine any effect the nozzle to throat separation had on the efficiency of the pump. As with the previous sections, the results of each test were compared with the mean values for the test group, and the deviations are plotted in Figure 5.3. This figure shows the three plots related to the efficiency; plot A shows the effect on the flow ratio, plot B shows the effect on the head ratio, and plot C shows the overall effect on the efficiency. It should be recalled that the efficiency is the product of the flow and head ratios.

It was stated in Chapter One that there is general agreement among researchers that the efficiency of a centre jet pump improves as the nozzles are moved upstream of the throat, reaching maximum efficiency when $1.0D_t \leqslant s \leqslant 2.0D_t$. The general trends in Figure 5.3 suggest that this is also the case with the annular mixing jet pump. The flow ratio shows a very small positive mean trend, varying less than $\pm$ 1 % from the mean, but the head ratio shows a much stronger trend, varying by about $\pm$ 5 %. The efficiency is the product of these two parameters, and as expected, it also shows a positive correlation with the separation, varying by about $\pm$ 5 %.

The literature suggest that further increases in efficiency could be achieved by increasing the nozzle to throat distance to a more optimal value. However, the physical geometry of the experimental model prevented any additional increase in the spacing; at maximum s, the nozzles of the model are flush with the lower surface of the jet pump inlet. It is conceivable though that an an-

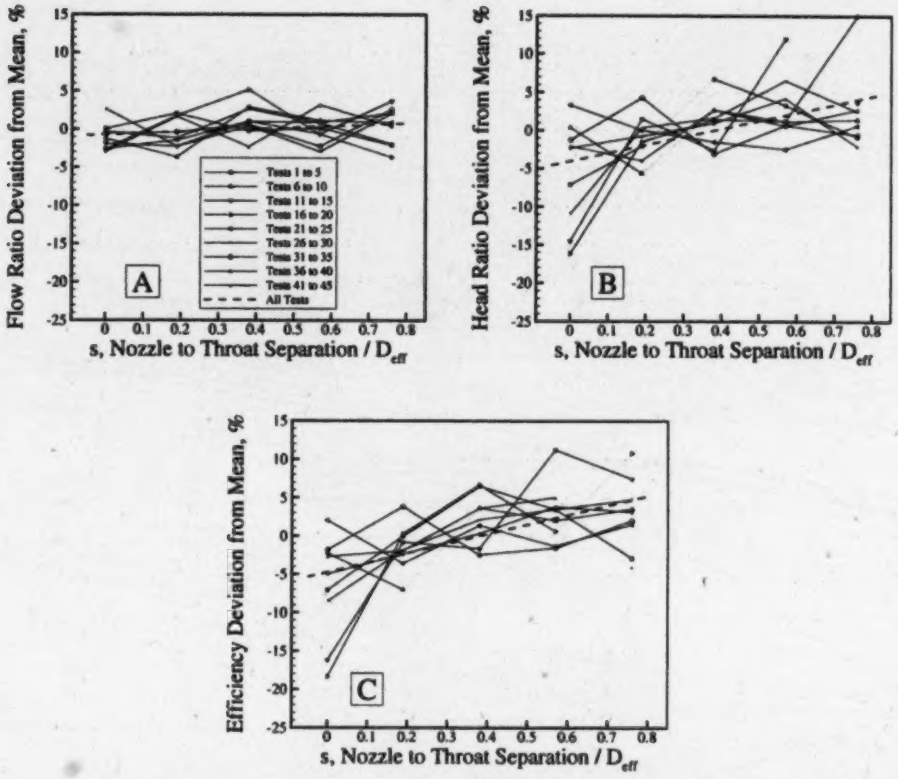

Figure 5.3: The efficiency η, the flow ratio M, and the head ratio N, versus nozzle to throat separation s for jet inlet pressure $P_0 = 483$ kPa (70 psi). The figures show the percent deviation of the measured parameter from the mean of the five measurements within the group. $D_{eff} = 1.49$ cm.

nular mixing jet pump could be built with a larger inlet radius, which could allow the designer to position the nozzles further upstream of the throat, giving further increases to the pump efficiency.

5.3 Effect of Jet Inlet Pressure

It was shown in the previous section that the nozzle to throat distance has only a small effect on the performance of the annular mixing jet pump. For the remaining sections, the effect of this distance will be removed by averaging the test results across each group. In this section, the effect of the inlet pressure P_0 is presented and discussed. The format of the data presentation will allow introduction to the effects of the area ratio and number of jets, but these effects will be explored in greater detail in subsequent sections.

The averaged results for the experiments and simulations are presented in three figures. Figure 5.4 shows the effect of the jet inlet pressure on the water flow rates in the jet pump. Next, Figure 5.5 shows the effect of the jet inlet pressure on the peak pressure in the mixing chamber. Finally, Figure 5.6 shows the effect on the flow ratio, the head ratio, and their product, the pump efficiency.

5.3.1 Effect of Jet Inlet Pressure on Flow Rates

The averaged flow rates for each test group, and the corresponding simulation results, were plotted against the jet inlet pressure to determine the effects of the inlet pressure on the flow rates; these plots are shown in Figure 5.4.

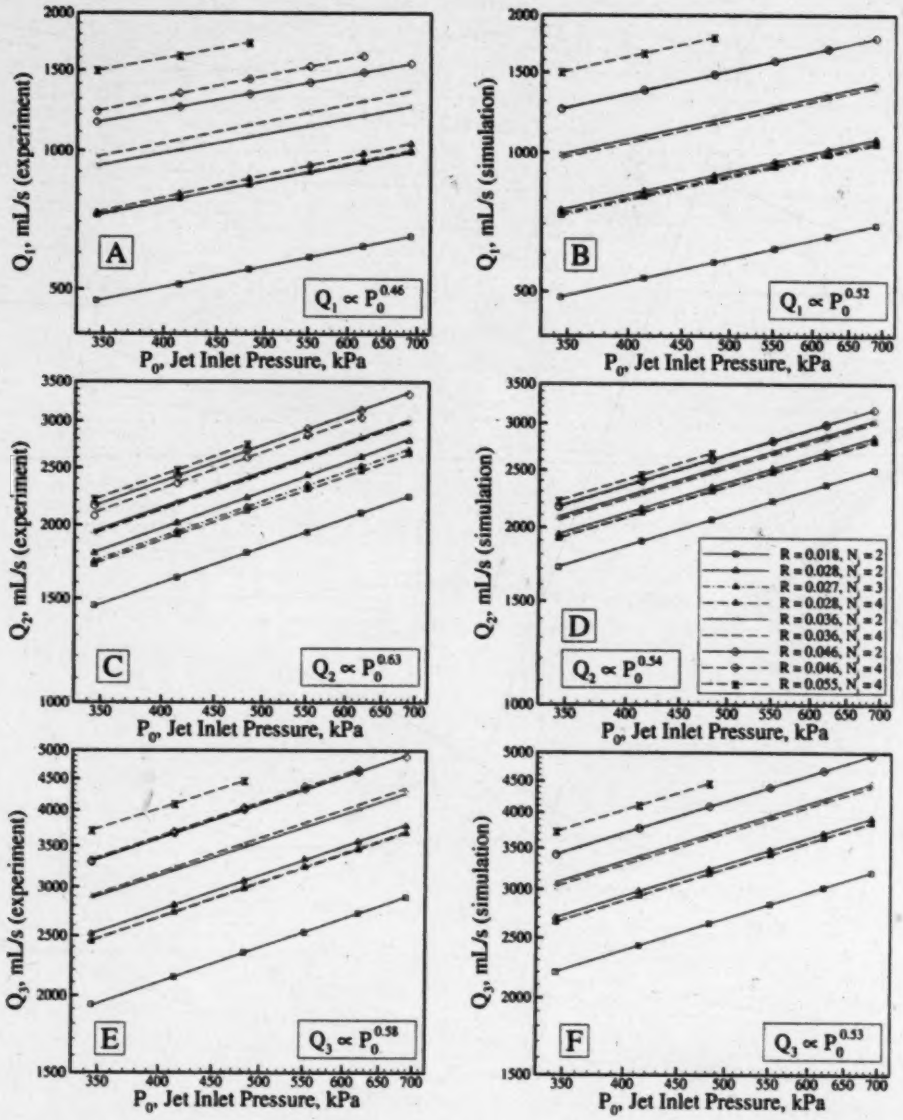

Figure 5.4: The primary, secondary, and tertiary flow rates Q_1, Q_2, and Q_3, versus the jet inlet pressure P_0, using experiment (left column) and simulation (right column) results. Each curve represents the mean data for a test group. The indicated slope is the mean value of least-squares curve fits for each line.

As expected, the flow rates increase steadily with the jet inlet pressure. By plotting Figure 5.4 on log-log axes, one can see that the data form straight, parallel lines, indicating that the data in each plot follow power functions with constant exponents. The curves were fitted to least-squares power functions, from which the mean slopes of the curves were determined; these are displayed on the individual plots in Figure 5.4.

From the simplified one-dimensional energy equation (Equation 3.2) without the elevation or loss terms, one would expect $Q^2 \propto P$, or $Q \propto P^{0.5}$. However, other terms or factors will affect the relationship between the flow rate and static pressure, and affect the exponent on P. If some terms include the flow rate at less than second order, such as elevation changes (zero-order), the lower-order terms will reduce the overall effective order of the equation, making the exponent to P greater than 0.5. Conversely, if some terms include the flow rate at orders greater than two, the overall order of the flow rate terms will be greater than two, and the exponent to P will be less than 0.5. Such deviations can arise from real energy losses which correlate to the flow rate at orders other than two, and from the kinetic energy correction factor α, which is a function of the velocity profile and depends on the velocity and degree of flow development.

The experimental data for Q_1 show good agreement with the simulation, with similar magnitudes and slopes for the two data sets. The fitted experimental data curves have a mean exponent of 0.46, slightly lower than the simulation result of 0.52. The simulation used second-order loss models

with a small elevation change, which is consistent with a mean curve slope of slightly more than 0.5. The simulation did not account for friction nor the complex three-dimensional flow patterns within the jet inlet plenum, and assumed fully developed flows in the jet nozzles. Since the experiment data gave an exponent to P_0 of less than 0.5, the data suggest that these flow losses correlate to the flow rate at somewhat greater than second order.

The secondary flow gave experimental curves with an exponent of 0.63, somewhat higher than the expected 0.5. This suggests an effect of lower-order terms; the elevation changes associated with Q_2 are small, so it is possible that the mixing process has lower-order components. The simulation results were fitted to curves with an exponent of 0.54. This appears reasonable considering that all the energy loss models are second-order, and that there is a larger elevation pressure change term than for Q_1.

The curves fitted to the experimental data for Q_3 have a mean exponent of 0.58. The tertiary flow is a combination of the primary and secondary, so it seems reasonable that the exponent should lie between the values for these other flows; a simple weighted average of the exponents for Q_1 and Q_2 also gives 0.58. The similar case exists for the simulation results, with an exponent of 0.53 which falls between those for Q_1 and Q_2.

The effects of the area ratio and jet quantity should be readily apparent in Figure 5.4, and these will be discussed in more detail in subsequent sections. The flow ratio will be discussed in Section 5.3.3, as part of the discussion of the effect of P_0 on the efficiency.

5.3.2 Effect of Jet Inlet Pressure on Mixing

The mean peak mixing pressure for each test group, and the corresponding simulation results, were plotted against the jet inlet pressure to determine what effect the inlet pressure has on the peak pressure. These plots are shown in Figure 5.5.

As with the flow rates, the peak mixing pressure also increases steadily with the jet inlet pressure. This effect is linear, rather than a power function as with the flow rates, because the static pressure is a linear term in the one-dimensional energy equation.

Compared with the experiment, the simulation generally over-estimates the peak mixing pressure, with the results at $P_0 = 345$ kPa varying from zero to ten percent higher than the experiment data, and rising more quickly with P_0. This appears to be a result of the simulation under-estimating the losses during mixing. This conclusion is drawn by considering the data for $R = 0.036$ (with the "◇" symbol). In Figures 5.4E and 5.4F, the experiment and simulation results for Q_3 at $R = 0.036$ are very close, with both ranging from 2900 mL/s to 3600 mL/s. However, the corresponding results for P_3 in Figures 5.5A and 5.5B show the experimental results ranging from 24 kPa to 36 kPa, while the simulation results are higher, ranging from 27 kPa to 43 kPa. Since the flow rates and elevations are the same, the higher value of P_3 must be the result of a higher energy state in the flow, which would come from lower losses. Since the mixing loss is the most significant loss in the jet pump, it is most likely that inaccuracies in the mixing model cause the

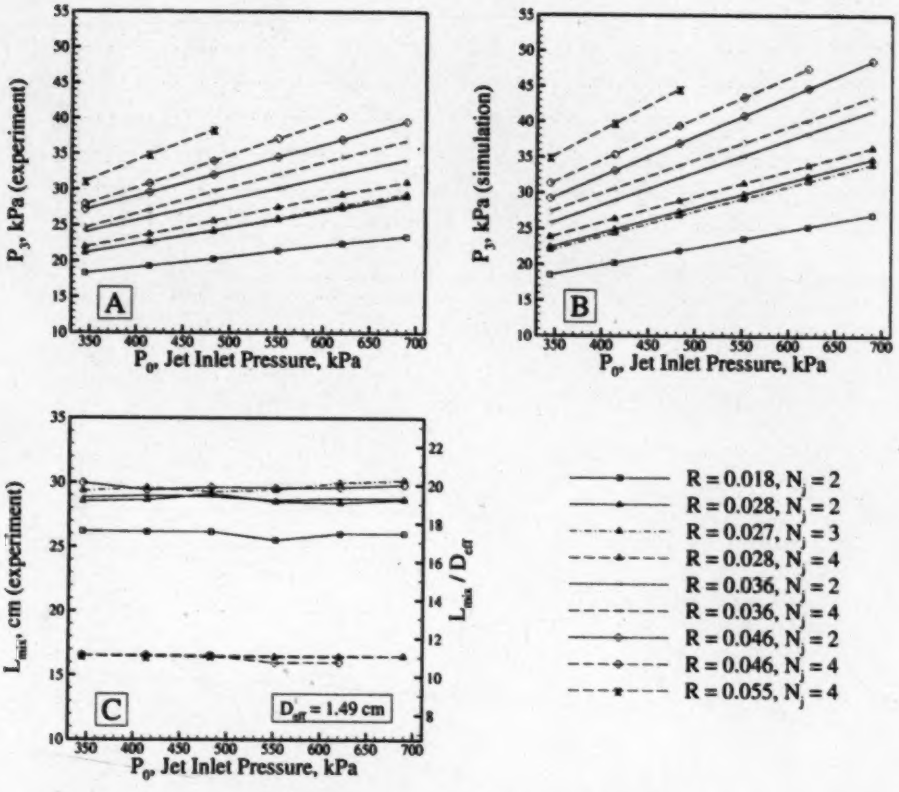
P3, kPa (experiment)
A
P0, Jet Inlet Pressure, kPa
P3, kPa (simulation)
B
P0, Jet Inlet Pressure, kPa
Lmix, cm (experiment)
Lmix / Deff
C
Deff = 1.49 cm
P0, Jet Inlet Pressure, kPa
R = 0.018, Nj = 2
R = 0.028, Nj = 2
R = 0.027, Nj = 3
R = 0.028, Nj = 4
R = 0.036, Nj = 2
R = 0.036, Nj = 4
R = 0.046, Nj = 2
R = 0.046, Nj = 4
R = 0.055, Nj = 4

Figure 5.5: The peak mixing pressure P_3 and mixing length L_{mix} versus jet inlet pressure P_0, using experiment (left side) and simulation (right side) results. Each curve represents the mean data for a test group. The simulation used fixed values of L_{mix} = 16.4 cm (11 D_{eff}) for $N_j = 4$, and 29.8 cm (20 D_{eff}) for $N_j = 2$ and 3.

discrepancy between the experimental and simulation results. Development of an improved one-dimensional mixing model for this geometry, or the use of two- or three-dimensional models, should improve the mixing model and increase the simulation accuracy.

Figure 5.5C shows that the mixing length is independent of the jet inlet pressure. This is likely because the geometry is fixed and flows remain turbulent across the full range of P_0, so the overall flow patterns remain unchanged for all values of the jet inlet pressure.

As was the case with the flow rates, the effects of the area ratio and jet quantity should be apparent in Figure 5.5; these will be discussed in more detail in subsequent sections. The head ratio will be discussed in Section 5.3.3, as part of the discussion of the effect of P_0 on the efficiency.

5.3.3 Effect of Jet Inlet Pressure on Efficiency

The effects of the jet inlet pressure on the efficiency of jet pump are shown in Figure 5.6. In these plots, the measured values of the flow ratio, head ratio, and efficiency were averaged for each test group, then plotted against the jet inlet pressure. The corresponding simulation results are also shown.

Figure 5.6 shows that M increases somewhat with an increase in P_0, with a flow ratio increase of about ten percent over the full range of inlet pressures. This dependency is proportional to $P_0^{0.17}$, which is the quotient of the functions for Q_2 and Q_1 shown on Figure 5.4. A similar response is seen with the simulation results, but since the simulation gave nearly identical

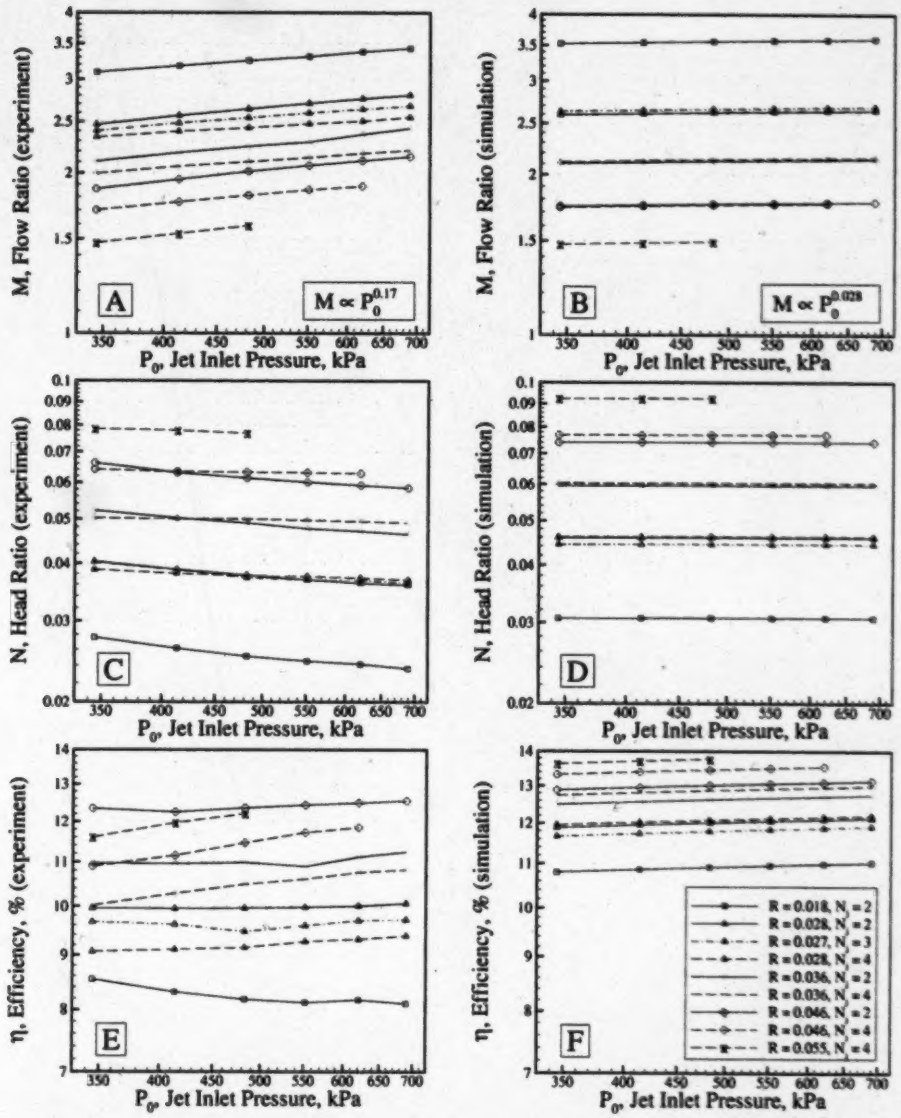
M, Flow Ratio (experiment)
M, Flow Ratio (simulation)
N, Head Ratio (experiment)
N, Head Ratio (simulation)
η, Efficiency, % (experiment)
η, Efficiency, % (simulation)
P0, Jet Inlet Pressure, kPa
A
B
C
D
E
F
M ∝ P0^0.17
M ∝ P0^0.028
R = 0.018, N = 2
R = 0.028, N = 2
R = 0.027, N = 3
R = 0.028, N = 4
R = 0.036, N = 2
R = 0.036, N = 4
R = 0.046, N = 2
R = 0.046, N = 4
R = 0.055, N = 4

Figure 5.6: The flow ratio M, head ratio N, and jet pump efficiency η versus jet inlet pressure P_0, using experiment (left column) and simulation (right column) results. Each curve represents the mean data for a test group.

slopes for Q_1 and Q_2 versus P_0, the simulation results for the flow ratio are almost independent of the jet inlet pressure.

The head ratio shows a general decrease with P_0, losing between two and fourteen percent across the full pressure range depending on the number of jets. In contrast, the simulation results for the head ratio are completely independent of the jet inlet pressure. These differences are correlated with the experiment and simulation results for P_3, in which the experiment data had lower values and slopes than the simulation results.

The efficiency results for the experiment data are somewhat inconsistent, since they are dependent on the number of jets, and to a lesser extent, the area ratio. Most of the results for two or three jets show the efficiency to be independent of the jet inlet pressure. However, the results for four jets show an increase in efficiency as P_0 increases, rising by about ten percent across the full inlet pressure range.

The dependency of the experimental flow and head ratios on the number of jets will be discussed further in Section 5.5.3.

5.4 Effect of Area Ratio

In this section, the effect of the nozzle to throat area ratio is presented and discussed. As with the discussion of jet inlet pressure effects, the results presented in this section use average data for a test group to remove the effect of the nozzle to throat separation distance.

The averaged results results for the experiments and simulations are pre-

sented in three figures. Figure 5.7 shows the effect of the area ratio on the volumetric flow rates in the jet pump. Next, Figure 5.8 shows the effect of the area ratio on the mixing processes, and finally, Figure 5.9 shows the effect on the flow ratio, the head ratio, and their product, the pump efficiency.

The plots presented in this section use the data for a jet inlet pressure of 483 kPa (70 psi). This pressure is in the middle of the test range, is representative of all pressures, and was used with all test groups.

5.4.1 Effect of Area Ratio on Flow Rates

It was first shown in Section 5.3.1 that the area ratio has a strong effect on the flow rates in the pump. As can be seen in Figure 5.4, as the area ratio increases, so too do all three flows. This is expected, since a larger area ratio implies a larger jet area, which offers lower resistance to the primary flow, and therefore allows a higher primary flow rate. A higher primary flow brings with it more energy, which in turn causes higher secondary and tertiary flows.

The volumetric flow rates for $P_0 = 483$ kPa (70 psi) are shown in Figure 5.7. The data points represent mean flow rates for the area ratio, averaged to remove the effects of nozzle to throat separation and number of jets, and then fitted with least squares power functions.

Figure 5.7 shows how, for a fixed jet inlet pressure, increasing the area ratio gives higher flow rates in the jet pump. The simulation results are similar for all three flow rates, although the slopes for the simulated secondary and tertiary flows are slightly lower than the experimental results.

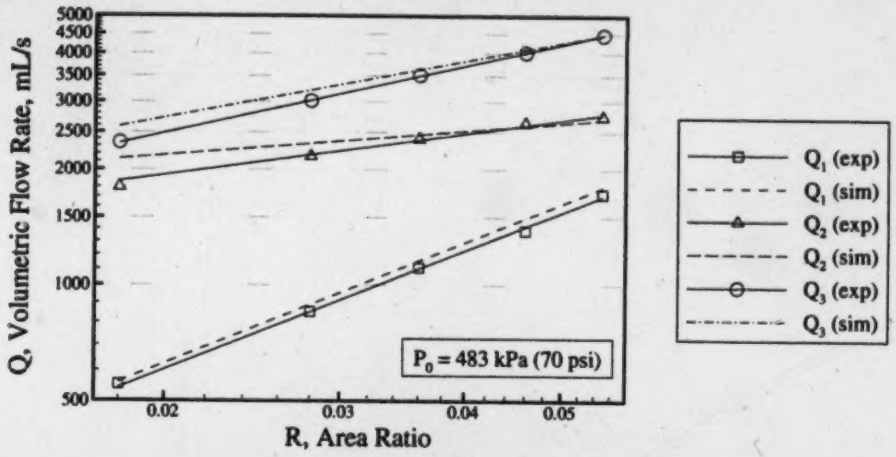

Figure 5.7: The primary, secondary, and tertiary flow rates Q_1, Q_2, and Q_3, versus the area ratio R using experiment and simulation results. Jet inlet pressure $P_0 = 483$ kPa (70 psi). Each curve represents the mean data for all tests at each area ratio.

5.4.2 Effect of Area Ratio on Mixing

Figure 5.5 in Section 5.3.2 illustrated the effect the area ratio had on the peak mixing pressure, showing that P_3 increased with R. It was less clear, however, the effect of R on the mixing length. Figure 5.8 shows the mixing data for $P_0 = 483$ kPa (70 psi) and better illustrates the effects of area ratio on the mixing processes.

The area ratio has a linear effect on the peak mixing pressure, with P_3 rising with R. The simulation shows a similar trend, but with somewhat higher pressures and slope.

The mixing length appears to be mostly insensitive to changes in the area ratio, although the mixing length for $N_j = 2$ and $R = 0.018$ appears to be

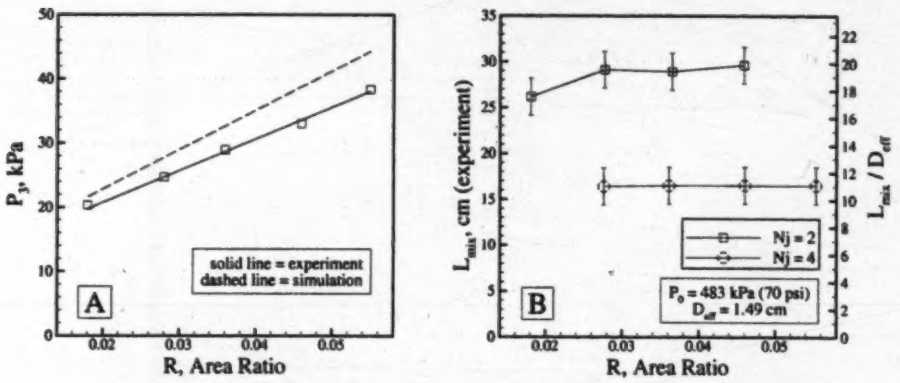

Figure 5.8: The peak mixing pressure P_3 and mixing length L_{mix} versus area ratio R, using experiment and simulation results. Jet inlet pressure P_0 = 483 kPa (70 psi). Each curve represents the mean data for all tests at each area ratio. The simulation used fixed values of L_{mix} = 11 D_{eff} for $N_j = 4$ and 20 D_{eff} for $N_j = 2$ or 3.

about 3 cm (2 D_{eff}) shorter than the other results for $N_j = 2$. It should be noted, however, that the uncertainty of the mixing length estimates is approximately 2 cm, so there is some possibility that the area ratio has no substantial effect on the mixing length.

5.4.3 Effect of Area Ratio on Efficiency

The effects of the area ratio on the efficiency of jet pump are shown in Figure 5.9. In these plots, the measured values of the flow ratio, head ratio, and efficiency were averaged for each test group, then plotted against the area ratio. The corresponding simulation results are also shown.

In Figure 5.9, the flow ratio is seen to decrease as the area ratio increases. This was evident in Figure 5.7, in which the curves for Q_1 and Q_2 converge.

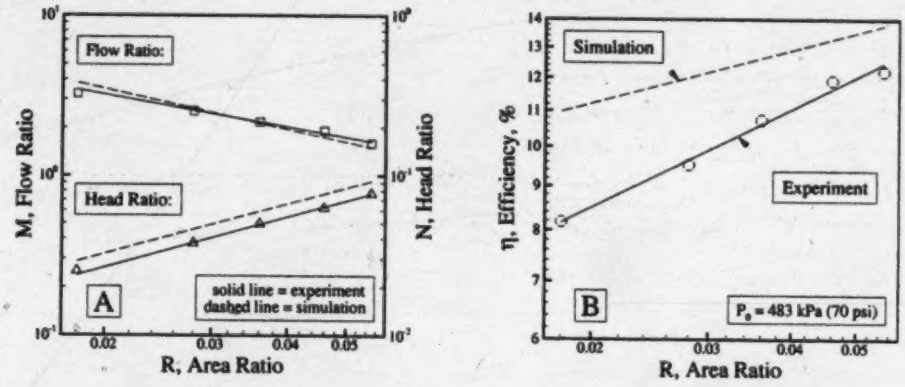

Figure 5.9: The flow ratio M, head ratio N, and jet pump efficiency η versus area ratio R, using experiment and simulation results. Jet inlet pressure P_0 = 483 kPa (70 psi). Each curve represents the mean data for all tests at each area ratio.

The experimental data curves can be extrapolated to a crossing point at $R = 0.123$, at which point the flow ratio equals unity.

One way to interpret the effect of the area ratio on the flow ratio is to consider a jet pump with a fixed jet area and jet inlet pressure. Changes to the mixing region of the jet pump will have a negligible effect on the flow through the jets, which may be considered constant. Now consider the effect of changing the throat area; as this is increased, the secondary and tertiary flows will slow. This will result in lower friction losses, giving higher secondary and tertiary flow rates. However, with the primary flow rate constant, the overall effect is an increased flow ratio.

The head ratio increases with the area ratio, as might have been expected from Figure 5.8, in which it was shown that P_3 increases with R. The simu-

lation results for the head ratio are consistently higher than the experimental data, following a parallel curve about 20% higher.

The efficiency was found to increase with the area ratio. For the range of jet inlet pressures tested, the flow ratio decreased from 3.25 to 1.59, or a reduction of one half, while the head ratio increased from 0.025 to 0.077, or a three-fold increase. The larger change of the head ratio dominates the efficiency calculation, giving a net increase of with area ratio. The simulation results show the same trend, but with higher values for the efficiency.

5.5 Effect of Number of Jets

In this section, the effect of the number of jets on the jet pump performance is presented and discussed. As with the discussion of jet inlet pressure effects, the results presented in this section use average data for a test group to remove the effect of the nozzle to throat separation distance.

The averaged results for the experiments and simulations are presented in three figures. Figure 5.10 shows the effect of the jet quantity on the volumetric flow rates in the jet pump. Next, Figure 5.11 shows the significant effect the number of jets has on the mixing processes, and finally, Figure 5.14 shows the effect on the flow ratio, head ratio, and efficiency.

As with the previous section, the plots in this section present data for a jet inlet pressure of 483 kPa (70 psi) as a representative middle pressure.

5.5.1 Effect of Number of Jets on Flow Rates

It was first shown in Section 5.3.1 that the number of jets has a small effect on the flow rates within the jet pump. In Figure 5.4, the plot of the flow rates versus the jet inlet pressure, three curves are shown for $R = 0.028$, and two are shown for $R = 0.036$ and $R = 0.046$. Each curve represents a different number of jets. From this figure, it is readily apparent that the flow rates for $N_j = 2$ are somewhat lower than for $N_j = 4$. The one case with $N_j = 3$, which occurs with $R = 0.036$, suggests that model configurations with two or three jets have similar performance.

The volumetric flow rates are plotted against the jet quantity for $P_0 =$ 483 kPa (70 psi) in Figure 5.7. The data points represent mean flow rates for the given number of jets, averaged to remove the effects of nozzle to throat separation. One curve is shown for each area ratio for which two or more different values of N_j were used.

As can be seen in Figure 5.10, the general effect of the number of jets on the flow rates is very small, with most of the experimental and simulation results showing very small differences between two and four jets.

For a fixed area ratio, the simulation predicted that the primary flow rate decreases as the number of jets increases. This would be expected because four jets should have slightly higher friction losses than two jets. For a fixed area ratio, an increase in the number of jets requires a decrease in the jet diameter, although the flow velocities in the jets would remain constant. The constant velocity and smaller diameter would decrease the Reynolds number

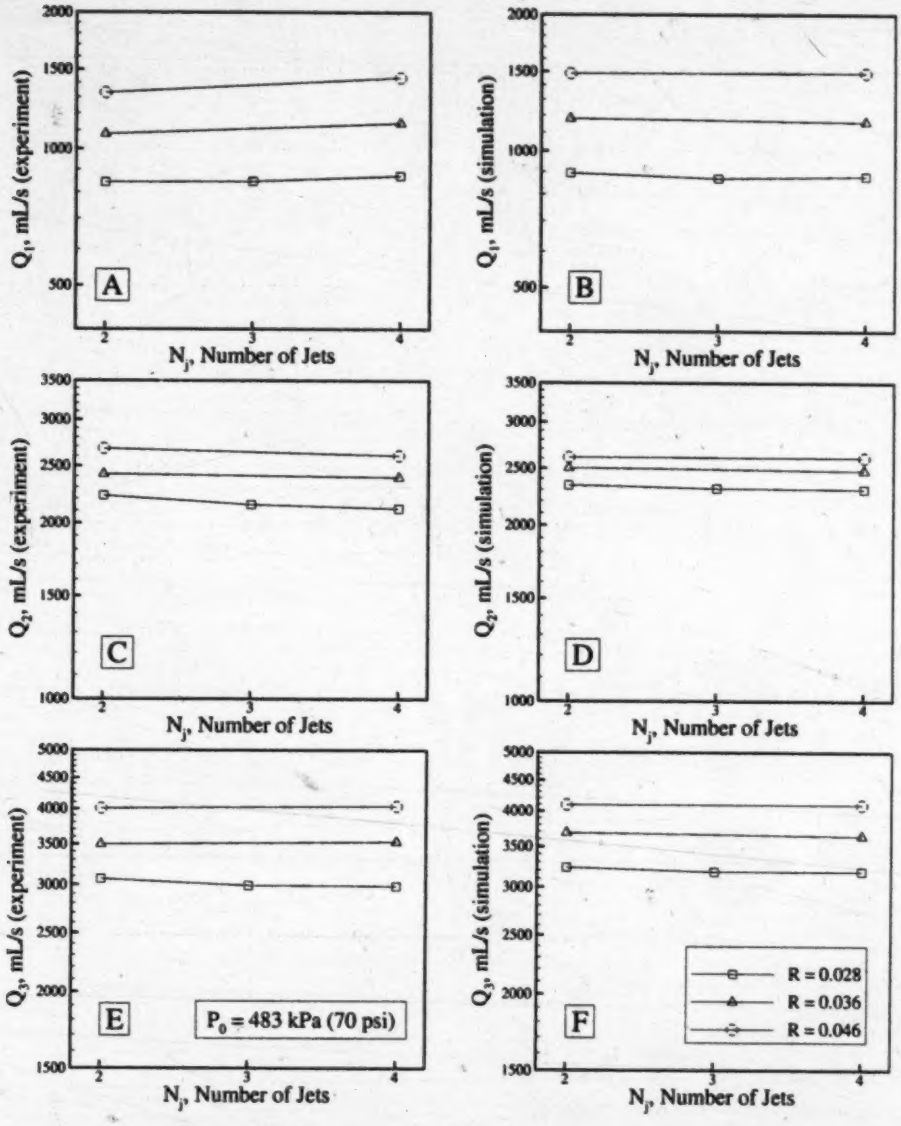

Figure 5.10: The effect of the number of jets on the measured flow rates Q_1, Q_2, and Q_3 for jet inlet pressure P_0 = 483 kPa (70 psi), using experiment (left column) and simulation (right column) results. Each curve represents a fixed area ratio. Data points are mean values calculated from the five tests within each test group.

and increase the relative roughness, and the Colebrook equation would return a higher friction factor.

The experiment data for Q_1 show the opposite effect, with the primary flow rate increasing with the number of jets. This may be the result of lower losses at the sudden contraction into the jet nozzles (node 1 in Figure 3.1). For a fixed nozzle inlet edge radius, a smaller diameter nozzle would have a lower rounded inlet loss coefficient than a larger diameter nozzle, and therefore lower losses at the contraction. However, it is unclear why this effect was not also seen in the simulation results.

The experiment and simulation give consistent results for the secondary and tertiary flow rates, with both showing small decreases in these flow rates as the number of jets increases.

5.5.2 Effect of Number of Jets on Mixing

Figure 5.5 in Section 5.3.2 illustrated the effect of the number of jets on the peak mixing pressure, showing that P_3 increased with N_j. It was later shown in Figure 5.8 that, while the mixing length is largely independent of the area ratio, it is strongly dependent on the number of jets.

It has been found that peak efficiency for a jet pump is obtained when the mixing process is complete at the end of the mixing tube, just before the mixed flow enters a diffuser. Most jet pump researchers agree that for a centre jet pump, a mixing tube length in the range of seven to ten tube diameters is optimum, although good performance has been reported for

tube lengths as little as 5.6 diameters (Bonnington and Hemmings, 1976). Assuming the effective hydraulic diameter of the annulus to be a suitable analogue to tube diameter of a circular pipe, the experimental model was built with sixteen pressure taps positioned in the range of 1.5 to 16 effective diameters, spaced approximately one effective diameter apart, to cover the expected mixing length.

Figure 5.11 shows three typical pressure profiles within the mixing region of the jet pump. All figures represent an area ratio $R = 0.036$ with differing numbers of jets. Shown in these figures is the maximum pressure, which corresponds to P_3, and the axial distance from the throat at which this pressure occurs, which gives the mixing length L_{mix}.

The general shape of the mixing pressure curves shows an interesting phenomenon. Figure 5.11C, the curve for $N_j = 4$, shows a brief pressure drop just after the throat, which is probably caused by the irrotational acceleration of the secondary fluid by the jet. After the initial drop, the pressure begins to rise as energy is transferred from the jets to the secondary fluid, and the pressure recovers its initial value after about three effective diameters. From this point, the pressure continues to rise until mixing is complete. This occurs after another eight effective diameters, for a total mixing length of about 11 D_{eff}. After complete mixing has occurred, the pressure shows the gradual decay consistent with wall friction losses.

The pressure profile shown in Figure 5.11C is consistent with the profile for a centre jet pump as reported by Sanger (1970), Schmitt (1975), and

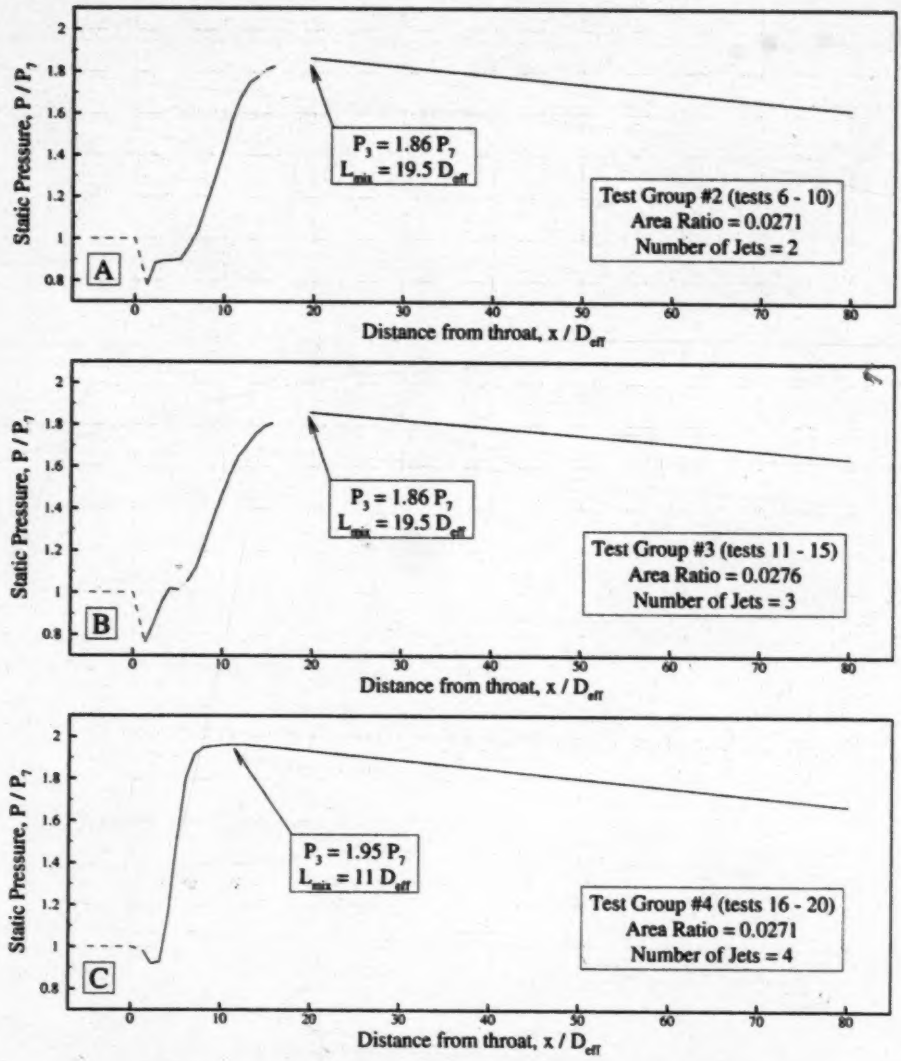
Static Pressure, P / P7
Distance from throat, x / Deff
P3 = 1.86 P7
Lmix = 19.5 Deff
Test Group #2 (tests 6 - 10)
Area Ratio = 0.0271
Number of Jets = 2
A
P3 = 1.86 P7
Lmix = 19.5 Deff
Test Group #3 (tests 11 - 15)
Area Ratio = 0.0276
Number of Jets = 3
B
P3 = 1.95 P7
Lmix = 11 Deff
Test Group #4 (tests 16 - 20)
Area Ratio = 0.0271
Number of Jets = 4
C

Figure 5.11: The effect of the number of jets on the static pressure profiles within the jet pump mixing region and annulus. For all cases, the area ratio $M \approx 0.03$ and the jet inlet pressure $P_0 = 483$ kPa (70 psi). $P_7 = 13.0$ kPa and $D_{eff} = 1.49$ cm. Solid curves show mean values calculated from the five tests within each group, and dashed curves are estimated pressures.

others. However, a centre jet pump has a mixing length in the range of 5.6 to 10 diameters, so a mixing length of 11 effective diameters for $N_j = 4$ is longer than for a conventional centre jet pump.

The curve for $N_j = 2$, plotted in Figure 5.11A, shows a much different profile. The profile begins as with $N_j = 4$, with a pressure drop at the start of mixing followed by a pressure rise. However, instead of continuing rapidly to a maximum, the pressure levels at a plateau over a length of about 3 D_{eff} before continuing toward the maximum. The final pressure rise also occurs slower than for $N_j = 4$, requiring approximately six additional diameters to reach its maximum. The combination of the pressure drop and extended rise increase the mixing length to nearly twenty effective diameters.

It is the author's opinion that the pressure plateau located between 2 and 5 D_{eff} in Figure 5.11A is evidence of a recirculation region between the jets. Very similar phenomena have been observed in confined jets (Hill, 1965; Rajaratnam, 1976) and annular jet pumps (Elger et al., 1994). In conventional jet pumps, a recirculation region forms when the secondary flow becomes fully entrained by the jet before the jet expands to its physical boundary. This boundary is either the mixing chamber wall of a centre jet pump, or the central axis of an annular jet pump. After full entrainment occurs, the recirculation region allows the jet to continue expanding smoothly to the boundary, at which point the recirculation region ends. Time-averaged streamlines showing the recirculation in centre and annular are shown in Figure 5.12A and B.

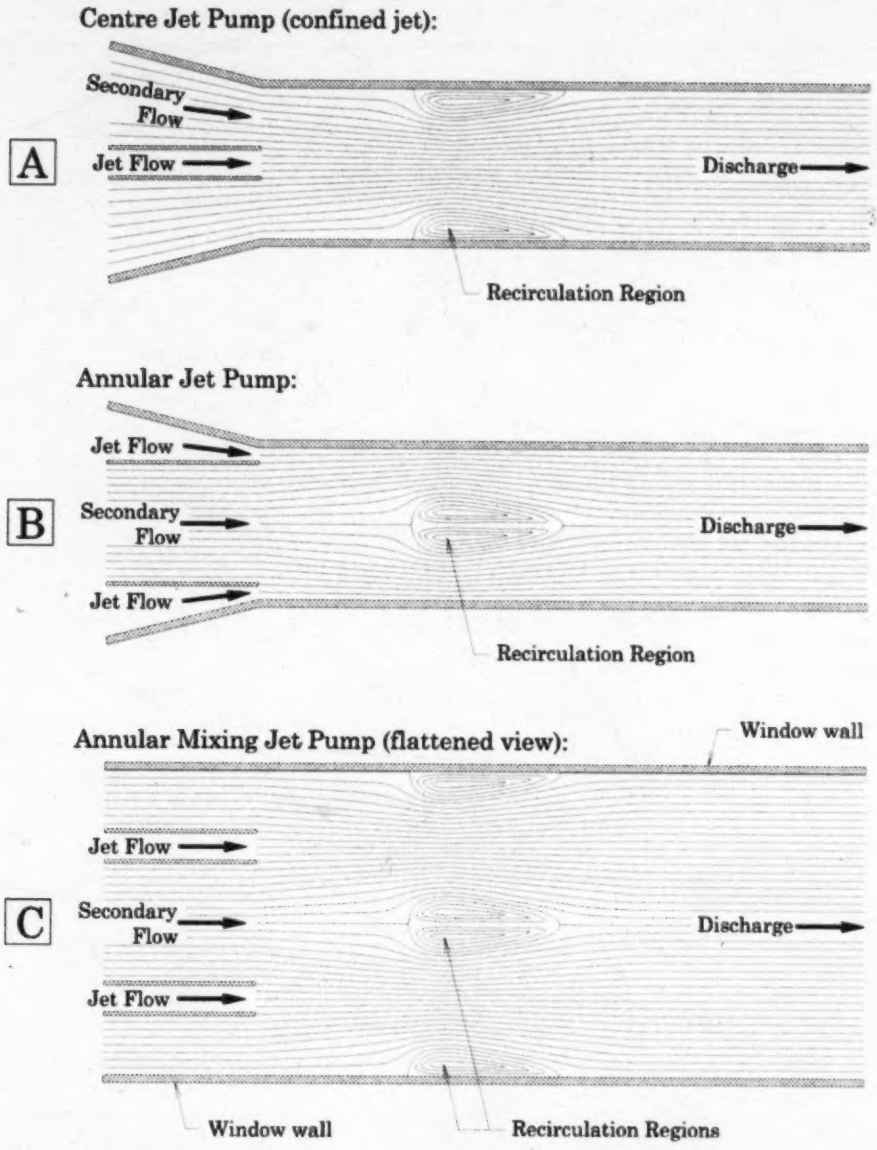

Figure 5.12: Section views showing time-averaged streamlines and recirculation patterns for a confined jet (Hill, 1965) and annular jet pump (Elger et al., 1994), and the proposed recirculation structure in the annular mixing jet pump.

Hill (1965) found that within a recirculation region, the static pressure remains approximately constant. Therefore, the constant-pressure plateau between 2 and 5 D_{eff} in Figure 5.11A may be evidence of a recirculation region.

Further evidence of recirculation was observed during visualization experiments with two jets; an image of the flow is shown in Figure 5.13. In this image, visualization dye was injected into the primary flow. The spreading of the jet plumes is clearly visible, but one may also see a region containing dye located between the jets, beginning about 5 cm (3 D_{eff}) from the throat. It is believed that this dye-marked area indicates a recirculation region between the two jets.

Two other recirculation zones may also have formed between the jets and the window. These appear smaller than the main recirculation between the jets. These zones were observed to start at about the same downstream position as the main zone, although images were captured showing the start varying by as much as three centimetres (2 D_{eff}) upstream or downstream.

Figures 5.12A and B show the time averaged streamlines for centre and annular jet pumps, and the typical location where a recirculation region may form. These two jet pumps are axisymmetrical, so the recirculation zone is shaped like an elongated torus. Using these two types of jet pumps as models, a proposed recirculation zone structure for the annular mixing jet pump is shown in Figure 5.12C. The illustration shows a flattened view of the experimental model mixing region, with two jets and the window walls.

Figure 5.13: Image of mixing region, showing recirculation zone between the jets marked by coloured dye. $R = 0.018$, $N_j = 2$, and $P_0 = 689$ kPa (100 psi).

A recirculation zone is shown between the two jets, as well as two other zones between the jets and the windows.

In Figure 5.12C, the flow on the streamline between the jets would slow as it approaches the recirculation, and eventually stop. Further downstream, the flow within the recirculation would be reversed. The stagnation point appears on the pressure profile in Figure 5.11A as the starting point of the pressure plateau, and this also correlates with the image in Figure 5.13 as the line between the jets above which dye is visible.

The curve for $N_j = 3$ is similar to that for $N_j = 2$. It shows only a small step during the pressure rise, which is delayed and not as pronounced as for the case with two jets. After the shorter pressure plateau, the pressure rises with a slope less than that for $N_j = 2$, and is fully mixed after 19.5 D_{eff}.

The smaller pressure plateau and slower pressure rise may result from the location of the middle jet. With two and four jets, the line of pressure taps was located midway between two jets, but with three jets, the middle jet flowed directly over all the pressure taps. One would expect no recirculation within the jet core, although a nearby recirculation zone could affect the measured pressure. The high jet velocity should give lower static pressure measurements, which may explain the delayed pressure rise. The mixing lengths for two and three jets were the same, suggesting similar structure to the mixing process.

Appendix B contains plots of the mixing pressures for all of the test groups, averaged across the group to remove the effect of the nozzle to throat

separation distance. The patterns described above for two and four jet configurations are clearly evident for all the tests.

5.5.3 Effect of Number of Jets on Efficiency

The effects of the number of jets on the jet pump efficiency are shown in Figure 5.14. In these plots, the measured values of the flow ratio, head ratio, and efficiency were averaged for each test group, then plotted against the jet quantity. The corresponding simulation results are also shown.

It was shown in Figures 5.10A and 5.10C that Q_1 increased slightly and Q_2 decreased slightly as the number of jets increased. This is also seen in Figure 5.14A, where the flow ratio decreases as the jet quantity increases. The simulation results for flow ratio appear independent of the jet quantity.

The head ratio, however, shows only a very slight increase with the number of jets. This is despite the observation from Figure 5.11 that the peak mixing pressure for pumps with four jets is higher than for two or three jets. However, the higher peak pressure is reached after a shorter mixing length, resulting in lower friction losses. Furthermore, the experimental model was installed vertically, so the shorter mixing length for $N_j = 4$ results in less elevation head. These two effects combine to give a total head at point three which is independent of the number of jets, and a similar effect on the head ratio. The simulation results are similar to those obtained from the experiments, with head ratios constant or increasing slightly with the number of jets.

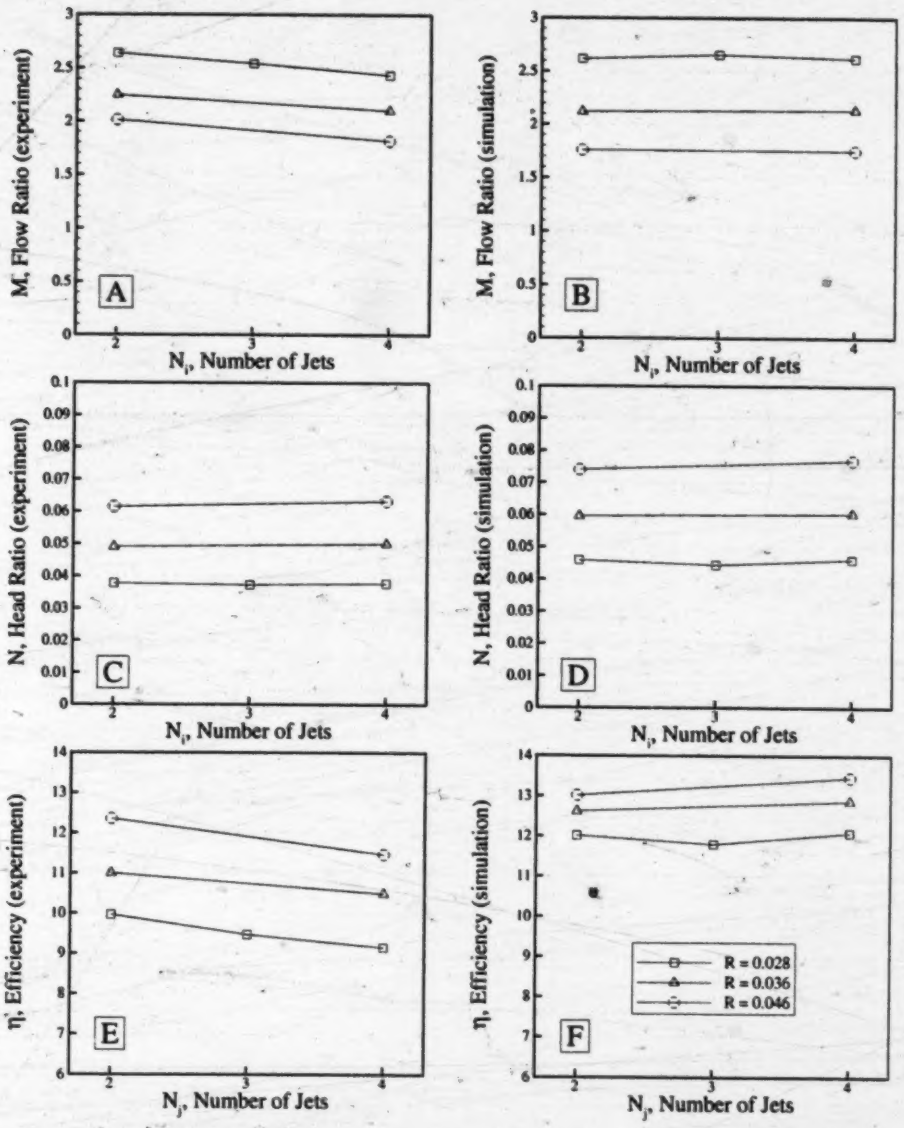

Figure 5.14: The effect of the number of jets on the measured flow ratio M, head ratio N, and efficiency η for jet inlet pressure $P_0 = 483$ kPa (70 psi), using experiment (left column) and simulation (right column) results. Each curve represents a fixed area ratio. Data points are mean values calculated from the five tests within each test group.

A constant head ratio and decreasing flow ratio combine to give a jet pump efficiency which decreases with an increase in the number of jets. The simulation results, however, show an efficiency which remains constant or increases with the number of jets. This is the logical result of the flow and head ratio results, which were constant or slightly increasing.

5.6 Cavitation

The phenomenon of cavitation is associated with many types of pumps, including jet pumps. As introduced in Section 1.2.2.3, jet pump cavitation may occur in the mixing region of jet pumps which handle liquids. It was shown in Figure 5.11 that as the secondary flow is accelerated during the initial mixing stage, its static pressure drops. If the static pressure falls below the vapour pressure of the liquid, the fluid will begin to change to the vapour phase.

Cavitation progresses in two stages: incipient and flow-limiting cavitation. Incipient cavitation occurs in the shear layer between the primary and secondary flows. The shear layer generates vortices with very low localized static pressures in which vapour bubbles form. Further downstream, the coherency of the ring vortices reduces and energy is transferred from the jet to the secondary fluid. These processes raise the local and ambient static pressures, causing the bubbles to collapse and generate a detectable sound. A jet pump with incipient cavitation still behaves as predicted by conventional theory.

As the cavitation becomes more intense, flow-limiting cavitation may develop. This occurs when the vapour bubbles increase in number such that they reach the pump walls and completely block the mixing region. At this point, no further entrainment may occur; any further increase in the primary flow has no effect on the secondary flow, and the flow ratio reaches a maximum.

During the experimental program, incipient cavitation was observed to occur under most conditions, but at no time was flow-limiting cavitation observed. The incipient cavitation appeared visually as a white plume emanating from the nozzles. The appearance of the plume coincided with an increased level of audible white noise from the model. Both these observations are consistent with the onset of incipient cavitation as reported by others. The observations were similar for all the tests, with very few or no cavitation bubbles observed at 344 kPa (50 psi) jet inlet pressure, and a steady increase in the visible and audible intensity as the inlet pressure was increased. The jet plume was clearly visible at the maximum jet inlet pressure for all tests.

High-speed images were captured of the cavitation bubbles, and one of these images is shown in Figure 5.15. The model configuration for this image used two nozzles for an area ratio $R = 0.018$, and a jet inlet pressure $P_0 =$ 689 kPa (100 psi). This configuration is similar to Test Number 1, with the exception that the nozzles were positioned adjacent to the window to improve the view for photography.

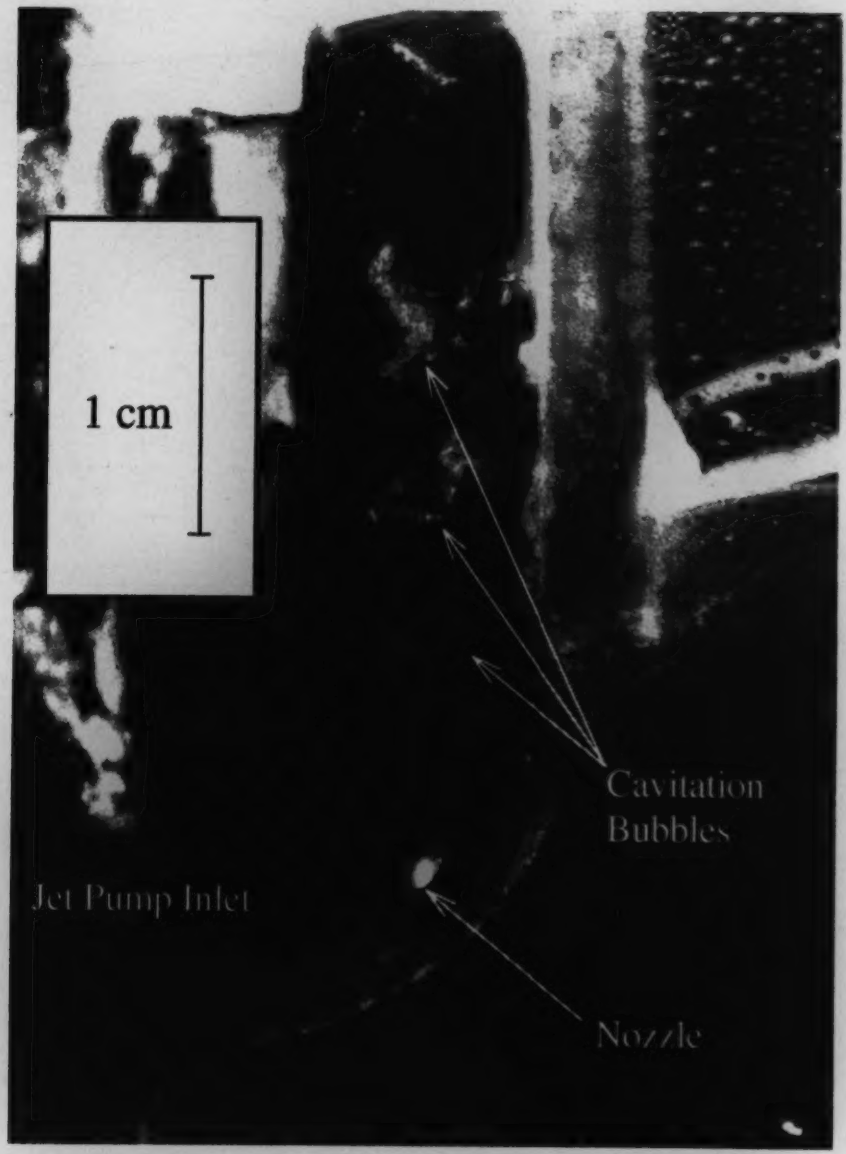

Figure 5.15: Incipient cavitation in the jet pump mixing region. $R = 0.018$, $N_j = 2$, and $P_0 = 689$ kPa (100 psi). The bubbles appear to form a general ring shape, suggesting cavitation in the jet ring vortices.

This image confirms that only incipient cavitation is occurring, since the bubbles are sparse and do not form a dense cloud which fills the mixing region. It also shows that most of the bubbles occur between 0.6 and 3.5 cm from the nozzle tip, which corresponds to 0.5 D_{eff} upstream of the throat to about 2 D_{eff} downstream. This is the region shown in Figure 5.11 where the static pressure drops sharply before energy transfer from the jet starts to raise the pressure. The bubbles in the image appear generally ring shaped, suggesting that they may form in the ring vortices in the jet.

Something else visible in Figure 5.15 is the appearance of cavitation bubbles at the nozzle tip on the lee side of the nozzle (the right side as viewed in the image), and the absence of bubbles on the upstream side (the left side in the image). Photographs published by Sanger (1970) and Narui and Inagaki (1982) show incipient cavitation bubbles forming uniformly around the entire circumference of the nozzle tip. The absence of bubbles on the upstream side of the nozzles was observed during most experimental tests. This might be the result of interactions between the jet shear layer and the boundary layer on the lower surface of the jet pump inlet. On the upstream side of the nozzle, the vortices in these two layers may interact and partially cancel each other, delaying the appearance of cavitation bubbles on that side of the jet.

A method for predicting the onset of flow-limiting cavitation was proposed by Cunningham et al. (1970). The onset of flow-limiting cavitation is

predicted by the cavitation number σ, defined as follows:

$$\sigma = \frac{(P_7 - P_v)}{(\rho U_t^2)/2} \tag{5.1}$$

where P_7 is the ambient static water pressure at the jet pump inlet, P_v is the vapour pressure of the water, ρ is the water density, and U_t is the secondary flow velocity at the throat. Cunningham recommended that, to avoid flow-limiting cavitation, a centre jet pump must operate at σ greater than a critical σ_L.

The value of σ_L varies with the design details of the jet pump, particularly its inlet and nozzle shape, and has been reported to range from 0.80 to about 1.7. In the absence of pump-specific test data, a value of $\sigma_L = 1.35$ is recommended (Cunningham et al., 1970).

The values of σ were calculated for each of the experimental test points, and were found to range from 12.6 at the higher values of R and P_0, to 87.0 at the lowest values of R and P_0. This range is much higher than the recommended limit of 1.35, suggesting that the experimental jet pump did not approach the conditions for flow-limiting cavitation.

It has been observed that cavitation limits the maximum flow ratio which can be achieved by a jet pump. Cunningham et al. (1970) provided a function for predicting the maximum flow ratio of a centre jet pump, based on the

area ratio and σ_L:

$$M_L = \frac{1-R}{R}\left[\frac{P_7 - P_v}{\sigma_L Z}\right]^{\frac{1}{2}} \tag{5.2}$$

where $Z = \rho U_n^2/2$, the nozzle dynamic pressure.

The values of M_L were calculated for each of the experimental test points. These were normalized by dividing the actual flow ratio M by M_L. Assuming that Equation 5.2 is appropriate for the annular mixing jet pump, the resulting number estimates the fraction of the cavitation-limited flow ratio which was achieved by the pump, and hence an indication of the cavitation margin which remained during the test. The normalized values fell in the range of 10% at the lowest values of R and P_0, to 23% at the highest values of R and P_0. These values indicate that the jet pump operated at a wide margin from flow-limiting cavitation, and that the secondary flow rate would have to increase by as much as an order of magnitude before flow-limiting cavitation would likely occur.

It was noted by Cunningham et al. (1970) that the cavitation resistance of a jet pump improves as the area ratio is lowered; this is also shown in Equation 5.2, in which the maximum flow ratio increases as the area ratio decreases. The annular mixing jet pump can be built easily with very low area ratios, because the annulus offers a potentially large area, and the annulus gap leaves space for only small nozzles. This gives the annular mixing jet pump an inherently high cavitation resistance.

5.7 Simulation Error

In the preceding sections, comparisons were shown between the experimental and simulation results. For the key dimensionless performance parameters the flow ratio, head ratio, and efficiency, the relative error of the simulation was calculated using the experimental data as the true values. The error data were calculated using the mean simulation and experiment results for each test group to remove the effect of the nozzle to throat separation, and are presented in Figure 5.16.

From Figure 5.16, it is apparent that the accuracy of the simulation is not high. The error of the simulated flow ratio straddles the zero line, falling within about $\pm$ 15 % of the experimental results. The simulation consistently over-estimated the head ratio, which exceeded the experimental results by ten to thirty percent. The product of these results is the efficiency error, which fell in the range of about five to thirty-five percent.

In Section 4.4.3, the expanded uncertainty of the simulated efficiency was reported to be about 85 %. The actual simulation error for the configurations tested was within about 35 %, less than half of the estimated simulation uncertainty.

5.8 Considerations for Design

An engineering study of the annular mixing jet pump would be incomplete without some comments on their applicability to the design of such pumps.

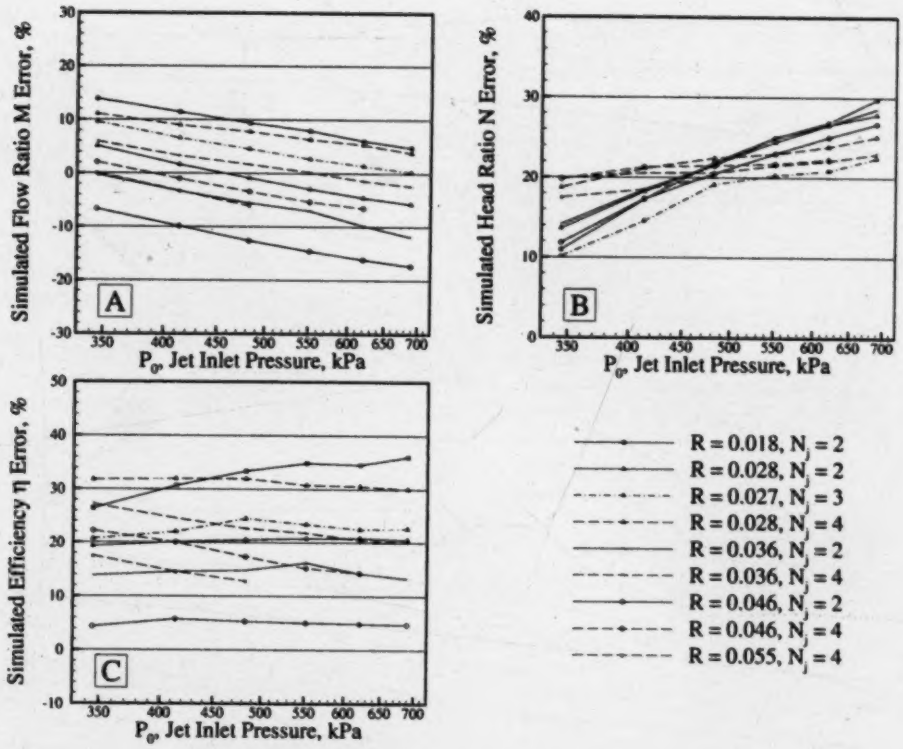
Simulated Flow Ratio M Error, %
A
P0, Jet Inlet Pressure, kPa
Simulated Head Ratio N Error, %
B
P0, Jet Inlet Pressure, kPa
Simulated Efficiency η Error, %
C
P0, Jet Inlet Pressure, kPa
R = 0.018, Nj = 2
R = 0.028, Nj = 2
R = 0.027, Nj = 3
R = 0.028, Nj = 4
R = 0.036, Nj = 2
R = 0.036, Nj = 4
R = 0.046, Nj = 2
R = 0.046, Nj = 4
R = 0.055, Nj = 4

Figure 5.16: The relative error of the simulation results for the flow ratio M, the head ratio N, and efficiency η for all test configurations and jet inlet pressures. The experiment data are taken to be the true values. Data points are the mean values calculated from the five tests within each test group.

In this section, some general comments will be made which may be of use to designers and engineers interested in the application of this style of jet pump.

It should be remembered that the experimental model was only half of the jet pump, cut along its long axis and mounted on a window to allow flow visualization. The following discussion applies to complete annular mixing jet pumps, and will use the number of jets for a complete jet pump. These will, of course, be double the numbers used in the previous sections.

5.8.1 General Discussion

The nozzle to throat distance had only a small effect on the performance of the jet pump. Although the data for each test group were somewhat inconsistent, mean normalized data for the entire test program revealed that all key parameters, with the exception of the mixing length, show a small increase with the nozzle to throat separation distance. Since the maximum separation is limited by the shape of the inlet, it is recommended that jet nozzles be made flush with the lower inlet surface to give maximum pump performance. Additionally, flush nozzles give the shortest mixing length, which allows for the shortest pump length.

The remaining parameters offer performance trade-offs and give the designer the ability to optimize the annular mixing jet pump for a specific application. It was found that as the jet inlet pressure increased, the flow ratio increased and the head ratio decreased. Therefore, if the application

requires a maximum flow ratio, then a higher inlet pressure is necessary, and conversely, if a higher head ratio is needed, a lower jet inlet pressure is required. The jet pump efficiency is not as strongly dependent on the jet inlet pressure as it is on other parameters.

The area ratio allows similar trade-offs to be made to suit an application. A small area ratio will maximize the flow ratio at the expense of the peak mixing pressure and the head ratio, while the opposite is true of larger area ratios. However, the head ratio has a greater response than the flow ratio, so if maximum efficiency is required, a larger area ratio must be used. It is easy to achieve very low area ratios with the annular mixing jet pump, and therefore very high flow ratios should be possible.

Finally, the designer may alter the number of jets to optimize the pump performance. If a compact pump is required, then the mixing length must be minimized. An annular mixing jet pump with eight or more jets will not have recirculation vortices between the jets, and will have the shortest mixing lengths. A large step increase in the mixing length would be experienced with six jets or less.

Related to the mixing length is the peak mixing pressure: a shorter mixing length will give a higher peak pressure because of reduced friction losses. However, the physical orientation of the jet pump must be considered, too. If the pump is installed like the experimental model, with the Q_3 flowing upward, a shorter mixing length would increase the hydrostatic component of P_3 and give a higher peak mixing pressure. However, if Q_3 flows down-

ward, the opposite is true, and if the pump is horizontal, there would be no hydrostatic effects of different mixing lengths.

It should be remembered, though, that the total head at the end of mixing remained independent of the number of jets. If the pump requires a high total discharge head, such as for a lifting application, and the pump size is not important, then four, six, or eight jets could be used with similar success.

The other performance parameters did not exhibit similar step changes with the number of jets, so if size is not an important factor, fewer jets will give the highest flow ratio and efficiency.

The experimental model did not approach flow-limiting cavitation conditions during the experiments, so it remains unknown whether the annular mixing jet pump will have values of σ_L similar to those for centre jet pumps. It was found, however, that lower area ratios and lower jet inlet pressures both contributed to improved cavitation resistance, and the very low area ratios possible for this type of pump make it inherently resistant to cavitation.

Table 5.1 summarizes the general design recommendations. It should be noted that these recommendations are also valid, where applicable, for centre jet pumps. This confirms one of the initial objectives of this research program, which was to verify whether the design techniques for conventional, or centre, jet pumps would apply to the design of the annular mixing jet pump.

Table 5.1: General recommendations for the application and design of annular mixing jet pumps.

Design Goal	Best Value for Parameter			
	Nozzle Length	Jet Inlet Pressure	Area Ratio	Number Of Jets
maximum flow rates	flush	higher	lower	any
maximum peak static pressure	flush	higher	higher	8 or more
maximum flow ratio	flush	higher	lower	fewer
maximum head ratio	flush	lower	higher	any
maximum jet pump efficiency	flush	any	higher	fewer
most compact size	flush	any	any	8 or more
best cavitation resistance	flush	lower	lower	unknown

5.8.2 Use of the Simulation

Two of the objectives of this research were to determine whether conventional design methods were applicable to the annular mixing jet pump, and if so, to develop a method of designing a family of similar pumps. It was expected at the outset of this program that a computer simulation could be a valuable design tool, and that although it may not have high accuracy, it should correctly predict the relative performance of competing designs.

Apart from the effect of the number of jets, the simulation did calculate the correct trends. For the ranges of values tested, the simulation predicted the flow ratio to within ± 15 %, which in many cases may be an adequate design estimate. The error of the head ratio and efficiency calculations is much greater, and should not be relied upon.

With these capabilities and limitations in mind, a designer could use the simulation to generate initial designs, but would have to use a combination of simulation, experiment, and experienced judgement to fully optimize the design.

Several recommendations may be offered to designers intending to use simulation to design an annular mixing jet pump. First, review Table 5.1 for some general guidelines. Of particular note are the nozzle length, or nozzle to throat separation, and the number of jets, since these two parameters are not accurately modeled by the simulation. Once these two parameters are set, the simulation may be used to alter such parameters as the pump dimensions, input pressures, and fluid and environmental properties. From the simulation will come an indication of the relative performance of the designs.

Once the best design is selected, the actual performance must be determined. If the design goal involves flow rates or the flow ratio, the simulation may prove sufficiently accurate. However, if pressures, the head ratio, or efficiency are critical, the simulation results should not be relied upon, and experiments should be conducted to validate the design.

CHAPTER 6

SUMMARY AND CONCLUSIONS

6.1 Introduction

A new type of jet pump called the annular mixing jet pump was investigated. This type of pump uses multiple jets flowing into the annulus formed between two concentric pipes, with the jets flowing parallel to the pipes. Its first reported use was in the mid-1980s (Field, 1990), and given that jet pumps were first described in the mid-eighteenth century (Thomson, 1852), the annular mixing jet pump is a relatively new design.

A physical model of the annular mixing jet pump was constructed to evaluate its performance and operating characteristics. The model was built as half of a jet pump, sectioned along its long axis and mounted onto a window to allow flow visualization inside the pump. By varying four design parameters, 45 different physical configurations were tested. The first parameter was the nozzle to throat separation, which is the distance from the nozzle tip to the throat, and which varied from zero to 0.76 effective throat diameters.

The second parameter was the area ratio, defined as the ratio of the total cross-sectional flow area of the jet nozzles to the cross-sectional flow area at the throat. The area ratio varied from 0.018 to 0.055. The third parameter was the number of jets, of which two, three, or four were used. The last parameter was the static gauge pressure at the inlet to the jet nozzles, which ranged from 345 kPa (50 psi) to a maximum of 689 kPa (100 psi).

A computer simulation of the experimental model was also built, using the one-dimensional energy equation as its basis. The simulation used conventional energy loss models for wall friction, elbows, expansions and contractions, and mixing. Hydraulic and effective diameters were used when modelling non-circular flow channels. The simulation was written to determine whether these models could be applied to design an annular mixing jet pump, and if so, to develop a useful design tool for similar pumps.

The performance of the jet pump was expressed with three dimensionless parameters. The flow ratio is the ratio of the secondary flow rate to the primary flow rate. Next, the head ratio is a ratio of changes to the total head, with the head difference between the jet pump inlet and the end of the mixing region in the numerator, and the head difference between the end of the mixing region and the jet inlet in the denominator. The final parameter is the jet pump efficiency, which is the product of the flow and head ratios.

6.2 Conclusions from the Experiments

It was found that all the performance indicators of the annular mixing jet pump, including the flow rates, head and flow ratios and efficiency, improved as the nozzle to throat separation increased. This effect is similar to that observed for centre jet pumps. For maximum pump performance, it is recommended that the nozzle to throat separation be maximized by making the jets flush with the lower surface of the jet pump inlet. The maximum nozzle to throat separation of the experimental model was 0.76 effective diameters, corresponding to a flush jet, and this value is recommended as a minimum. The literature for centre jet pumps suggests the optimum value may be greater (Cairns and Na, 1969), but this could not be confirmed with the experimental model as it was built.

As expected, the flow rates and pressures within the annular mixing jet pump increased with the jet inlet pressure. The mixing length, defined as the distance from the throat to the point where the mixing chamber pressure reaches its maximum, was independent of the jet inlet pressure. The flow ratio increased and the head ratio decreased as the jet inlet pressure rose. Therefore, a designer seeking maximum flow ratios should use higher jet inlet pressures, while a design to maximize the head ratio should aim for lower inlet pressures. The efficiency showed a dependency on the number of jets in addition to the jet inlet pressure: for two jets, the efficiency was independent of the jet inlet pressure, but for four jets, the efficiency increased with the jet inlet pressure.

Like centre jet pumps, increasing the area ratio of the annular mixing jet pump resulted in higher flow rates and static mixing region pressures. However, it was found that the area ratio had no effect on the mixing length. As the area ratio increased, the flow ratio decreased and the head ratio rose. The area ratio had a stronger effect on the head ratio than on the flow ratio, and since the efficiency is the product of the head and flow ratios, the efficiency increased with the area ratio.

The number of jets had a significant effect on the flow structure in the mixing region. The experimental model had a mixing length of 11 effective diameters when four jets were installed, which is longer than the typical range of 5.6 to 10 diameters for a centre jet pump. This may be attributed to the distance the jets must spread to meet and mix with adjacent jets. With two or three jets, mixing was complete after 20 effective diameters. It is proposed that the longer mixing length coincided with the appearance of a recirculation region between the jets, located between two and five effective diameters downstream of the throat. This conclusion is based on evidence found in the static pressure measurements within the mixing region, from flow visualization imagery, and from the observations of other researchers studying centre (Hill, 1965; Rajaratnam, 1976) and annular jet pumps (Elger et al., 1994).

The flow ratio showed a decrease as the number of jets increased, while the head ratio remained constant. Therefore, the efficiency of the jet pump fell as the number of jets increased.

The recommended number of jets depends on the application of the jet pump. If the flow ratio or efficiency must be maximized, then fewer jets should be used. However, if a compact size is required, the mixing length must be minimized, and more jets are needed. In the experimental model, the mixing length dropped from 20 down to 11 effective diameters when the number of jets increased from three to four. Assuming a complete jet pump to have similar mixing characteristics as the half-sectioned experimental model, at least eight jets would be needed to minimize the size of an annular mixing jet pump.

Flow-limiting cavitation did not occur during any of the test runs, although some degree of incipient cavitation was observed for most tests. Flow visualization imagery gave the impression that the observed cavitation occurred in the jet vortices. Calculations of Cunningham's cavitation index σ (Cunningham et al., 1970) suggested that the experimental model operated at a wide margin from the onset of flow-limiting cavitation. The annular mixing jet pump can be easily built with very low area ratios, and since cavitation resistance increases as the area ratio drops, the annular mixing jet pump can be made very resistant to cavitation.

Assuming, as contended here, that the results and conclusions for the half-sectioned experimental model are applicable to a complete annular mixing jet pump, some general recommendations can be offered to designers. These are summarized in Table 6.1

Table 6.1: General recommendations for the application and design of complete annular mixing jet pumps.

Design Goal	Best Value for Parameter			
	Nozzle Length	Jet Inlet Pressure	Area Ratio	Number Of Jets
maximum flow rates	flush	higher	lower	any
maximum peak static pressure	flush	higher	higher	8 or more
maximum flow ratio	flush	higher	lower	fewer
maximum head ratio	flush	lower	higher	any
maximum jet pump efficiency	flush	any	higher	fewer
most compact size	flush	any	any	8 or more
best cavitation resistance	flush	lower	lower	unknown

6.3 Conclusions from the Simulation

It was found that the annular mixing jet pump can be analyzed with a simple one-dimensional simulation. This simulation correctly predicted the effects of the jet inlet pressure and the area ratio. Like the published results for centre jet pumps, incipient cavitation had no effect on the validity of the simulation.

It is recommended that the elbow loss model published by The Crane Company (1976) and the mixing loss model proposed by Cunningham (1957) be used. The loss models for expansions and contractions published by The Hydraulic Institute (1954) and modified for round edge inlets as proposed by Bullen et al. (1988) are also recommended. The use of effective diameters for non-circular flow channels in the jet pump inlet and annulus worked well.

The one-dimensional simulation did not correctly predict the effects of the number of jets, because such effects arise from the three-dimensional flow patterns in the mixing chamber. Therefore, to use a one-dimensional simulation to design an annular mixing jet pump, the designer must first apply the general rules outlined in Table 6.1 to select an appropriate number of jets. Once this selection has been made, a simulation may be used, altering the remaining design variables to obtain an optimal design.

Although it was expected and confirmed that a simple one-dimensional simulation would not have a high accuracy, it did correctly predict the general performance trends within the limits of the experimental program. For the ranges of conditions tested, the simulation gave flow ratio results within $\pm$ 15 % of the experiments, but the error in the efficiency was much greater, ranging up to about 35 %. Despite its shortcomings, this type of simulation, when combined with the guidelines in Table 6.1, should allow a designer to optimize an annular mixing jet pump for a particular application.

6.4 Recommendations for Future Work

This is the first study of the annular mixing jet pump, so there remain many avenues for research with this type of pump.

The jet pump used for this study was a half-sectioned model. This allowed flow visualization, but introduced wall effects which would not be present in a real pump. It is suggested that future work be done with a complete model of the jet pump. Such a model could be made with transparent pipes to allow visualization within the mixing region.

One application of the annular mixing jet pump is for cleaning particles in a water conditioner. This application has two-phase secondary and tertiary flows, and further study of multiphase flows in this type of jet pump would be of interest.

The effects of the nozzle to throat separation were explored over a limited range. It would be useful to know if an optimum value exists for the nozzle to throat separation, as is the case for centre jet pumps.

The recirculation region found in the mixing region had a pronounced effect on the size of the jet pump, and a greater understanding of the geometries and conditions which produce recirculation would be of interest. The use of advanced flow visualization techniques, such as image correlation velocimetry with tracer particles, could be explored.

Another route to explore would be the use of two- or three-dimensional computational fluid dynamics to simulate the jet pump. This approach would be expected to offer improved accuracy and reduced uncertainty of the simulation results. It may also give more insight into the effects of the nozzle to throat separation and the number of jets, two parameters the simple one-dimensional approach did not adequately model.

During the test program, the jet pump did not approach the conditions for flow limiting cavitation. The conditions under which flow limiting cavitation may occur would be important for a designer, and more research should be done to quantify these.

BIBLIOGRAPHY

Blevins, R. D. (1992). *Applied Fluid Dynamics Handbook.* Van Nostrand, New York.

Bonnington, S. T. and Hemmings, J. A. G. (1976). *Jet Pumps and Ejectors, A State of the Art Review and Bibliography.* BHRA Fluid Engineering, Cranfield, Bedford, England, 2nd edition.

Bullen, P. R., Cheeseman, D. J., and Hussain, L. A. (1988). The Effects of Inlet Sharpness on the Pipe Contraction Pressure Loss Coefficient. *Int. J. Heat and Fluid Flow*, 9(4):431–433.

Cairns, J. R. and Na, T. Y. (1969). Optimum Design of Water Jet Pumps. *Trans. ASME, Series A*, 91(1):62–68.

Colebrook, C. F. (1938–1939). Turbulent Flows in Pipes, with Particular Reference to the Transition Between the Smooth and Rough Pipe Laws. *J. Inst. Civil Eng.*, 11:133–156.

Cunningham, R. G. (1957). Jet Pump Theory and Performance With Fluids of High Viscosity. *Trans. ASME*, 79:1807–1820.

Cunningham, R. G. (1975). Liquid Jet Pump Modelling: Effects of Axial Dimensions on Theory-Experiment Agreement. In *2nd Symposium on Jet Pumps and Ejectors and Gas Lift Techniques*, pages F1–1 to F1–15.

Cunningham, R. G., Hansen, A. G., and Na, T. Y. (1970). Jet Pump Cavitation. *Trans. ASME, J. Basic Eng.*, 92(3):483–494.

Elger, D. F., Taylor, S. J., and Liou, C. P. (1994). Recirculation in an Annular-Type Jet Pump. *Trans. ASME, J. Fluids Eng.*, 116:735–740.

Field, R. G. (1990). Water Conditioner Backflush Device. Patent #1,273,721, Canadian Intellectual Property Office.

Field, R. G. (1995). Water Conditioner Backflush Device. Patent #5,472,609, United States Patent and Trademark Office.

Fluke Mfg. Co. (1977). *2175A Digital Thermometer Instruction Manual.* John Fluke Mfg. Co., Inc.

Gosline, J. E. and O'Brein, M. P. (1934). The Water Jet Pump. *University of California Publications in Engineering*, 3(3):167–190.

Haaland, S. E. (1983). Simple and Explicit Formulas for the Friction Factor in Turbulent Pipe Flow. *Trans. ASME, J. Fluids Eng.*, 105(1):89–90.

Hill, P. G. (1965). Turbulent Jets in Ducted Streams. *J. Fluid Mech.*, 22:161–186.

Jaluria, Y. (1988). *Computer Methods for Engineering.* Allyn and Bacon.

Johnson, R. D. (1968). Method and Means for Backwashing Mineral Beds. Patent #3,395,095, United States Patent and Trademark Office.

Jones, Jr., O. C. (1976). An Improvement in the Calculations of Turbulent Friction in Rectangular Ducts. *Trans. ASME, J. Fluids Eng.*, 98:173–181.

Jones, Jr., O. C. and Leung, J. C. M. (1981). An Improvement in the Calculations of Turbulent Friction in Smooth Concentric Annuli. *Trans. ASME, J. Fluids Eng.*, 103(4):615–623.

Lewis, R. A. (1965). An Experimental Analysis of a Jet Inducer With Multiple Nozzles. In *Symposium on Cavitation in Fluid Machinery, ASME Annual Meeting*, page 109.

Matthews, B. H. (1959). Method of Regenerating a Zeolite Bed. Patent #2,902,445, United States Patent and Trademark Office.

Miller, I. and Freund, J. E. (1985). *Probability and Statistics for Engineers.* Prentice-Hall, Englewood Cliffs, New Jersey, 3rd edition.

Moody, L. F. (1944). Friction Factors for Pipe Flow. *ASME Trans.*, 66:671–684.

Narui, H. and Inagaki, S. (1982). Limiting Flow Cavitation Number of Water Jet Pumps. *Bull. JSME*, 25(209):1682–1689.

Purdy, A. W. (1967). The Country of the Young. In *North of Summer*, pages 79–80. McClelland and Stewart, Toronto.

Rajaratnam, N. (1976). *Turbulent Jets.* Elsevier Scientific Publishing Company, Amsterdam.

Rakitin, S. R. (1997). *Software Verificatin and Validation: A Practitioner's Guide.* Artech House, Boston.

Rankine, J. M. (1870). On the Mathematical Theory of Combined Streams. *Proc. Royal Soc.*, 19:90–94.

Robinson, M. P. (1944). Water Treating Apparatus. Patent #2,365,293, United States Patent and Trademark Office.

Sanger, N. L. (1970). An Experimental Investigation of Several Low Area Ratio Water Jet Pumps. *Trans. ASME, J. Basic Eng.*, 92:11–20.

Schmitt, H. (1975). Diversity of Jet Pumps and Ejector Techniques. In *2nd Symposium on Jet Pumps and Ejectors and Gas Lift Techniques*, pages A4–35 to A4–49.

Sparrow, E. M., Chen, T. S., and Jonsson, V. K. (1964). Laminar Flow and Pressure Drop in Internally Finned Annular Ducts. *Int. J. Heat and Mass Transfer*, 7:583–585.

Taylor, B. N. and Kuyatt, C. E. (1994). Guidelines for Evaluating and Expressing the Uncertainty of NIST Measurement Results. NIST Technical Note 1297, National Institute of Standards and Technology, Washington, D.C.

The Crane Company (1976). Flow of Fluids Through Valves, Fittings, and Pipe. Technical Paper No. 410-C, Crane Canada Limited.

The Hydraulic Institute (1954). *Pipe Friction Manual.* Hydraulic Institute, New York.

Thomson, J. (1852). On a Jet Pump, or Apparatus for Drawing Up Water by the Power of a Jet. *British Association Report*, pages 130–131.

Validyne Corp. (1971). *Phamphlet CD 15-8/71, Validyne CD15 DC Output Sine Wave Carrier Demodulator.* Validyne Engineering Corporation.

Weast, R. C., editor (1982). *CRC Handbook of Chemistry and Physics.* CRC Press, Boca Raton, Florida, 63rd edition.

White, F. M. (1986). *Fluid Mechanics.* McGraw-Hill, 2nd edition.

APPENDIX A

SIMULATION UNCERTAINTY PARAMETERS

The following 44 parameters were used to estimate the uncertainty of the simulation results. The table lists all the parameter symbols, descriptions, and the estimated uncertainty limits.

Table A.1: Parameters Contributing to Simulation Uncertainty

Symbol	Parameter Description	Uncertainty
Pipe dimensions:		
D_b	outside diameter of inner pipe	± 0.025 cm
t_b	wall thickness of inner pipe	± 0.020 cm
D_d	outside diameter of outer pipe	± 0.025 cm
t_d	wall thickness of outer pipe	± 0.020 cm
D_{125}	inside diameter of 31mm ($1\frac{1}{4}$") pipe	± 0.028 cm
D_{200}	inside diameter of 51mm (2") pipe	± 0.030 cm

continued on next page...

continued from previous page...

Symbol	Parameter Description	Uncertainty
L_{125}	length of 31mm pipe	± 0.3 cm
L_{200}	length of 51mm pipe	± 0.3 cm
Other dimensions and parameters:		
P_0	jet nozzle inlet pressure	± 3.5 kPa
T_w	water temperature	± 0.9°C
H_w	water surface height above z_{4a}	± 0.2 cm
D_j	jet nozzle diameter	± 0.0025 cm
h_i	jet pump inlet height	± 0.051 cm
r_i	jet pump inlet radius	± 0.025 cm
r_j	jet nozzle inlet radius	± 0.025 cm
r_5	discharge pipe inlet radius	± 0.025 cm
D_{1a}	inlet plenum core diameter	± 0.013 cm
D_{1b}	inlet plenum major diameter	± 0.013 cm
α	kinetic energy correction factor	± 0.020
L_{mix}	mixing length	± 2 $D_{eff,3}$
Elevations:		
z_0	inlet pressure gauge elevation	± 0.1 cm
z_1	jet nozzle inlet plane elevation	± 0.1 cm
z_2	jet nozzle exit plane elevation	± 0.1 cm
z_4	pressure tap # 17 elevation	± 0.1 cm

continued on next page...

continued from previous page...

Symbol	Parameter Description	Uncertainty
z_{4a}	annulus discharge plane elevation	± 0.1 cm
z_5	discharge plenum exit plane elevation	± 0.1 cm
z_6	discharge pipe exit plane elevation	± 0.1 cm
z_7	jet pump inlet elevation	± 0.1 cm
Friction factors:		
f_2	jet nozzle friction factor	± 25 %
f_3	annulus friction factor	± 25 %
f_{5a}	31mm pipe friction factor	± 25 %
f_6	51mm pipe friction factor	± 25 %
f_9	jet pump inlet friction factor	± 25 %
Loss coefficients:		
$K_{el,6a}$	31mm pipe elbow loss factor	± 50 %
$K_{el,6b}$	51mm pipe elbow loss factor	± 50 %
$K_{el,8}$	jet pump inlet elbow loss factor	± 50 %
$K_{sc,2}$	sudden contraction into jet nozzles	± 15 %
$K_{sc,6}$	sudden contraction into 31mm pipe	± 15 %
$K_{sc,7}$	sudden contraction into jet pump inlet	± 15 %
$K_{gc,8}$	gradual contraction in jet pump inlet	± 15 %
$K_{se,5}$	sudden expansion into discharge plenum	± 15 %
$K_{ge,6}$	gradual expansion at pipe connector	± 15 %

continued on next page...

continued from previous page...

Symbol	Parameter Description	Uncertainty
K_{mix}	mixing loss coefficient	$\pm$ 15 %
K_{Ann}	Annubar permanent loss coefficient	$\pm$ 15 %

Appendix B

Experiment and Simulation Data

This appendix contains details of the experiment configurations, and plots of the experimental and simulation results.

Table B.1: Experimental Test Schedule

Test Group	Test Numbers	N_j	D_j, cm	R
1	1 – 5	2	0.373	0.0180
2	6 – 10	2	0.462	0.0276
3	11 – 15	3	0.373	0.0271
4	16 – 20	4	0.326	0.0276
5	21 – 25	2	0.531	0.0365
6	26 – 30	4	0.373	0.0361
7	31 – 35	2	0.595	0.0459
8	36 – 40	4	0.422	0.0460
9	41 – 45	4	0.462	0.0553

Table B.2: Nozzle to Throat Distances

Test Number Within Group	s/D_{eff}
first	0.76
second	0.57
third	0.38
fourth	0.19
fifth	0.00
$D_{eff} = 1.49$ cm	

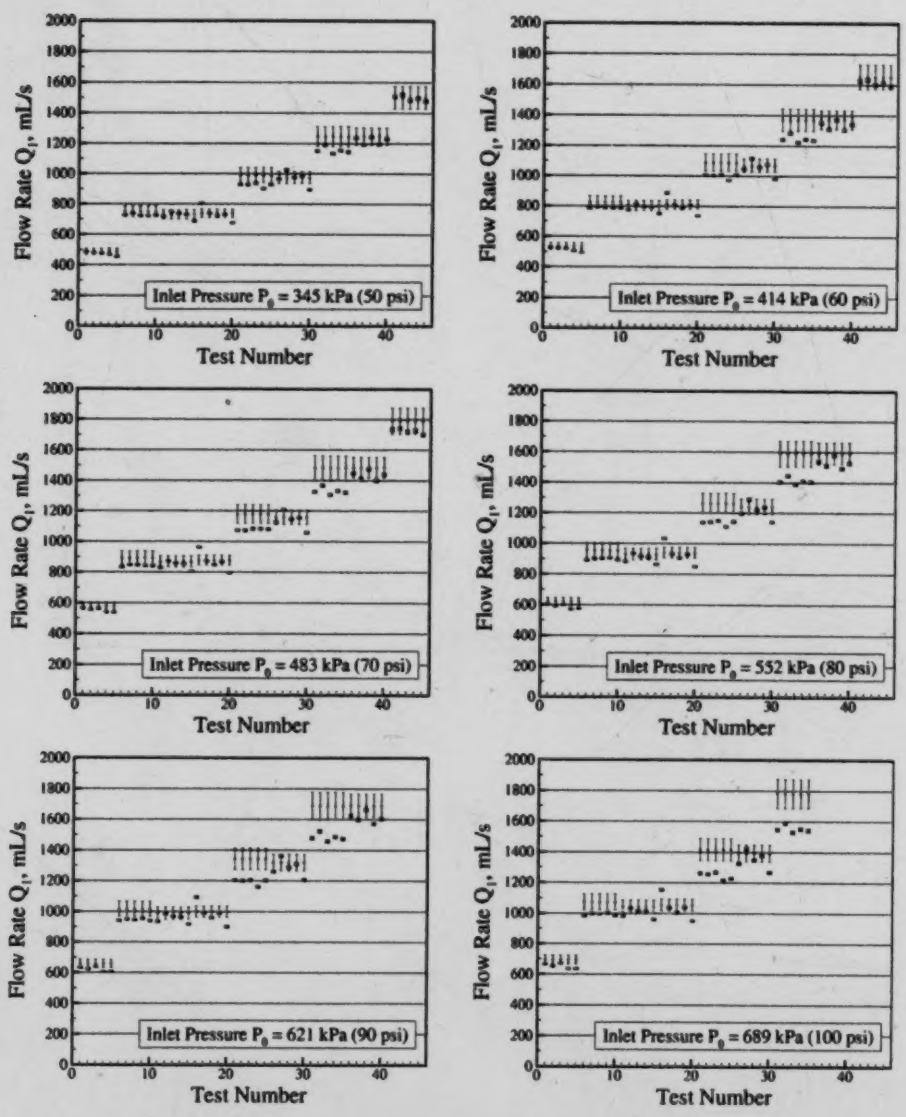
Flow Rate Q_1, mL/s
Test Number
Inlet Pressure P_0 = 345 kPa (50 psi)
Inlet Pressure P_0 = 414 kPa (60 psi)
Inlet Pressure P_0 = 483 kPa (70 psi)
Inlet Pressure P_0 = 552 kPa (80 psi)
Inlet Pressure P_0 = 621 kPa (90 psi)
Inlet Pressure P_0 = 689 kPa (100 psi)

Figure B.1: Data for the volumetric flow rate Q_1 obtained from the experiments (short error bars) and the simulation (tall error bars) for all test points and jet inlet plenum pressures. The nominal simulation result is shown with a horizontal tic mark in the middle of the large error bar.

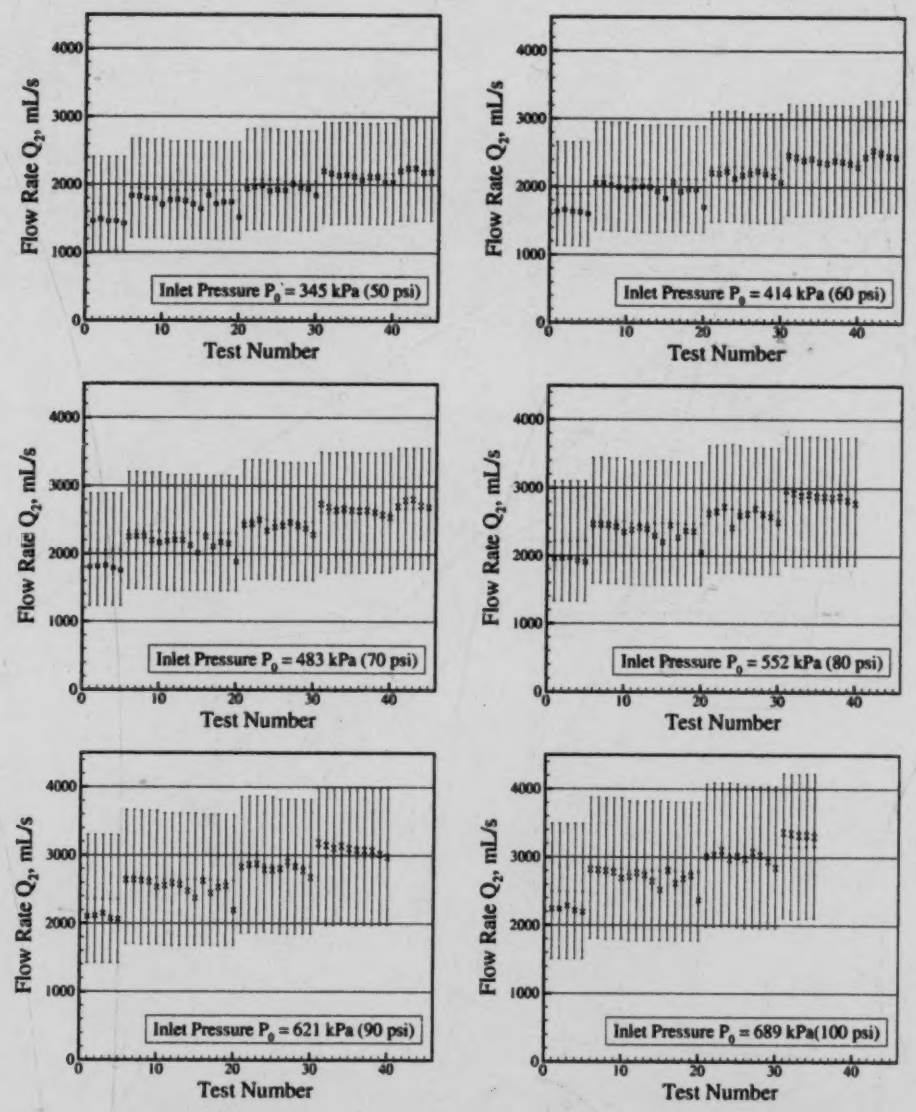
Flow Rate Q_2, mL/s
Test Number
Inlet Pressure P_0 = 345 kPa (50 psi)
Inlet Pressure P_0 = 414 kPa (60 psi)
Inlet Pressure P_0 = 483 kPa (70 psi)
Inlet Pressure P_0 = 552 kPa (80 psi)
Inlet Pressure P_0 = 621 kPa (90 psi)
Inlet Pressure P_0 = 689 kPa(100 psi)

Figure B.2: Data for the volumetric flow rate Q_2 obtained from the experiments (short error bars) and the simulation (tall error bars) for all test points and jet inlet plenum pressures. The nominal simulation result is shown with a horizontal tic mark in the middle of the large error bar.

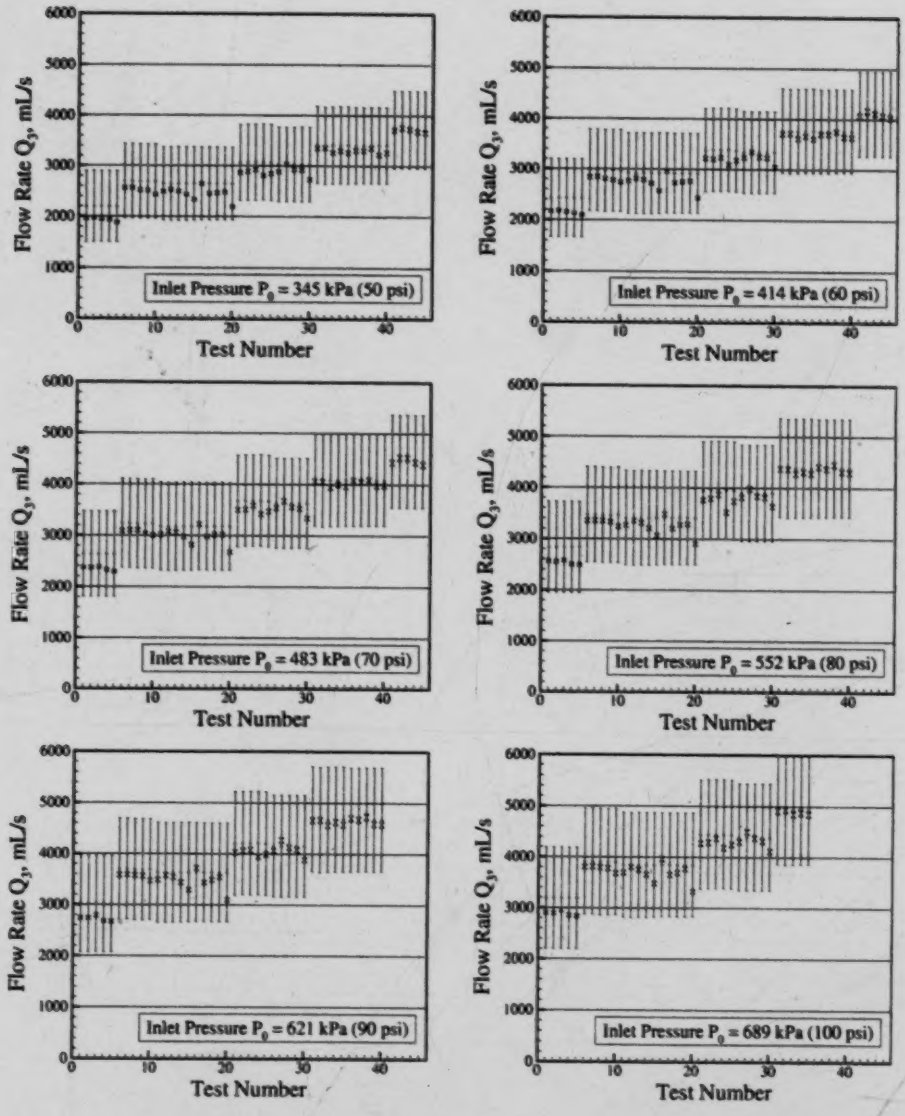
Flow Rate Q_3, mL/s
Test Number
Inlet Pressure P_0 = 345 kPa (50 psi)
Inlet Pressure P_0 = 414 kPa (60 psi)
Inlet Pressure P_0 = 483 kPa (70 psi)
Inlet Pressure P_0 = 552 kPa (80 psi)
Inlet Pressure P_0 = 621 kPa (90 psi)
Inlet Pressure P_0 = 689 kPa (100 psi)

Figure B.3: Data for the volumetric flow rate Q_3 obtained from the experiments (short error bars) and the simulation (tall error bars) for all test points and jet inlet plenum pressures. The nominal simulation result is shown with a horizontal tic mark in the middle of the large error bar.

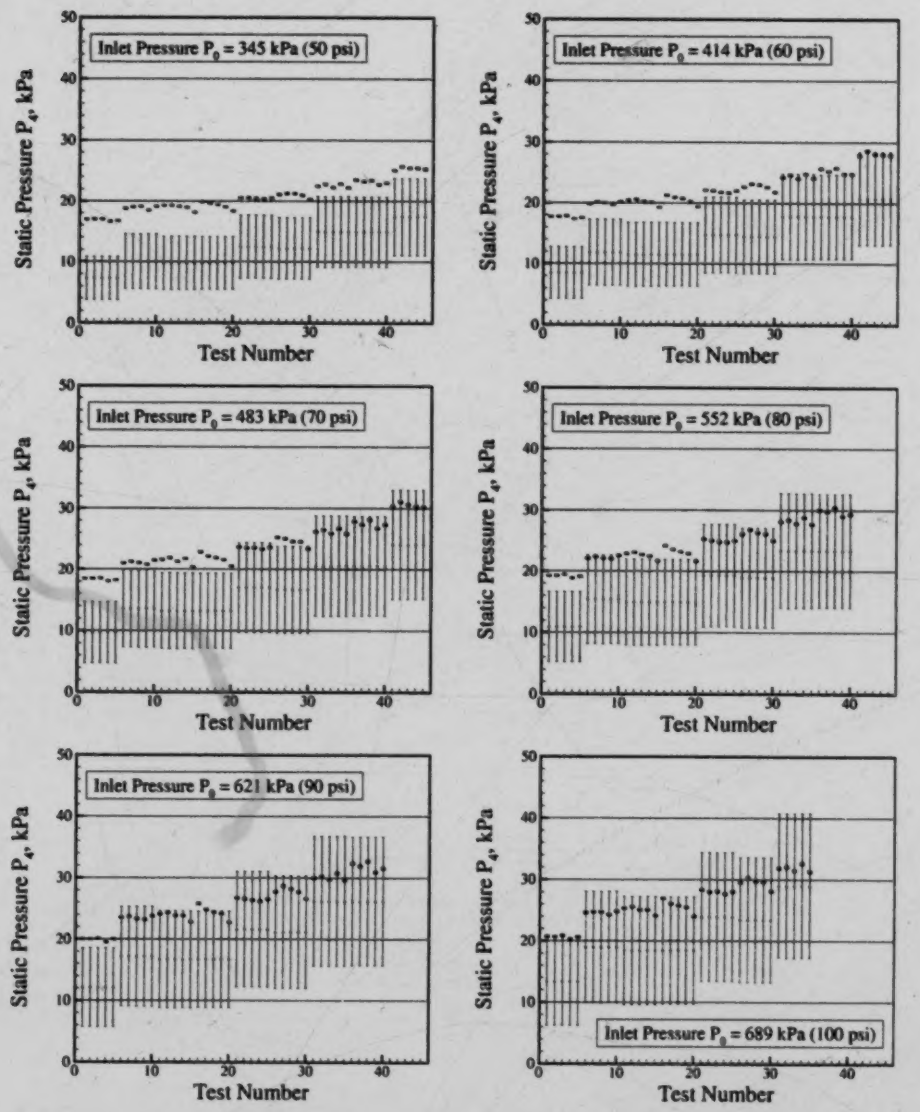
Inlet Pressure P0 = 345 kPa (50 psi)
Inlet Pressure P0 = 414 kPa (60 psi)
Inlet Pressure P0 = 483 kPa (70 psi)
Inlet Pressure P0 = 552 kPa (80 psi)
Inlet Pressure P0 = 621 kPa (90 psi)
Inlet Pressure P0 = 689 kPa (100 psi)
Static Pressure P4, kPa
Test Number
0
10
20
30
40
50

Figure B.4: Data for the static annulus discharge pressure P_4 obtained from the experiments (short error bars) and the simulation (tall error bars) for all test points and jet inlet plenum pressures. The nominal simulation result is shown with a horizontal tic mark in the middle of the large error bar.

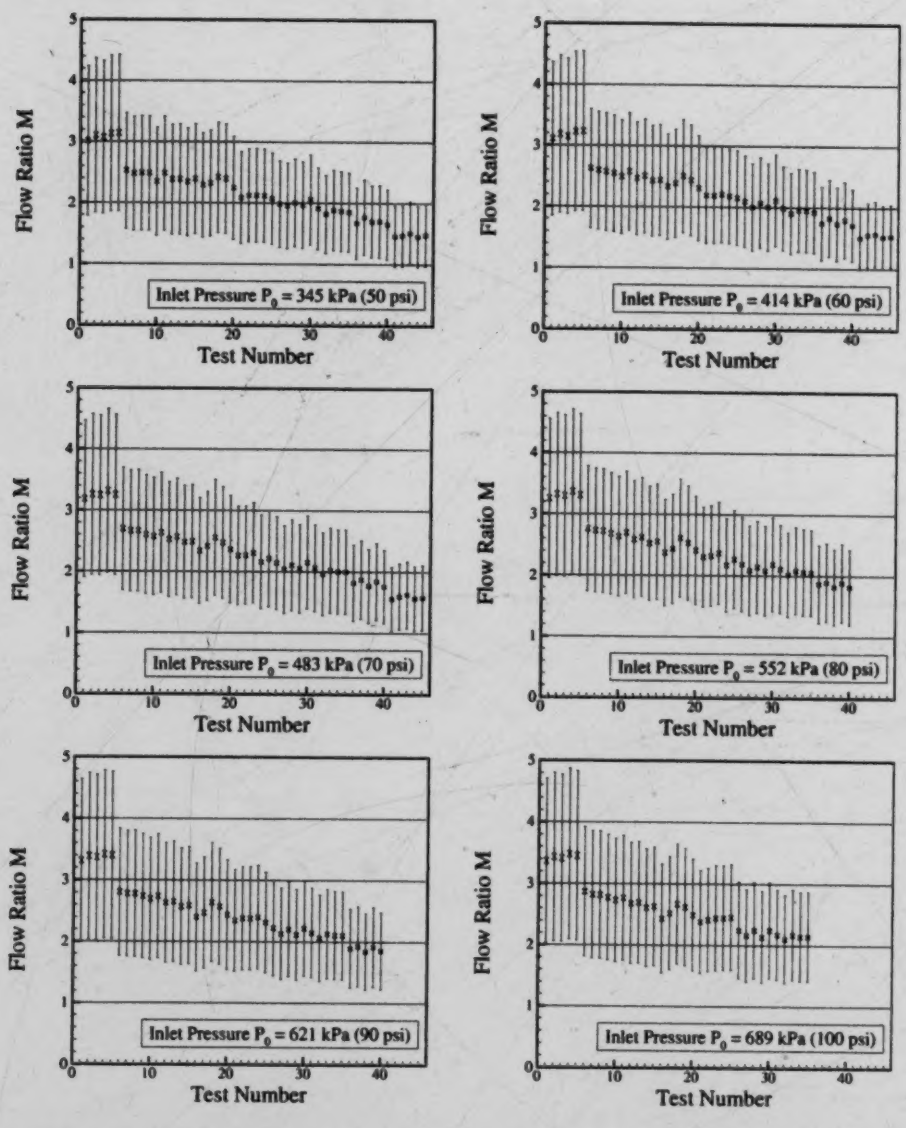
Flow Ratio M
Test Number
Inlet Pressure P0 = 345 kPa (50 psi)
Inlet Pressure P0 = 414 kPa (60 psi)
Inlet Pressure P0 = 483 kPa (70 psi)
Inlet Pressure P0 = 552 kPa (80 psi)
Inlet Pressure P0 = 621 kPa (90 psi)
Inlet Pressure P0 = 689 kPa (100 psi)

Figure B.5: Data for the flow ratio $M = Q_2/Q_1$ obtained from the experiments (short error bars) and the simulation (tall error bars) for all test points and jet inlet plenum pressures. The nominal simulation result is shown with a horizontal tic mark in the middle of the large error bar.

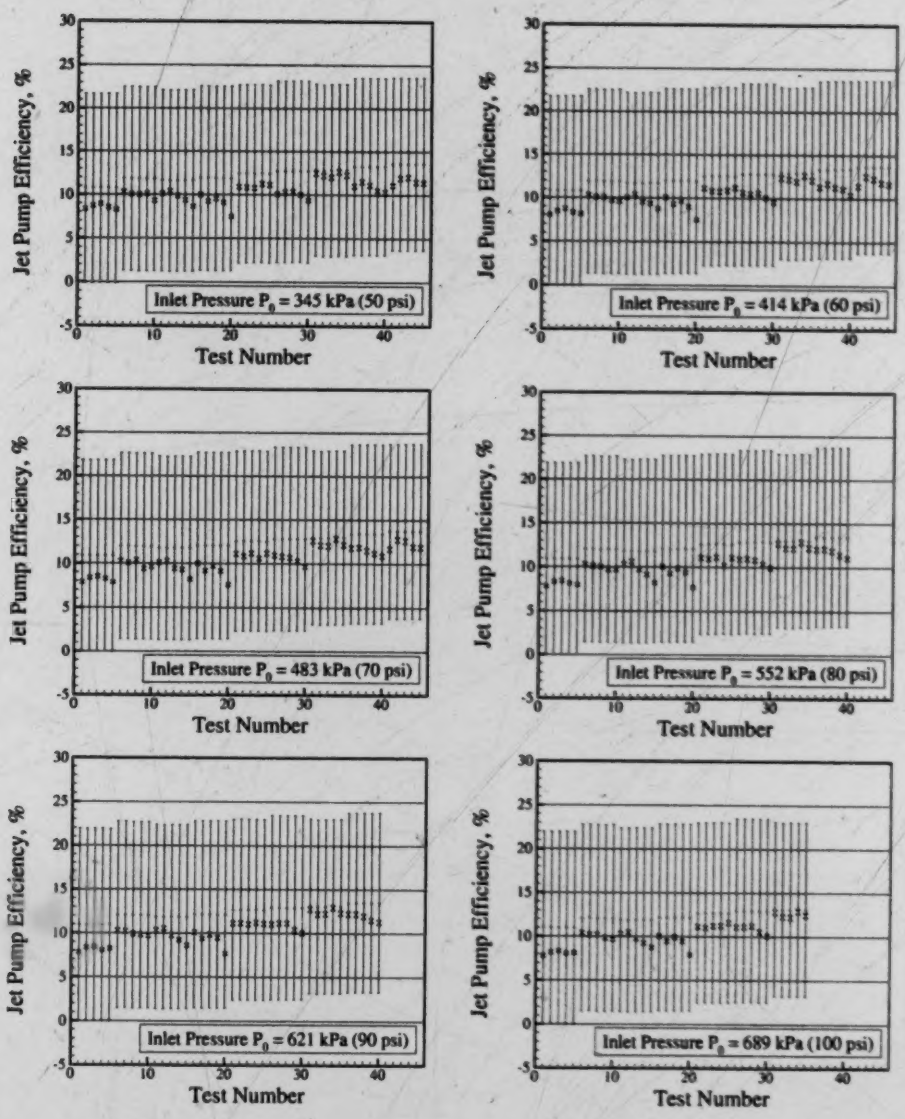
Jet Pump Efficiency, %
Test Number
Inlet Pressure P0 = 345 kPa (50 psi)
Inlet Pressure P0 = 414 kPa (60 psi)
Inlet Pressure P0 = 483 kPa (70 psi)
Inlet Pressure P0 = 552 kPa (80 psi)
Inlet Pressure P0 = 621 kPa (90 psi)
Inlet Pressure P0 = 689 kPa (100 psi)

Figure B.6: Data for the jet pump efficiency η obtained from the experiments (short error bars) and the simulation (tall error bars) for all test points and jet inlet plenum pressures. The nominal simulation result is shown with a horizontal tic mark in the middle of the large error bar.

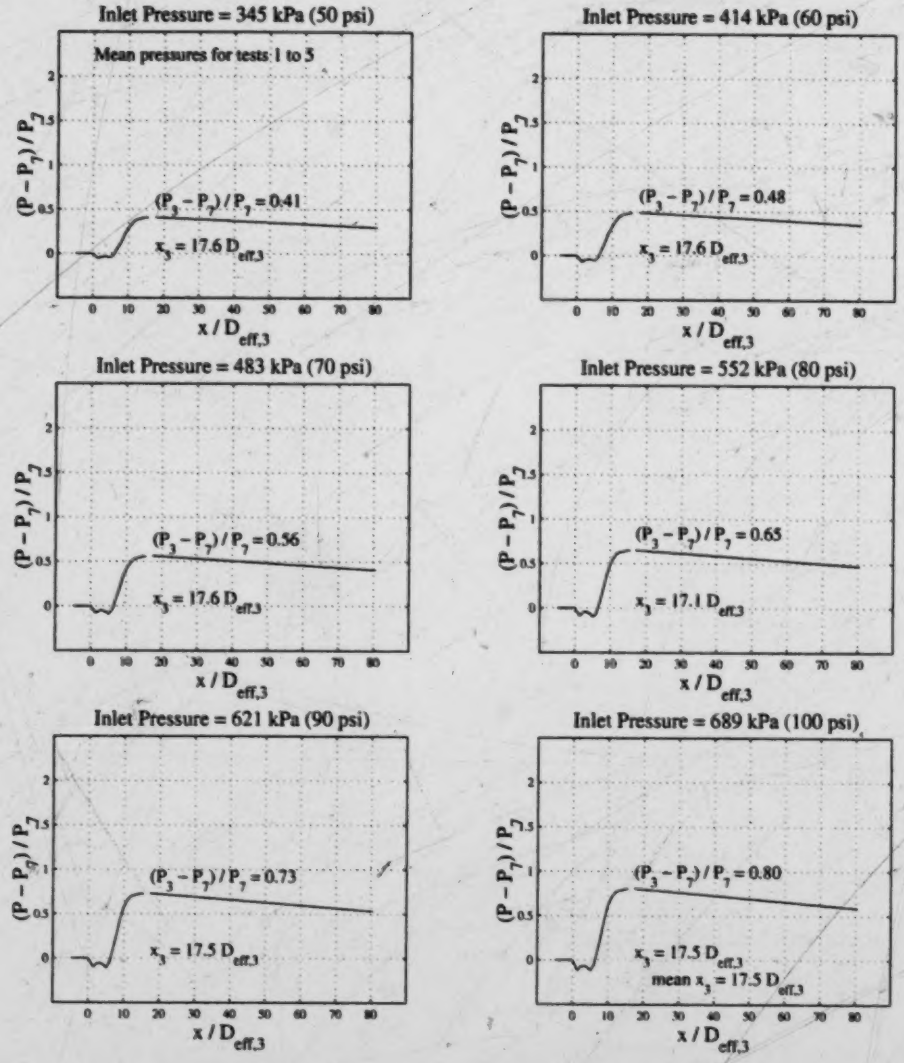
Inlet Pressure = 345 kPa (50 psi)
Mean pressures for tests 1 to 5
(P_3 - P_7) / P_7 = 0.41
x_3 = 17.6 D_eff,3
Inlet Pressure = 414 kPa (60 psi)
(P_3 - P_7) / P_7 = 0.48
x_3 = 17.6 D_eff,3
Inlet Pressure = 483 kPa (70 psi)
(P_3 - P_7) / P_7 = 0.56
x_3 = 17.6 D_eff,3
Inlet Pressure = 552 kPa (80 psi)
(P_3 - P_7) / P_7 = 0.65
x_3 = 17.1 D_eff,3
Inlet Pressure = 621 kPa (90 psi)
(P_3 - P_7) / P_7 = 0.73
x_3 = 17.5 D_eff,3
Inlet Pressure = 689 kPa (100 psi)
(P_3 - P_7) / P_7 = 0.80
x_3 = 17.5 D_eff,3
mean x_3 = 17.5 D_eff,3
(P - P_7) / P_7
x / D_eff,3

Figure B.7: Mean static pressures measured in the mixing region of the jet pump for Test Group 1 (tests 1 through 5). These test configurations had $N_j = 2$ and $R = 0.018$. $P_7 = 13.0$ kPa and $D_{eff,3} = 1.49$ cm.

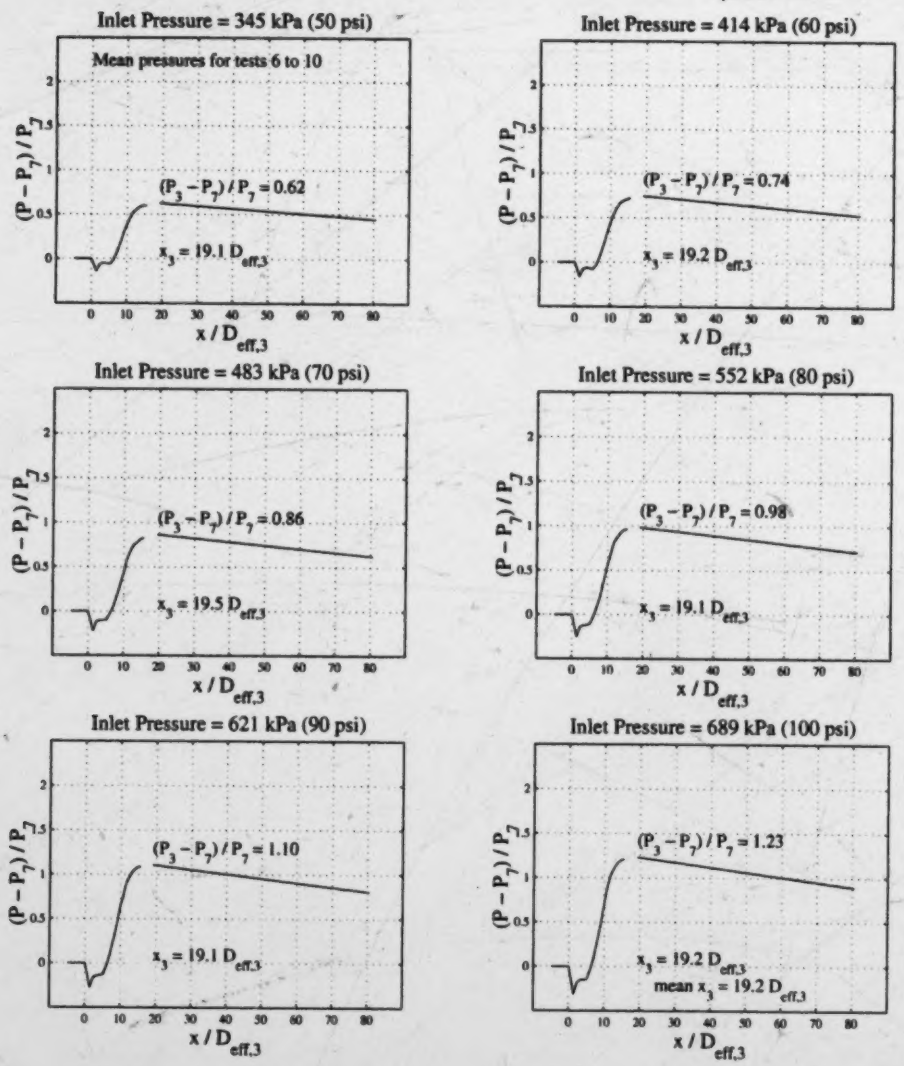
Inlet Pressure = 345 kPa (50 psi)
Mean pressures for tests 6 to 10
(P3 – P7) / P7 = 0.62
x3 = 19.1 Deff,3
Inlet Pressure = 414 kPa (60 psi)
(P3 – P7) / P7 = 0.74
x3 = 19.2 Deff,3
Inlet Pressure = 483 kPa (70 psi)
(P3 – P7) / P7 = 0.86
x3 = 19.5 Deff,3
Inlet Pressure = 552 kPa (80 psi)
(P3 – P7) / P7 = 0.98
x3 = 19.1 Deff,3
Inlet Pressure = 621 kPa (90 psi)
(P3 – P7) / P7 = 1.10
x3 = 19.1 Deff,3
Inlet Pressure = 689 kPa (100 psi)
(P3 – P7) / P7 = 1.23
x3 = 19.2 Deff,3
mean x3 = 19.2 Deff,3
(P – P7) / P7
x / Deff,3

Figure B.8: Mean static pressures measured in the mixing region of the jet pump for Test Group 2 (tests 6 through 10). These test configurations had $N_j = 2$ and $R = 0.018$. $P_7 = 13.0$ kPa and $D_{eff,3} = 1.49$ cm.

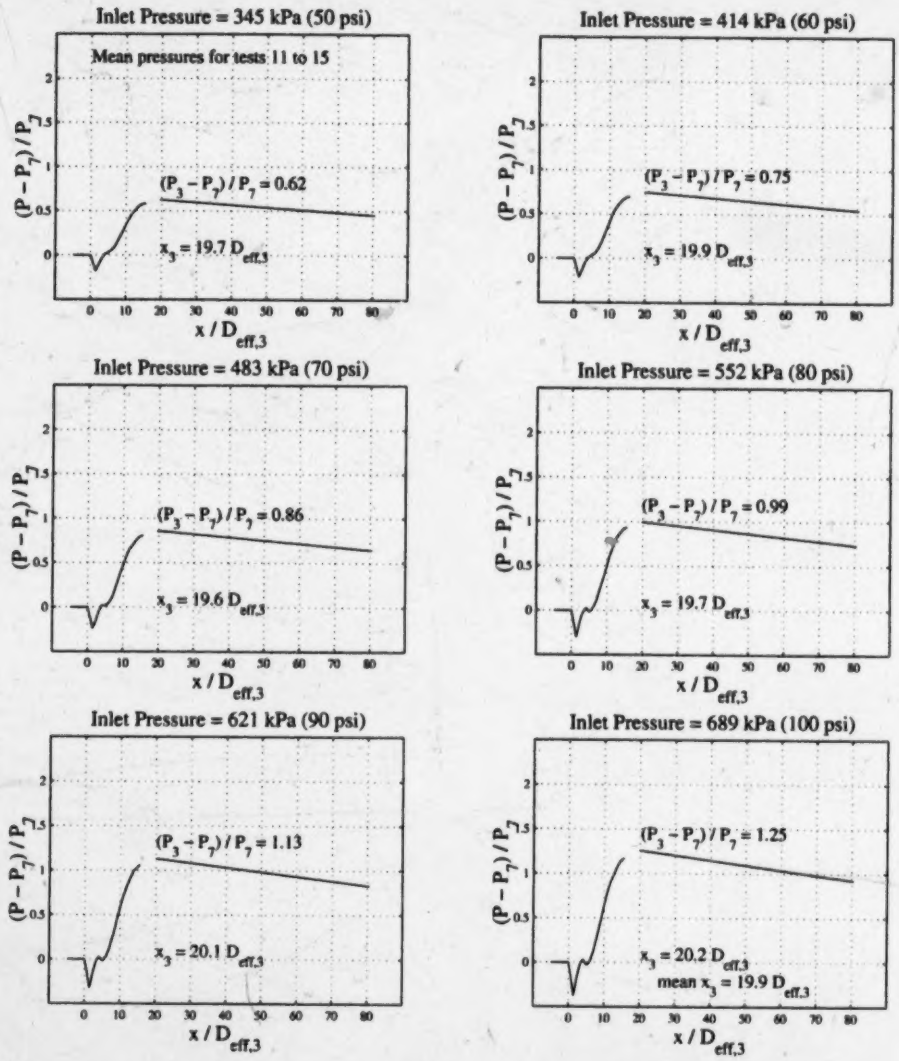
Inlet Pressure = 345 kPa (50 psi)
Mean pressures for tests 11 to 15
(P - P7) / P7
(P3 - P7) / P7 = 0.62
x3 = 19.7 Deff,3
x / Deff,3
Inlet Pressure = 414 kPa (60 psi)
(P3 - P7) / P7 = 0.75
x3 = 19.9 Deff,3
Inlet Pressure = 483 kPa (70 psi)
(P3 - P7) / P7 = 0.86
x3 = 19.6 Deff,3
Inlet Pressure = 552 kPa (80 psi)
(P3 - P7) / P7 = 0.99
x3 = 19.7 Deff,3
Inlet Pressure = 621 kPa (90 psi)
(P3 - P7) / P7 = 1.13
x3 = 20.1 Deff,3
Inlet Pressure = 689 kPa (100 psi)
(P3 - P7) / P7 = 1.25
x3 = 20.2 Deff,3
mean x3 = 19.9 Deff,3

Figure B.9: Mean static pressures measured in the mixing region of the jet pump for Test Group 3 (tests 11 through 15). These test configurations had $N_j = 3$ and $R = 0.018$. $P_7 = 13.0$ kPa and $D_{eff,3} = 1.49$ cm.

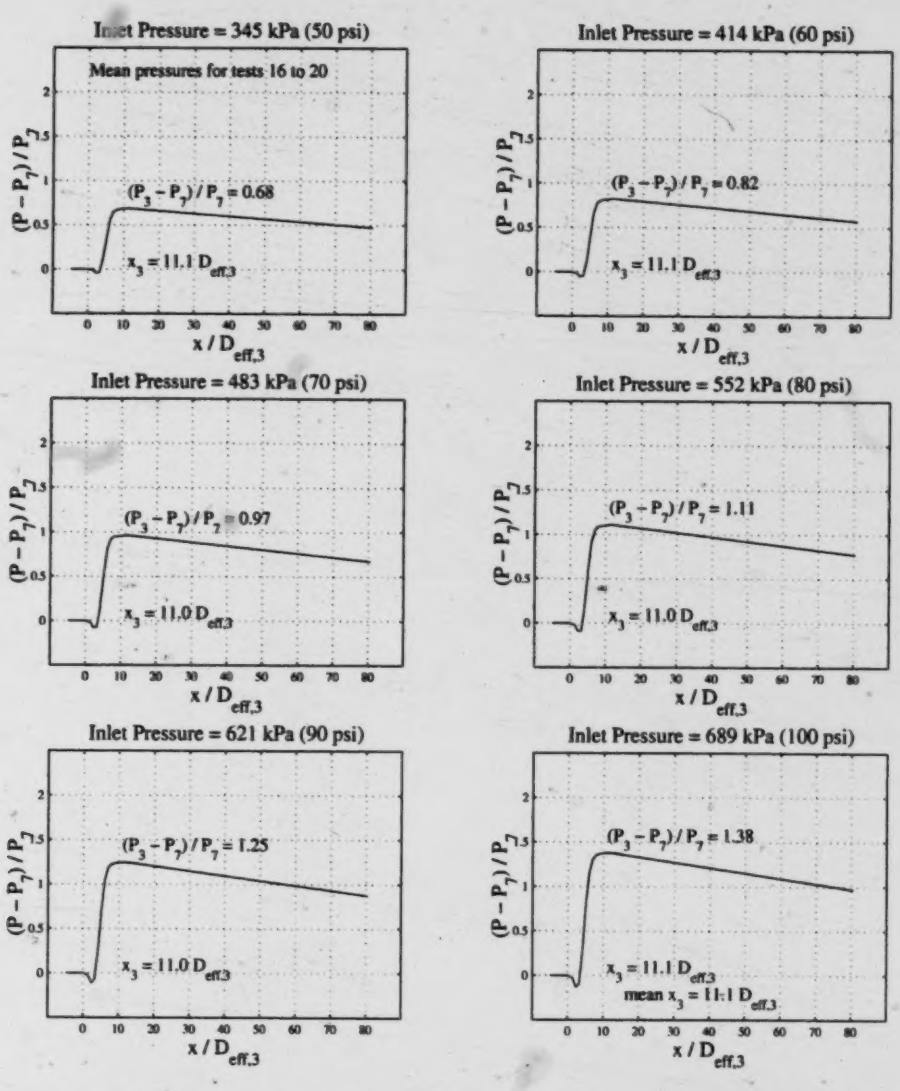
Inlet Pressure = 345 kPa (50 psi)
Mean pressures for tests 16 to 20
(P3 - P7) / P7 = 0.68
x3 = 11.1 Deff,3
Inlet Pressure = 414 kPa (60 psi)
(P3 - P7) / P7 = 0.82
x3 = 11.1 Deff,3
Inlet Pressure = 483 kPa (70 psi)
(P3 - P7) / P7 = 0.97
x3 = 11.0 Deff,3
Inlet Pressure = 552 kPa (80 psi)
(P3 - P7) / P7 = 1.11
x3 = 11.0 Deff,3
Inlet Pressure = 621 kPa (90 psi)
(P3 - P7) / P7 = 1.25
x3 = 11.0 Deff,3
Inlet Pressure = 689 kPa (100 psi)
(P3 - P7) / P7 = 1.38
x3 = 11.1 Deff,3
mean x3 = 11.1 Deff,3
(P - P7) / P7
x / Deff,3

Figure B.10: Mean static pressures measured in the mixing region of the jet pump for Test Group 4 (tests 16 through 20). These test configurations had $N_j = 4$ and $R = 0.018$. $P_7 = 13.0$ kPa and $D_{eff,3} = 1.49$ cm.

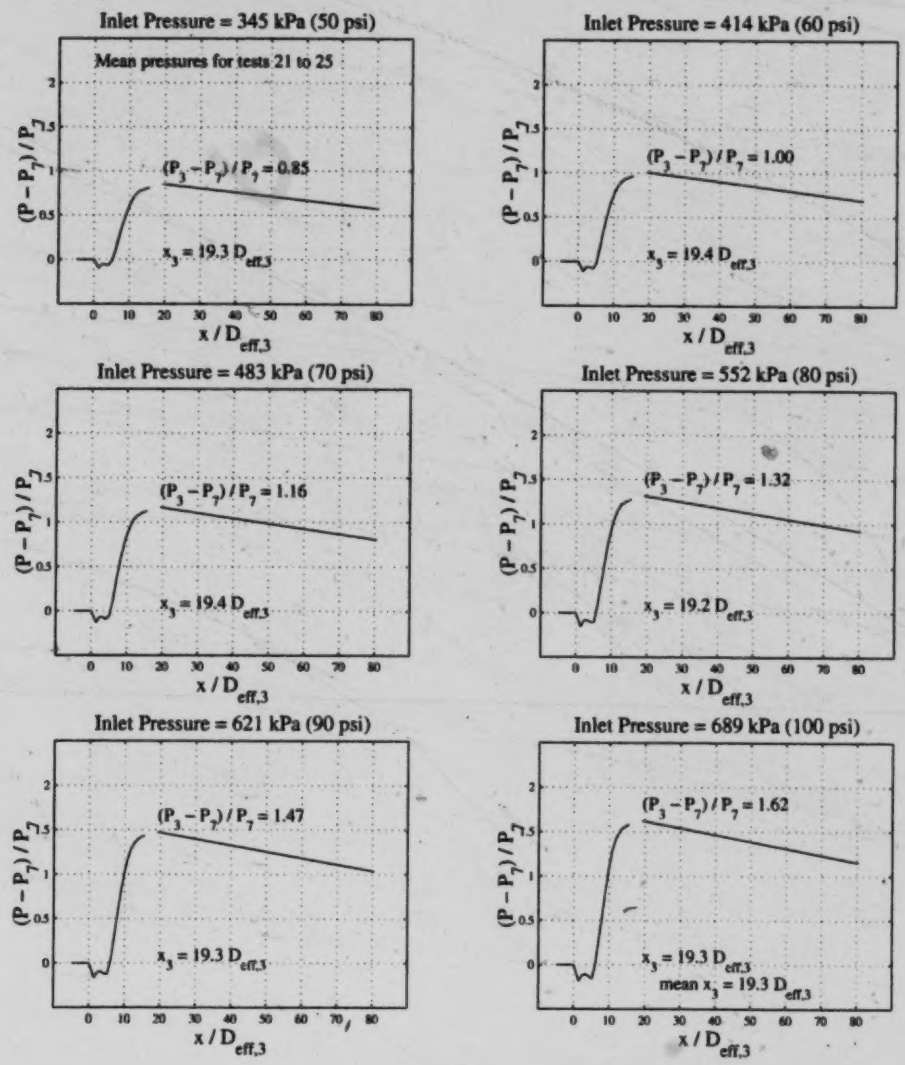
Inlet Pressure = 345 kPa (50 psi)
Mean pressures for tests 21 to 25
(P3 − P7) / P7 = 0.85
x3 = 19.3 Deff,3
Inlet Pressure = 414 kPa (60 psi)
(P3 − P7) / P7 = 1.00
x3 = 19.4 Deff,3
Inlet Pressure = 483 kPa (70 psi)
(P3 − P7) / P7 = 1.16
x3 = 19.4 Deff,3
Inlet Pressure = 552 kPa (80 psi)
(P3 − P7) / P7 = 1.32
x3 = 19.2 Deff,3
Inlet Pressure = 621 kPa (90 psi)
(P3 − P7) / P7 = 1.47
x3 = 19.3 Deff,3
Inlet Pressure = 689 kPa (100 psi)
(P3 − P7) / P7 = 1.62
x3 = 19.3 Deff,3
mean x3 = 19.3 Deff,3
(P − P7) / P7
x / Deff,3

Figure B.11: Mean static pressures measured in the mixing region of the jet pump for Test Group 5 (tests 21 through 25). These test configurations had $N_j = 2$ and $R = 0.018$. $P_7 = 13.0$ kPa and $D_{eff,3} = 1.49$ cm.

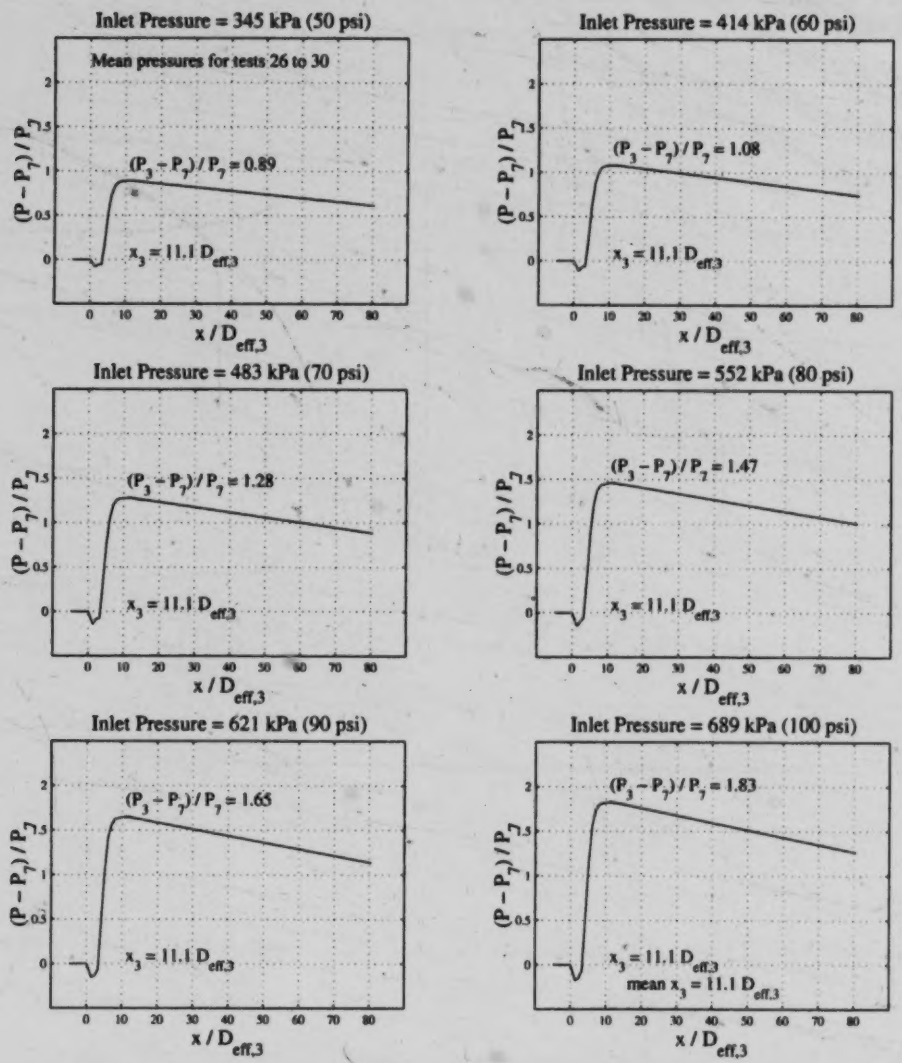
Inlet Pressure = 345 kPa (50 psi)
Mean pressures for tests 26 to 30
(P3 - P7) / P7 = 0.89
x3 = 11.1 Deff,3
Inlet Pressure = 414 kPa (60 psi)
(P3 - P7) / P7 = 1.08
x3 = 11.1 Deff,3
Inlet Pressure = 483 kPa (70 psi)
(P3 - P7) / P7 = 1.28
x3 = 11.1 Deff,3
Inlet Pressure = 552 kPa (80 psi)
(P3 - P7) / P7 = 1.47
x3 = 11.1 Deff,3
Inlet Pressure = 621 kPa (90 psi)
(P3 - P7) / P7 = 1.65
x3 = 11.1 Deff,3
Inlet Pressure = 689 kPa (100 psi)
(P3 - P7) / P7 = 1.83
x3 = 11.1 Deff,3
mean x3 = 11.1 Deff,3
(P - P7) / PJ
x / Deff,3

Figure B.12: Mean static pressures measured in the mixing region of the jet pump for Test Group 6 (tests 26 through 30). These test configurations had $N_j = 4$ and $R = 0.018$. $P_7 = 13.0$ kPa and $D_{eff,3} = 1.49$ cm.

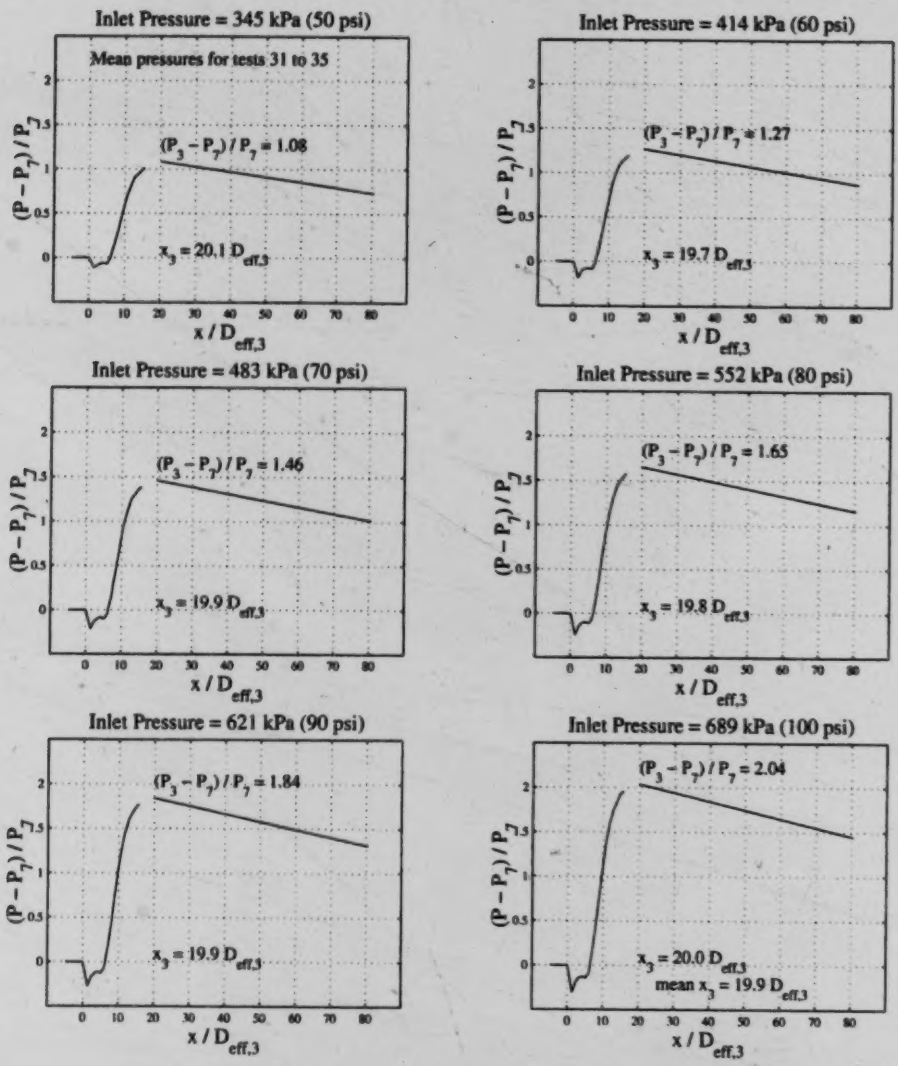
Inlet Pressure = 345 kPa (50 psi)
Mean pressures for tests 31 to 35
(P3 – P7) / P7 = 1.08
x3 = 20.1 Deff,3
Inlet Pressure = 414 kPa (60 psi)
(P3 – P7) / P7 = 1.27
x3 = 19.7 Deff,3
Inlet Pressure = 483 kPa (70 psi)
(P3 – P7) / P7 = 1.46
x3 = 19.9 Deff,3
Inlet Pressure = 552 kPa (80 psi)
(P3 – P7) / P7 = 1.65
x3 = 19.8 Deff,3
Inlet Pressure = 621 kPa (90 psi)
(P3 – P7) / P7 = 1.84
x3 = 19.9 Deff,3
Inlet Pressure = 689 kPa (100 psi)
(P3 – P7) / P7 = 2.04
x3 = 20.0 Deff,3
mean x3 = 19.9 Deff,3
(P – P7) / P7
x / Deff,3

Figure B.13: Mean static pressures measured in the mixing region of the jet pump for Test Group 7 (tests 31 through 35). These test configurations had $N_j = 2$ and $R = 0.018$. $P_7 = 13.0$ kPa and $D_{eff,3} = 1.49$ cm.

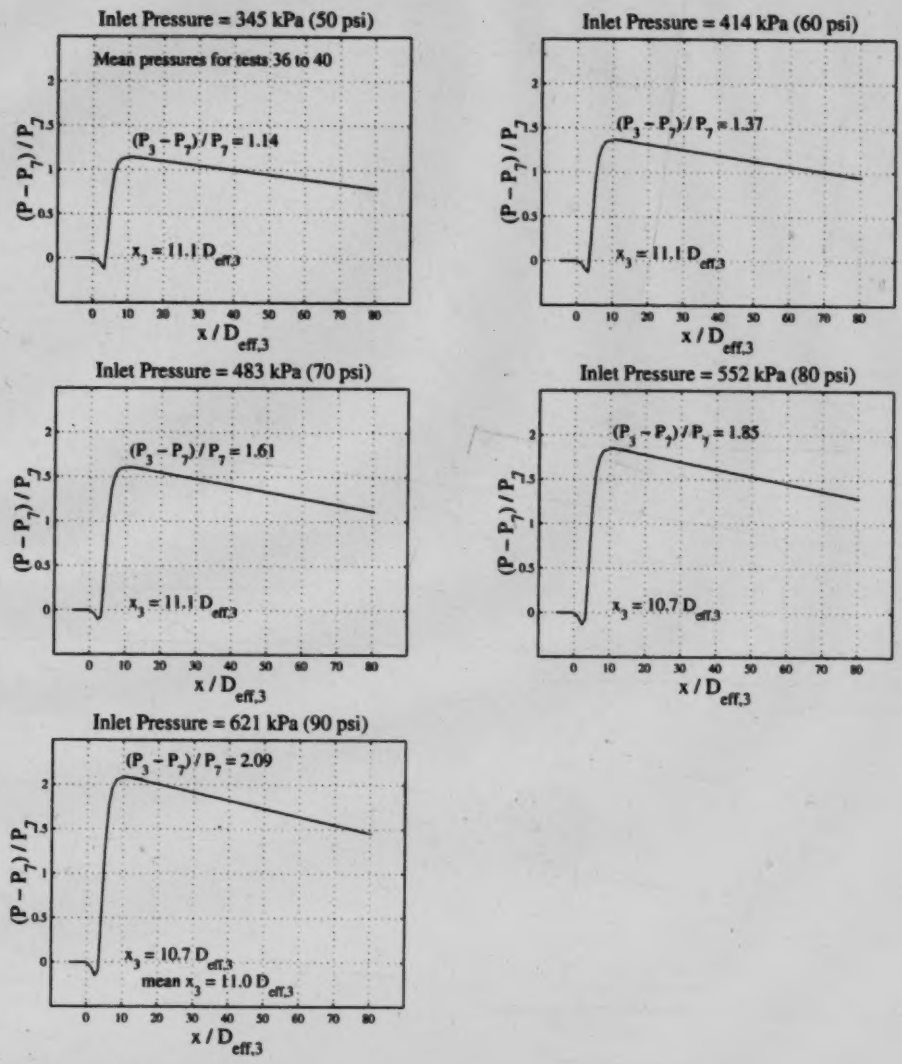
Inlet Pressure = 345 kPa (50 psi)
Mean pressures for tests 36 to 40
(P3 - P7) / P7 = 1.14
x3 = 11.1 Deff,3
Inlet Pressure = 414 kPa (60 psi)
(P3 - P7) / P7 = 1.37
x3 = 11.1 Deff,3
Inlet Pressure = 483 kPa (70 psi)
(P3 - P7) / P7 = 1.61
x3 = 11.1 Deff,3
Inlet Pressure = 552 kPa (80 psi)
(P3 - P7) / P7 = 1.85
x3 = 10.7 Deff,3
Inlet Pressure = 621 kPa (90 psi)
(P3 - P7) / P7 = 2.09
x3 = 10.7 Deff,3
mean x3 = 11.0 Deff,3
(P - P7) / P7
x / Deff,3

Figure B.14: Mean static pressures measured in the mixing region of the jet pump for Test Group 8 (tests 36 through 40). These test configurations had $N_j = 4$ and $R = 0.018$. $P_7 = 13.0$ kPa and $D_{eff,3} = 1.49$ cm.

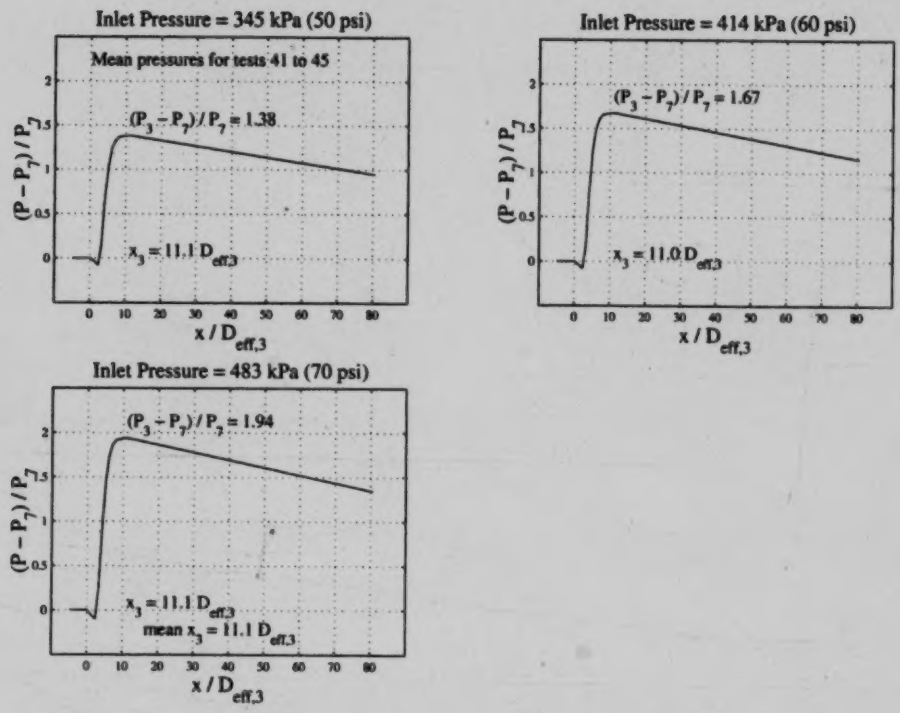
Inlet Pressure = 345 kPa (50 psi)
Mean pressures for tests 41 to 45
(P3 - P7) / P7 = 1.38
x3 = 11.1 Deff,3
(P - P7) / P7
x / Deff,3
Inlet Pressure = 414 kPa (60 psi)
(P3 - P7) / P7 = 1.67
x3 = 11.0 Deff,3
Inlet Pressure = 483 kPa (70 psi)
(P3 - P7) / P7 = 1.94
x3 = 11.1 Deff,3
mean x3 = 11.1 Deff,3

Figure B.15: Mean static pressures measured in the mixing region of the jet pump for Test Group 9 (tests 41 through 45). These test configurations had $N_j = 4$ and $R = 0.018$. $P_7 = 13.0$ kPa and $D_{eff,3} = 1.49$ cm.